PARTICLE MANIPULATION WITH OSCILLATORY NON-LINEAR MICROFLUIDICS

BY

GIRIDAR VISHWANATHAN

DISSERTATION

Submitted in partial fulfillment of the requirements
for the degree of Doctor of Philosophy in Mechanical Engineering
in the Graduate College of the
University of Illinois Urbana-Champaign, 2022

Urbana, Illinois

Doctoral Committee:

Assistant Professor Gabriel Juarez, Chair and Director of Research
Associate Professor Kyle Smith
Associate Professor Qian Chen
Professor Sascha Hilgenfeldt

Abstract

In this work, inertial and electro-inertial nonlinear phenomena arising in oscillatory microfluidic flows in the 10 – 1000 Hz range and their potential for manipulating microparticles are experimentally examined and supported with theory and simulation. First, the use of viscous streaming flows, which are steady secondary vortices emerging due to inertia near a solid surface immersed in an oscillatory background flow, is considered. For a particular surface geometry, the viscous streaming vortices are shown to manifest in qualitatively distinct topological phases depending on the frequency. These phases are characterized by the configuration of centers and saddle points of the vortices. It is shown that particles can either be 'attracted' and trapped or 'repelled' and cleared away from the flow path around the boundary by choosing the geometry appropriately. The particle manipulation efficiency is found to improve with an increasing frequency above a minimum threshold below which particle manipulation is ineffective. Next, the cross-streamline inertial migration of particles in a quasi-2D channel flow to specific stable positions, known as inertial focusing, is examined in $10 - 1000$ Hz oscillatory flows. It is found that oscillatory flows enable the focusing of much smaller particles than possible with conventional steady flow inertial focusing ($Re_p < 0.1$) due to the large effective length ($1 - 10$ m) traveled by particles even in a relatively short channel (4 cm). In this case, there exists a critical frequency above which focusing efficiency decreases rapidly but below which it is constant, in contrast with steady streaming. Further, the oscillatory flows enable precise measurement of the migration velocities which can be directly compared against analytical theories and numeric simulations. A corresponding asymptotic theory is also derived and its prediction is compared against mi-

gration velocity and focusing position measurements to good concord. Finally, the Brownian limitation on inertial focusing is surpassed using cross-coupled nonlinear interaction between synchronized oscillatory hydrodynamic and electrokinetic effects, a technique referred to as Synchronized Oscillatory Electro-Inertial Focusing (SOEIF). SOEIF is demonstrated to be capable of manipulating particles up to 3 orders of magnitude smaller than the channel width (corresponding to $Re_p \ll 0.001$). The phase difference between the oscillatory flow and field is found to be a critical parameter and its effect is characterized by measurements of focusing position, efficiency, and migration velocities. It is found that the focusing position can be tuned to anywhere between the channel center and the wall by changing the phase difference between the field and flow. Additional measurements towards uncovering the precise mechanism of SOEIF are also presented.

Acknowledgments

I would like to thank my advisor, Dr. Gabriel Juarez and the wonderful Juarez group for their immense support, co-operation and enthusiasm in my work and ideas; the committee members: Dr. Sascha Hilgenfeldt, Dr. Kyle Smith and Dr. Qian Chen for their insightful guidance and constructive criticism, as well as, their inspiring work; Dr. Glennys Mensing for her mentorship and expertise; Dr Aditya Khair and Dr. Mattia Gazzola for sharing their wisdom. Finally I would like to acknowledge the incalculable contributions of Ms. Kathy Smith and the entire graduate student body of MechSE in making my work possible.

Table of Contents

Chapter 1

Introduction

Microfluidics refers to the study and application of fluid flows in artificially fabricated channels and surface manifolds with features having a characteristic length scale (l) in the $10^{-9} - 10^{-3}$ m (μm-nm) size range. For an internal or channel flow, the characteristic length scale l, is set by the hydraulic diameter ($l = D_h = 4A_c/P_c$), where A_c is the cross sectional area of the channel and P_c is the perimeter of the cross section. For external flows, typically flow around an obstacle, such as a cylinder or an aerofoil, it is taken to be the radius of curvature ($l = a$) of the surface.

The defining parameter that characterizes all fluid flows is the dimensionless Reynolds Number : $Re = Ul/\nu$ and can be interpreted as the ratio of inertial stresses, to the viscous stresses. Here U is the characteristic velocity, usually either the maximum or average speed of a fluid particle depending on context; and ν is the kinematic viscosity, an intensive thermodynamic material property of the fluid.

Owing to the relatively small length scales in traditional microfluidic flows, the Reynolds number is small compared unity ($Re \ll 1$). Flows with $Re \ll 1$ are referred to as Stokes flows or creeping flows in fluid mechanics literature, and are characterized by their temporal reversibility and the absence of swirling eddies and intermittent random fluctuations observed in everyday macroscopic fluid flows. Temporal reversibility implies that when the direction of fluid flow is reversed, every point in the fluid retraces its path exactly.

Due to a combination of these small length scales, and the consequent predictability and repeatability of flows, microfluidic technologies have emerged as a powerful platform for integrating several complex chemical and bio-analytical processes into a single device. The

advantages the microfluidic approach include orders of magnitude ($10^{-2} - 10^4$ times) less reagent consumption, higher specificity, precision, and shorter analysis times than conventional glassware laborotory processes.

Non-linear microfluidics, hitherto synonymous with inertial microfluidics, refers to systems that utilize hydrodynamic effects that arise when $Re \sim \mathcal{O}(1)$), coincident with the temporal irreversibility of flow. Typically, nonlinear microfluidic devices operate by using inertial forces acting on fluids or particles to accomplish either mixing or sorting/separation of microparticles, typically with radii in the range $3 - 30$ μm. Since the advent of inertial focusing [Di Carlo et al., 2007], inertial microfluidics has quickly risen to prominence with multiple commercial devices currently available for purchase.

Its attractiveness may understood as a combination of two factors, the first is that unlike most other techniques of particle separation which become less effective with increasing flow rate, inertial microfluidics improves with the increasing flow rate enabling much larger throughputs ($>$ 1 ml/min) than all other techniques for particle radii in the $3 - 30$ μm range. The second, is it's entirely passive operation. In other words, it requires no additional electronics or sensors to use, making it very easy to implement.

The ease of focusing microparticles is determined by the Reynolds number at the scale of the particle: $Re_p = Ua^2/\nu l$ for neutrally buoyant particles. Particles in a Newtonian fluid with $Re_p < 0.1$ usually cannot be focused due practical limitations associated with the long ($>$ 20 cm) channel lengths. Briefly, these limitations are ; 1) Microchannels greater than 20 cm in length have large pressure drops requiring more specialized methods of fabrication and making integration of multiple systems difficult; 2) The resulting shear stresses in long and narrow channels can damage biological particles such as cells, vesicles and organelles. More recently, inertial focusing with quasi-steady oscillatory flows ($1 - 10$ Hz) has shown promise in overcoming these difficulties [Mutlu et al., 2018], enabling smaller (radius $a < 1$ μm), and more delicate biological particles (max shear rate :$\dot{\gamma}_{max} < 10^4$) to be focused.

Another inertial hydrodynamic phenomenon, that has been used for mixing and sort-

ing in microfluidic devices is steady streaming [Friend and Yeo, 2011, Wiklund et al., 2012]. Steady streaming refers to the steady flows [Riley, 2001] that occur near a solid/fluid boundary in a surrounding fluid that oscillates with a frequency f ($1 - 100$ KHz), and small-amplitude s ($s/l \ll 1$) due to fluidic inertia. The magnitude of the characteristic streaming velocity scales as $U_s \sim \epsilon s\omega$, where $\epsilon = s/l$ is the dimensionless amplitude and $\omega = 2\pi f$ is the angular frequency. At small scales, these steady flows have been shown to be useful in position control [Amit et al., 2016], trapping [Lutz et al., 2006a] and sorting [Wang et al., 2011, Thameem et al., 2017] of particles and cells. Like inertial focusing, streaming flows require $Re = ls\omega/\nu \sim \mathcal{O}(1)$ for operation and can therefore be included into the umbrella of inertial microfluidics, albeit using oscillatory flows that are typically in the $1 - 100$ KHz regime.

In this thesis, the continuum between steady streaming and inertial focusing are experimentally explored using oscillatory flows in the $10 - 1000$ Hz frequency regime for the purposes of particle manipulation. The choice of $10 - 1000$ Hz is motivated by the fact that both effective steady streaming and inertial focusing can conceivably be achieved in this frequency regime using a simple, low cost and robust experimental setup. Further, by careful choice of the experimental geometry and characteristic length, one can examine the entire range of transient inertial effects characterized by the dimensionless Womersley numbers $\alpha = l/\sqrt{\nu/\omega}$ using this range of frequency. Through these experiments, I also emphasize how both techniques of particle manipulation arise from different inertial mechanisms at the particle scale, despite having common ground in their origin and implementation and result in different qualitative dependence on the frequency or the Womersley number. This implies that oscillatory inertial focusing and steady streaming are complementary and can be multiplexed to achieve different effects under identical conditions.

Finally, I make an attempt towards generalizing the concept of nonlinear oscillatory microfluidics beyond a purely hydrodynamic phenomena by incorporating an oscillatory electric field aligned with and in addition to the oscillatory flow at the same frequency. This is done to study the nonlinear interaction between oscillatory electrokinetic and oscillatory

hydrodynamic effects which manifests as a steady migration; a process referred to as cross rectification. Such an approach provides an avenue to transcend the limitations of using purely inertial effects for particle manipulation, while retaining its unique advantage of improving efficiency with increasing throughput. Through this work, I hope to motivate the use of nonlinear oscillatory microfluidics as an exciting new paradigm for microfluidics.

The organization of the thesis is as follows:

In Chapter 2, I describe the construction of an experimental apparatus used to generate oscillatory flows in inside a microchannel. I then characterize its range of amplitudes, frequencies, and the Fourier spectrum for sinusoidal and non-sinusoidal (square, sawtooth, triangle) waveforms. This is followed with a validation, done by comparing benchmark experimental results against established theories for oscillatory flow inside a square channel and near a flat plate. Descriptions of standard protocols such as particle and fluid properties, amplitude measurement, imaging and particle tracking used in the remaining chapters are also elaborated.

In Chapter 3, I describe experiments on steady streaming which are supported by direct numerical simulations (DNS). First streaming around a single cylinder is considered and its key topological features (vortex centers and saddle points) are characterized as a function of frequency and cylinder aspect ratio. Next I report the streaming topology around a periodic lattice of a single curvature, followed by a checkerboard lattice for different curvature ratios. The application of the lattice to trap inertial particles ($St > 0.1$) and its resulting efficiency is evaluated for different frequencies. Next, continuous flow separation of inertial particles from a flow path is studied using a fore-aft asymmetric (bullet) geometry and its efficiency is evaluated against frequency. An analysis of the viability of model mammalian cells that are subjected to steady streaming is also presented.

In Chapter 4, I investigate oscillatory inertial focusing in a straight quasi 2D channel. I begin by deriving an asymptotic theory for small particle migration in such flows and reporting its predictions. The steady state focusing position and focusing efficiency are

characterized for different oscillatory amplitudes, particle sizes, and frequencies. Additionally, transient effects on the inertial focusing efficiency are discussed. The transient regime is then applied towards imaging particles and measuring the particle migration velocity. The measurements of particle migration velocity and focusing position are compared against theoretical predictions.

In Chapter 5, I describe the basics of SOEIF. This is followed by a characterization of the steady state focusing position and focusing efficiency versus the phase difference between the oscillatory flow and electric field. The nature of nonlinear interaction between oscillatory field and flow is examined by measurements of the migration velocity for a single particle size at different values of oscillatory field amplitudes and driven flow oscillation amplitudes. Finally, the migration velocity measurements for different particle sizes are reported for identical conditions and its scaling with radius is investigated.

In Chapter 6, I first summarize the key findings results. I then provide a subjective assessment of the state of microfluidics as a technology and an industry. Recommendations on where and how the contributions can be applied are made. I conclude with the best future directions that can be taken in light of this context.

Chapter 2

Experimental setup and methods

2.1 Review

At low frequencies ($0.1 \leq f \leq 10$ Hz), oscillatory flows are usually achieved by a programmed syringe pump, electromechanical relay valves [Abolhasani and Jensen, 2016] or a pneumatic pressure controller [Zhou and Schroeder, 2016]. The fidelity of the desired waveform is limited by inertia of the oscillatory driver. For low frequencies, the response time of syringe pumps and actuators in electromechanical valves and pnuematic pressure controllers is on the order of $\mathcal{O}(10$ ms), therefore preventing the realization of sinusoidal oscillations at higher frequencies.

At high frequencies ($10^3 \leq f \leq 10^6$ Hz), piezoelectric transducers, which typically possess resonant frequencies in this range, are used [Rallabandi et al., 2017, Phillips et al., 2016, Xie et al., 2015, Lieu et al., 2012, Morris and Forster, 2000]. At these frequencies, effects are usually local to the transducer and are effected through the use of rigid boundaries, interfaces or bubbles which serve to amplify their effect within a microfluidic device.

The utility of piezoelectric transducers in the $10 - 1000$ Hz range are limited by the small amplitudes generated. These amplitudes may be partially increased through the use of designed features such as membrane cavities in the channel on to which the piezo elements need to be bonded to be used properly [Vázquez-Vergara et al., 2017]. More recent designs of microfluidic oscillators primarily aim to achieve oscillatory flows free of external actuators with a focus on miniaturization and integration with other lab-on-chip modules. This is typically done by exploiting non-linear fluid-elastic interaction with a membrane

or diaphragm unit as a steady flow is driven through it. Therefore, a time dependent response is obtained even with a steady input at low Reynolds numbers [Xia et al., 2012, Leslie et al., 2009, Kim et al., 2013, Mosadegh et al., 2010]. Other possibilities such as the use of non-Newtonian fluids for switching [Groisman et al., 2003], generation of oil droplets as an oscillatory source [Basilio et al., 2019], and the Coanda effect [Yang et al., 2007] have also been explored. Although these micro-oscillators are highly miniaturized, modular and in some cases, capable of producing frequencies in the audible range [Xia et al., 2012], they are mostly integrated with the device through bonding or through pre-designed features making it inconvenient to test different channel geometries and thus discouraging their use in a research setting. Further, in microfluidic oscillators that function based on fluid elastic interaction the amplitudes and frequencies are coupled and hence cannot be independently controlled.

2.2 Construction and Setup

The apparatus is set up as displayed in the schematic, shown in Figure 2.1 (a). A loudspeaker [I] (DROK TDA7297B, 15 W, 90 dB) is situated on the microscope stage by placing it on, and taping it to a 3D printed speaker mount [II]. A 3D printed elbow adapter [III] is bonded to the speaker cone such that it is coaxial with the diaphragm by applying silicone around the circumference of the interface. One end of the microfluidic tubing [V] (PE60 Intramedic 427416, 0.76 mm ID $\times$ 1.22 mm OD) is threaded through a cut micropipette tip that acts as a conical sleeve [IV]. The tube then enters into the front end, and exits out of the side end of the elbow adapter into an outlet receptacle or reservoir. The conical sleeve is forced into the adapter creating a tight wedge seal between the tube and elbow. The other end is inserted into the outlet of a PDMS-glass microchannel [VI] and sealed with silicone or epoxy. The microchannel is placed in the optical path of the inverted microscope for observation.

To drive the speaker, an AUX controlled amplifier chip is used. A pair of multi-stranded

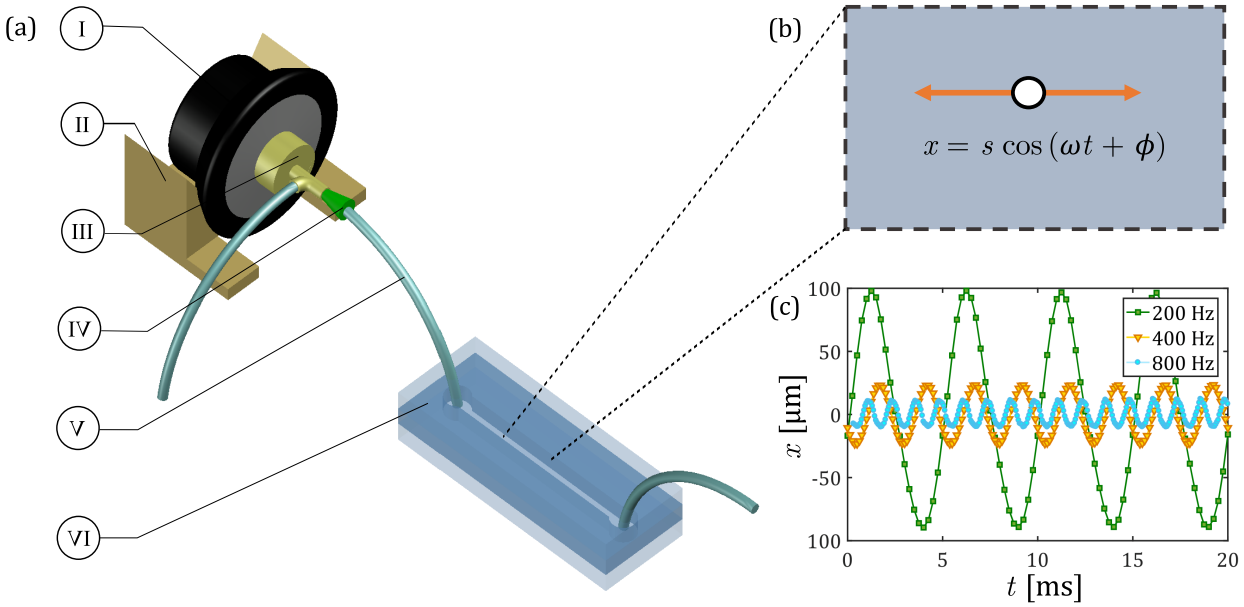

Figure 2.1: (a) Schematic of the experimental setup. The loudspeaker diaphragm is directly interfaced with microfluidic tubing (maintained taut and filled with liquid) to generate sinusoidal liquid oscillations in a PDMS microchannel. The critical components are (I) speaker, (II) 3d printed speaker mount, (III) speaker-to-tube adapter, (IV) pipette-tip wedge seal (V) polyethylene tubing, and (V) PDMS microchannel. (b) Schematic of tracer particle (and liquid) displacement in a microchannel described by the oscillation amplitude and angular frequency. (c) Experimental streamwise displacement of 0.93 μm diameter tracer particles in water over a number of oscillation cycles obtained with micro-particle tracking velocimetry.

wires connects the terminals of the speaker to output terminals of the chip. A connected AUX cable carries the input signal of the desired waveform, frequency and voltage amplitude from a computer or smartphone using a waveform generator application. Typically, a 100% volume setting corresponds to an input voltage amplitude of 5.0 V to the amplifier chip.

During operation, the input analog voltage is converted to an oscillatory displacement of the diaphragm by the speaker. The diaphragm displacement is transduced into elastic deformations of the microfluidic tubing at the fixed end of the device outlet. The stress induced by tubing deformation generates a time-varying pressure within, resulting in oscillatory displacement of the liquid at the same frequency as the diaphragm. To minimize higher harmonic signals, the tubing must be maintained taut with minimal tension such that its boundary conditions correspond to a fixed end at the microchannel outlet and a forced oscillatory displacement at the diaphragm. For maximum amplitude and repeatability, the microchannel and tube must be fully primed with liquid. In addition to the oscillatory flow, a steady flow can also be simultaneously setup inside the channel using a syringe pump to drive liquid at the inlet.

Flow visualization was achieved with brightfield microscopy by using suspending polystyrene tracer particles in the working liquid. To image the temporal characteristics of the oscillatory flow, a high-speed global shutter scientific CMOS camera (Edgertronic® SC2+) was used with a frame rate exactly twenty times larger than the driving oscillation frequency ($20f$). To view time-averaged steady flow or the migration of inertial particles, stroboscopic imaging was performed with a high resolution global shutter CMOS camera (XIMEA® XiQ). The displacement and velocity fields are then obtained from 2D particle tracking velocimetry algorithms [Ouellette et al., 2006].

2.3 Characterization

For the characterization and subsequent validation of the generated oscillatory flow presented in this chapter, experiments were performed with deionized water (unless specified otherwise) of density $\rho = 1005$ kg/m^3, dynamic viscosity $\mu = 0.96$ mPa.s and kinematic viscosity $\nu = \mu/\rho = 0.95$ mm^2/s. The suspended polystyrene tracer particles have a mean diameter of $d = 0.93$ μm and density of $\rho_p = 1060$ kg/m^3. The relaxation time of the tracer particles : $\tau = \rho_p d^2/18\mu \approx 50 \times 10^{-9}$ s, is much smaller than the oscillatory timescales considered in this study ($\tau \ll 1/f$) ensuring that the tracers accurately reflect the underlying flow field.

The PDMS microchannel geometries used are: (i) a square channel with a width and height of 110 μm and length of 6 cm, (ii) a rectangular channel with a width of 5 mm, height of 200 μm, and length of 2 cm. Tracer particles at the midplane of the microchannel were observed using brightfield illumination with objectives of 10$\times$ and 20$\times$ magnification (depth of field 8.5 μm and 5.5 μm respectively).

The streamwise displacement of a tracer particle in a channel flow is illustrated in Figure 2.1 (b) and described by $x = s\cos(\omega t + \phi)$. Here, s is oscillation amplitude, $\omega = 2\pi f$ is the angular frequency, and ϕ is the initial phase. The characteristic liquid velocity is $U = s\omega$.

Examples of the displacement of tracked particles from their mean position during a 20 ms period are shown in Figure 2.1 (c). The ratio of sampling frequency (camera framerate) to liquid oscillation frequency is kept constant at 20. That is, for oscillation at 200, 400 and 800 Hz, a framerate of 4000, 8000 and 16000 Hz is used, respectively. The corresponding amplitudes are 100, 27 and 14 μm.

The operational range of amplitude and frequency is shown in Figure 2.2 (a). For a given frequency, the displacement of a tracer particle is dependent on the volume setting of the loudspeaker. As an example, three volume settings (input voltages) are considered here: low (1.5 V), intermediate (3.0 V), and high (4.5 V). At 100 Hz, for example, the amplitude ranges from 50 μm at low to 800 μm at high volume setting. The amplitude swept by

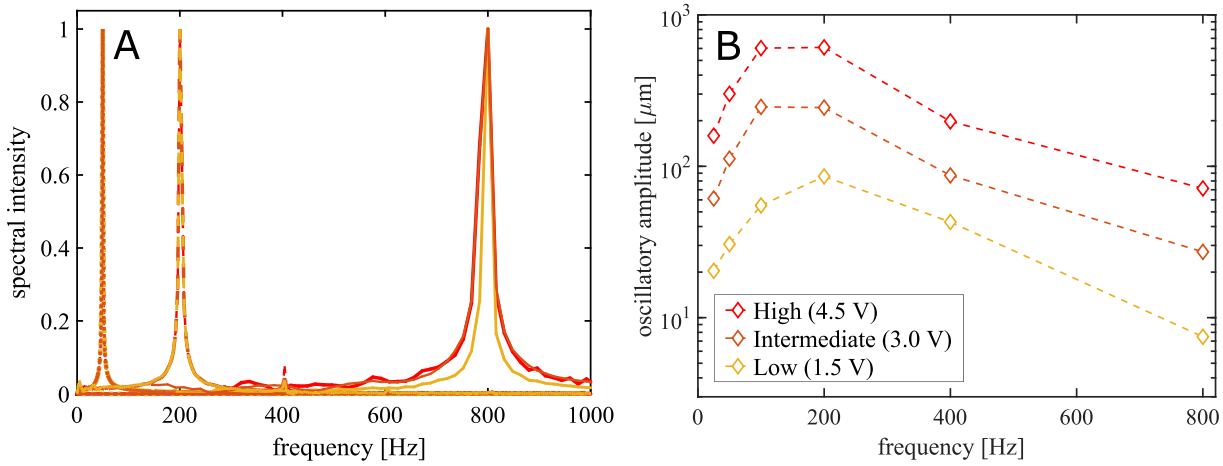

Figure 2.2: (a) Fourier spectrum analysis of tracer particle displacement in the streamwise direction at three different frequencies (50, 200, and 800 Hz) and volume settings (input voltages): Low (1.5 V, yellow), intermediate (3.0 V, orange) and high (4.5 V, red). (b) The amplitude of oscillatory displacement in microchannels for a range of frequencies and volume settings.

a tracer particle over a single oscillation period, for a given volume setting, shows a non-monotonic variation with frequency due to the performance characteristics of the speaker. The maximum oscillation amplitude occurs at 200 Hz, which corresponds to the resonant frequency ($\approx$ 230 Hz) of the loudspeaker diaphragm.

A Fourier spectrum analysis of particle trajectories at varying oscillation amplitudes and frequencies is shown in Figure 2.2 (b). The spectra have been obtained for oscillation frequencies of 50, 200 and 800 Hz and at volume settings of low, intermediate, and high. For low and intermediate volume settings, monodisperse peaks in the spectral intensity correspond to the input driving frequency of the loudspeaker. The peaks are especially narrow at 200 Hz, or near the resonance frequency of the diaphragm. For high volume settings, widening of the peak is noticeable. For 800 Hz at high volume setting, contributions due to higher harmonics are of considerable magnitude.

A quantitative measure of harmonic distortion present in the signal as compared to the fundamental driving frequency is obtained by calculating the total harmonic distortion (THD). The THD is defined as THD $= \sqrt{\Sigma_{i=1}^{N} V_i^2}/V_1$, where V_i is the power of the spectral

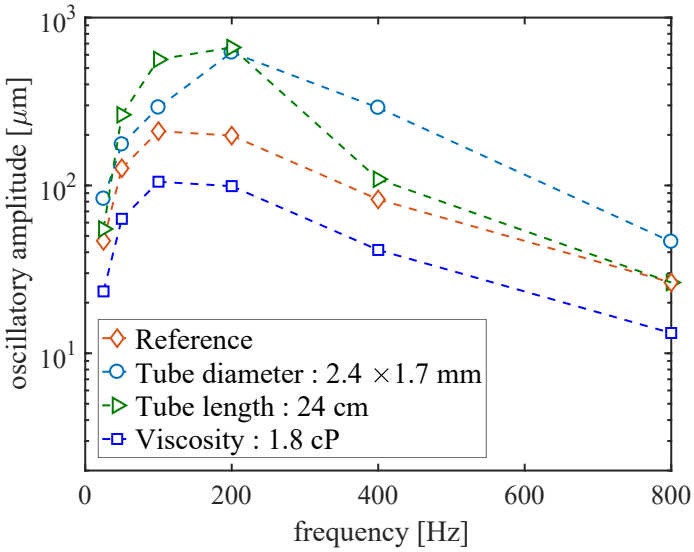

Figure 2.3: Effects of tube length, tube diameter and liquid viscosity on oscillatory amplitude. When compared to the reference case, an increase in tube length or tube diameter will lead to an increase in oscillation amplitude over the range of operational frequencies. An increase in viscosity, however, decreases the oscillation amplitude.

intensity at the ith harmonic [Shmilovitz, 2005]. A low THD value is associated with a more accurate representation of the original driving signal. For low volume settings, the THD at 50, 200, and 800 Hz are 3.5%, 7.1%, and 9.1%, respectively. For intermediate volume settings, the THD at 50, 200, and 800 Hz are 5.2%, 8.9%, and 13.4%, respectively.For high volume settings, the THD at 50, 200, and 800 Hz are 7.3%, 11.1%, and 21.3%, respectively. The growing magnitude of higher harmonics with increasing speaker volume typically limits operation at frequencies $>$ 400 Hz to low or intermediate speaker volumes. At low frequencies however, the maximum amplitude is chosen to avoid damage to the microchannel or unfastening of the outlet tube from the speaker cone. Therefore, sinusoidal oscillations with displacement amplitudes up to 100 μm and velocity amplitudes up to 4 cm/s can be reliably achieved throughout the frequency range of $25 - 800$ Hz. The resulting ranges of the Womersley and Reynolds numbers are $1.5 < \alpha < 15$, $0.4 < \mathrm{Re} < 80$ respectively. The dimensionless amplitude $\epsilon = \mathrm{Re}/\alpha^2$ ranges from $0.1 < \epsilon < 5$.

Next, the effect of the liquid viscosity, the tube diameter and tube length on the oscilla-

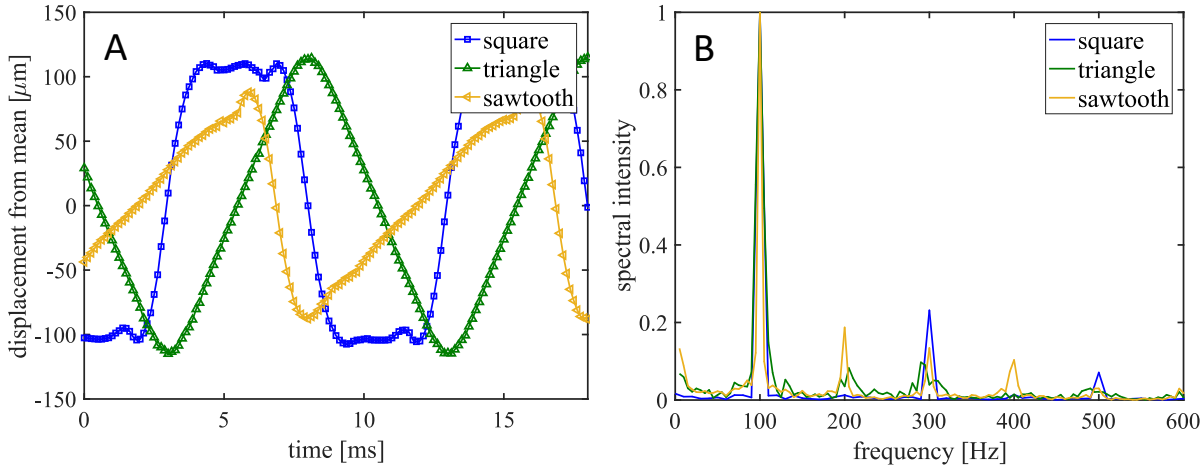

Figure 2.4: Examples of non-sinusoidal waveforms. (A) Particle displacements for square, triangular and sawtooth waveforms at an oscillation frequency of 100 Hz. (B) The corresponding Fourier spectra for non-sinusoidal particle displacements.

tory amplitude over the range of operational frequencies is examined. For these experiments, the driver amplitude is maintained constant at the intermediate level (3.0 V) and only one setup parameter is modified at a time while the remaining parameters are identical to the reference control case (diamond symbols). The corresponding results for oscillation amplitude versus frequency are shown in Figure 2.3. When the viscosity of the working liquid is increased by changing to a 25% glycerol solution ($\mu = 1.81$ mPa.s) the amplitude decreases by a factor of nearly 2 over the range of operating frequencies (square symbols). This suggests that, in general, increasing the liquid viscosity compared to that of DI water would result in a similar characteristic amplitude versus frequency curve with a constant factor decrease in the amplitude. When the microfluidic tubing diameter for the same material (polyethylene) is increased to 2.41 x 1.67 mm, the amplitude increases compared to the reference case by a factor between 1.5 up to 3 depending on the frequency (circle symbols). The increase is larger at high frequencies and smaller at low frequencies, indicating the resonant frequency has increased. When the tube length for the same material (polyethylene) is increased to 24 cm (by a factor of 2), the amplitude increases significantly near the resonant frequency, but remains unchanged from the reference control case at very low and very high frequencies

(triangle symbols).

In addition to the sinusoidal waveforms discussed above, non-sinusoidal waveforms are also demonstrated. Particle displacement tracks for square, triangle and sawtooth waveforms are shown in Figure 2.4 A. Here, the amplitude setting is intermediate (3.0 V), the driving frequency is 100 Hz, and particles are observed at 4000 frames per second.

As expected, very sharp changes in position associated with the vertical segments of square and sawtooth waveforms are not possible in real systems with a finite response time. These vertical segments of the voltage waveform are translated into steep inclined segments in the fluid. From the square waveform, it is seen that it takes approximately 1 ms for the displacement to change from $+100$ to -100 μm. Based on this, the response time of the system may be estimated to be 1 ms. Nonetheless, the Fourier spectra of these waveforms are observed to be in good agreement with the ideal spectra, at least up to the third harmonic and shown in Figure 2.4 B.

The maximum pressure inside the square channel may be estimated from the modified Poiseuille formula:

$$\Delta P = \frac{64 \mu L s f}{D_h^2} \ , \tag{2.1}$$

where D_h and L are the hydraulic diameter and length of the channel. For the square channel ($D_h = 110$ μm and $L = 6$ cm) filled with DI water ($\mu = 0.96$ mPa.s) and settings for maximum oscillatory displacement ($f = 200$ Hz, $s = 600$ μm), the pressure inside the channel is calculated to be approximately equal to 31 kPa.

2.4 Validation

The small length scales of $\mathcal{O}(100$ μm) associated with microchannels imply that most microscale flows are laminar flows governed by the Stokes equation. An important feature of microscale oscillatory flows in the $25 - 800$ Hz range is that transient effects associated with the unsteady Stokes equation become significant. An example of departure from Stokes flow

is illustrated by the comparison of the steady Stokes flow velocity profile [O'Brien, 1975] at the midplane (black solid curve) against those obtained experimentally for oscillatory flow through a square channel (110 μm $\times$ 110 μm $\times$ 6 cm) at different frequencies (symbols), shown in Figure 2.5 (a).

To obtain the amplitude of velocity in the square channel midplane, $50 - 200$ particles (0.93 μm) are tracked for one hundred oscillation cycles and their respective velocities are computed. The amplitude of each velocity series ($U_{max}(y)$) is obtained and superposed in the streamwise direction. The resulting spread of speeds is filtered for outliers and averaged. The associated statistical error bars are smaller than the data markers shown.

The results for 100 Hz and 400 Hz are similar to the Stokes laminar flow profile (black solid curve). At 800 Hz, however, there is considerable deviation from the steady velocity profile due to increasing Womersley number α with frequency. For 100, 400, and 800 Hz, α is 2.75, 5.51, and 7.78, respectively. For each α, the analytical series solutions for the amplitude of the midplane oscillatory velocity profiles ($U_{max}(y)$) were evaluated correct to one hundred terms [O'Brien, 1975], and are shown by the continuous lines to good agreement with experimental data, even at 800 Hz.

In contrast, deviations from the unsteady Stokes equation are demonstrated in Figure 2.5 (b) by comparing the amplitude of measured oscillatory flow (symbols) in the rectangular channel ($l \gg H$), with those obtained theoretically from the solution to oscillatory flow over an infinite flat plate (Stokes' second problem) [Landau and Lifshits, 1959]. The maximum temporal flow velocity as a function of distance from a flat plate is given by the expression:

$$U_{max}(y)/s\omega = \sqrt{2}e^{-y/(2\delta_{AC})}\sqrt{\cosh\left(y/\delta_{AC}\right) - \cos\left(y/\delta_{AC}\right)}\ , \tag{2.2}$$

where δ_{AC} is the Stokes boundary layer length and equal to $\sqrt{\nu/\omega}$. At 800 Hz, normalized experimental data (symbols) is in good agreement with equation (2.2). At 50 Hz, and to a lesser extent at 200 Hz, deviations from the theory occur where the velocity amplitudes are

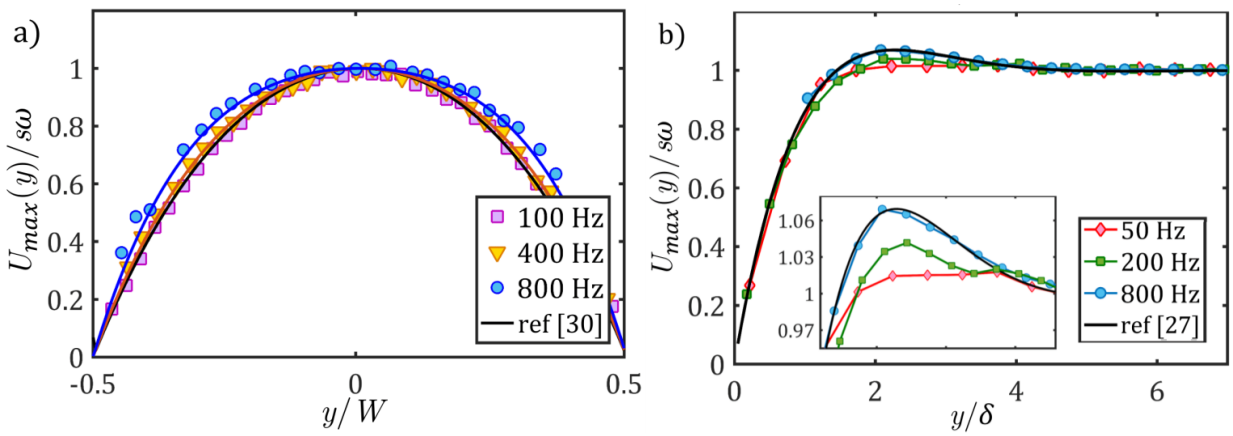

Figure 2.5: (a) Oscillatory velocity flow profile in a square channel (symbols) showing deviation from Stokes flow profile (black solid curve) with increasing frequency. (b) Oscillatory velocity profile with position (symbols) near a solid channel wall in a semi-infinite rectangular channel ($l \gg H$) showing agreement with the theoretical solution (black solid curve) to Stokes' second problem [Landau and Lifshits, 1959] with increasing frequency. (Inset) Close-up of the region from $1.5 \leq y/\delta_{AC} \leq 4.5$ to demonstrate agreement with equation (2.2) at different frequencies.

larger than those at the far field and is detailed in the inset. This is due to the relatively short channel height (200 μm) and the effect of boundary layers at the top and bottom walls of the channel affecting flow at the midplane. The corresponding values of α for the cases of 50, 200, and 800 Hz are 3.57, 7.14, and 14.3, respectively. Therefore, at the midplane, effects of channel side-walls may be neglected for distances larger than $4\sqrt{\nu/\omega}$ into the channel. Further, three dimensional flow effects can be ignored for $\alpha \geq 7.5$ when the shorter dimension is used.

Chapter 3

Particle manipulation with steady streaming flows

3.1 The Single Cylinder

Steady streaming refers to the steady secondary flows that result from oscillatory relative motion between an immersed body and a viscous liquid. In this section, the steady streaming around a cylinder in a PDMS microchannel is studied using polystyrene tracer particles ($d_p = 0.93$ μm, $\rho_p = 1060$ kg/m^3) in deionized water ($\nu = 0.95$ mm^2/s, $\rho = 1005$ kg/m^3).

For a cylinder of radius $a = 100$ μm and height $h = 200$ μm, both the oscillatory and streaming flows for frequency $f = 100$ Hz are displayed in Figure 3.1 (a). The oscillatory primary flow, is viewed at 2000 fps and is shown in the left half of Figure 3.1 (a). The distance swept by a tracer particle further than δ_{AC} from the cylinder surface is measured as $2s$ or twice the oscillation amplitude. The Stokes boundary layer thickness is defined as $\delta_{AC} = \sqrt{\nu/\omega}$, where $\omega = 2\pi f$. When viewed stroboscopically i.e framerate matched with frequency, the secondary steady streaming flow, rather than the oscillatory primary flow, is observed as shown in the right half of Figure 3.1 (a). The steady streaming flow has a quadrupolar structure, consisting of four counter-rotating vortices centered a distance L_e normal to the cylinder surface. Flow is directed toward the cylinder boundary parallel to the oscillation direction and away from the cylinder boundary perpendicular to the oscillation direction. It has been established [Riley, 2001] that the steady streaming flow pathlines are independent of the amplitude when the streaming flow characteristic velocity $U_s = \epsilon s\omega < \nu/a$, and the dimensionless amplitude $\epsilon = s/a < 0.2$. Both these criterion are satisfied for all experiments performed in this chapter.

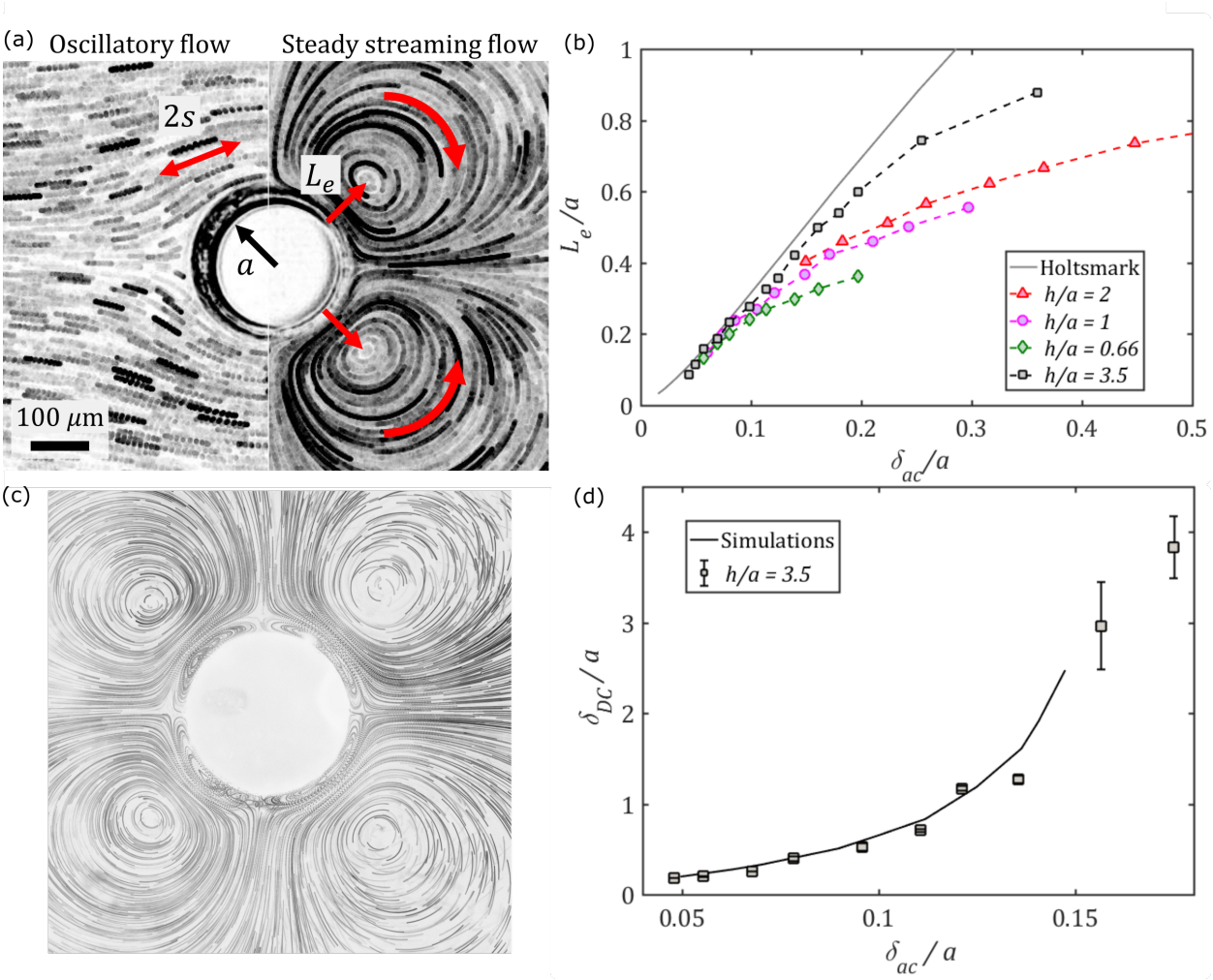

Figure 3.1: Streaming flows in lattice arrays. (a) Steady streaming around a cylindrical obstacle (radius $a = 100$ μm) in a microfluidic device. (Left) Pathlines of tracer particles captured with high-speed imaging. The distance swept by a tracer particle as the fluid undergoes one period of oscillation is measured to be $2s$. (Right) Pathlines of tracer particles captured with stroboscopic imaging showing the steady streaming profile, composed of two counter-rotating vortices. The eddy center distance from cylinder surface is L_e. (b) Experimental measurements (symbols) of L_e/a versus δ_{AC}/a for different cylinder aspect ratios h/a. Experiments converge to the analytical solution for streaming around a 2D cylinder [Holtsmark et al., 1954] (continuous line) for low δ_{AC}/a and high h/a. (c) Experimental steady streaming flow pathlines around a high aspect ratio cylinder ($h/a = 3.5$) displaying inner and outer vortex layers separated by a DC boundary layer. (d) Experimental measurements (symbols) of the dimensionless boundary layer distance from the cylinder surface (δ_{DC}/a) versus the dimensionless Stokes boundary layer for water for a cylinder of $h/a = 3.5$ and comparison with simulations (black line) in [Parthasarathy et al., 2019].

The evolution of the steady streaming flow profile with dimensionless frequency is first characterized by plotting the normalized eddy center distance L_e/a against δ_{AC}/a as shown in Figure 3.1 (b) for different cylinder aspect ratios h/a. For all aspect ratios, at relatively high frequencies ($\delta_{AC}/a \leq 0.1$), the dimensionless eddy center increases linearly, in good agreement with theory for a 2D cylinders [Holtsmark et al., 1954]. As expected, agreement with the theory improves as h/a increases, with good correspondence throughout the entire range of frequencies when $h/a = 3.5$. For low frequencies ($\delta_{AC}/a \geq 0.1$), the location of the dimensionless eddy center diverges from the approximately linear theoretical behavior and approaches a fixed value of L_e/a that increases with h/a.

For the cylinder of aspect ratio $h/a = 3.5$, two layers of quadrupolar counter-rotating vortices are observed when $\delta_{AC}/a < 0.15$ as shown in Figure 3.1 (c), referred to as the outer layer and the inner layer respectively. The inner layer vortices are characterized by L_e/a, and rotate as described above with liquid moving towards the cylinder along the oscillation direction and away from the cylinder in the direction perpendicular to it. The outer vortex layer rotates in the opposite sense. The two layers are separated by a cylindrical surface referred to as the DC boundary layer, and separated by a distance δ_{DC} from the cylinder surface.

The variation of δ_{DC}/a with δ_{AC}/a is shown in Figure 3.1 (d) for both experiments (square markers) with a cylinder of $h/a = 3.5$, and 2D simulations (continuous line) [Parthasarathy et al., 2019]. Mutual agreement is seen for $\delta_{AC} < 0.15$. For $\delta_{AC}/a > 0.16$, the δ_{DC}/a increases rapidly, becoming larger than the channel width of 5 mm and making simulations unviable. This rapid increase of the DC boundary layer to sizes comparable to the channel width are also responsible for the plateauing of L_e/a observed in Figure 3.1 (b).

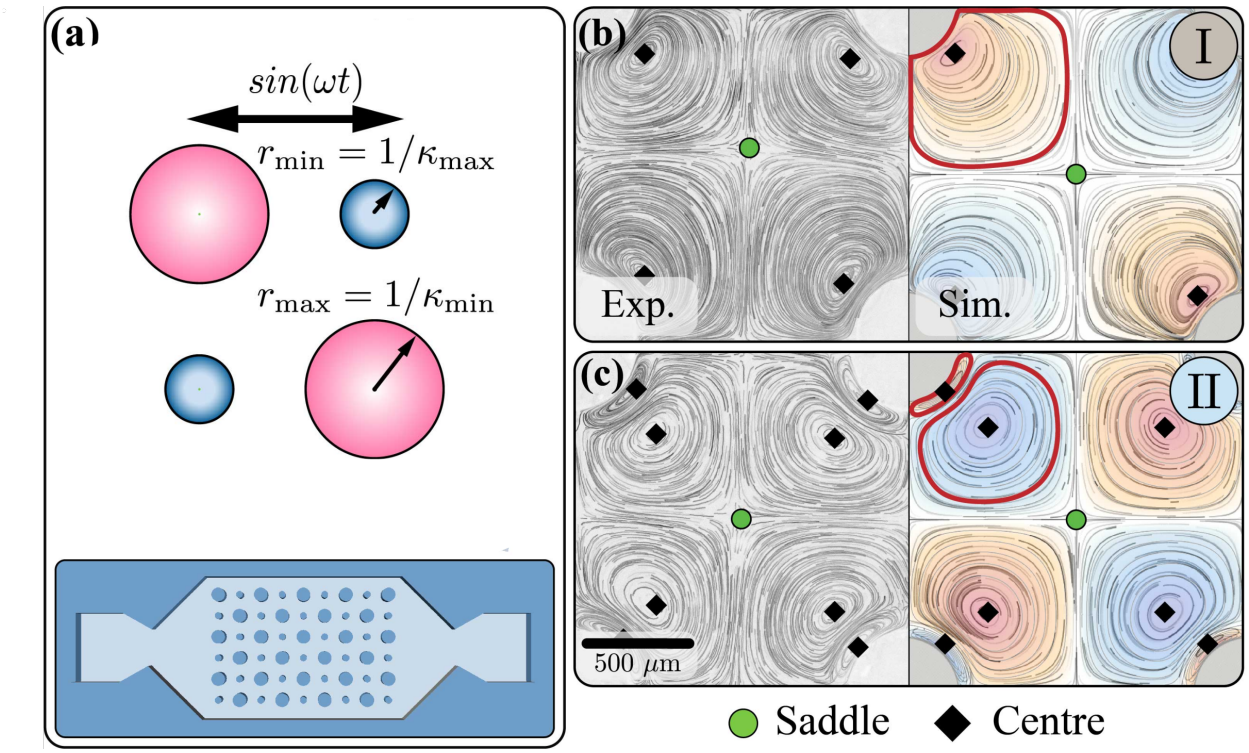

Figure 3.2: Streaming flows in lattice arrays. (a) Illustration of the lattice geometry that consists of alternating cylinders. The repeating unit cell entails cylinders of two different radii, therefore curvatures κ_{max} and κ_{min}, and a fixed centre-to-centre spacing. The experimental setup is constituted of a glass-bonded PDMS channel connected to a loudspeaker that generates oscillatory flows along the horizontal direction. (b, c) Time-averaged particle pathlines observed in experiments (left) and simulations (right), for a constant curvature lattice system with $\kappa_{max}/\kappa_{min} = 1$. Two distinct flow topologies, direct generalization of the well-known (b) single layer (referred to as Phase I, bordeaux outline) and (c) double layer (referred to as Phase II, bordeaux double outline) regimes are reported. The flow topologies are four-fold symmetric, and defining saddles (green circles) and centres (black diamonds) are marked. Blue represents clockwise rotation, while orange stands for counter-clockwise rotation. (d) Time-averaged particle pathlines observed in experiments across multiple unit cells for a lattice system with $\kappa_{max}/\kappa_{min} = 2$.

3.2 The Lattice System

To explore the effects of multiple body-curvatures on viscous streaming, a simplified lattice system shown in Figure 3.2 (a) is considered [Bhosale et al., 2020]. It consists of a 2D array of circular cylinders, with exactly two distinct curvatures κ_{max} and κ_{min}, arranged in a checkerboard pattern, and immersed in the background oscillatory flow. The center-to-center distance between adjacent cylinders is kept constant at $6.25/\kappa_{max}$ throughout the study. This setup allows multiple, discrete body-curvatures systems to be examined methodically. The streaming pathlines (for $s\kappa_{max} \ll 1$) are specified by only two parameters: the dimensionless Stokes layer thickness $\delta_{AC}\kappa_{max}$ and the curvature ratio $\kappa_{max}/\kappa_{min}$. Thus, by keeping κ_{max} fixed while modifying κ_{min} and ω, the effects of curvature variations ($\kappa_{max}/\kappa_{min}$) and flow conditions ($\delta_{AC}\kappa_{max}$) on streaming topology can be studied in a controlled, systematic manner. The computationally predicted phase space and its underlying bifurcation mechanisms were categorized via dynamical systems theory and published in [Bhosale et al., 2020].

To examine the potential for microfluidic applications, a realization of the lattice system was attempted. Three lattice microchannels were fabricated, consisting of rectangular arrays of 10×8 cylinders with $r_{min} = \kappa_{max}^{-1} = 287$ μm and $r_{max} = \kappa_{min}^{-1} = 287,\ 333,\ 571$ μm, resulting in the curvature ratios $\kappa_{max}/\kappa_{min} \approx 1.0$, 1.2, and 2.0. The channel height was $h = 2$ mm, ensuring that the $h\kappa_{min} \geq 3.5$ for all the lattices. As mentioned above, the oscillation amplitude is maintained small compared to the cylinder radii, that is $s\kappa_{max} < 0.2$.

3.2.1 Phase Space

To visualize the pathlines for the lattice system, polystyrene tracer particles ($d_p = 3.4$ μm, $\rho_p = 1060$ kg/m^3) are used with deionized water ($\nu = 0.95$ mm^2/s, $\rho = 1005$ kg/m^3) as the working fluid. The simplest case of the uniform-curvature lattice ($\kappa_{max}/\kappa_{min}$=1) is shown in Figure 3.2 (b, c). On the left, observed streaming flow pathlines for a unit cell are shown, while on the right, corresponding numerical streamlines are juxtaposed, with

blue and orange representing clockwise and counter-clockwise rotations, respectively. Of particular relevance are the flow critical points, where the velocity is zero. In two-dimensional incompressible flows, saddles (green circles) and centers (black diamonds) define the flow field, its topology and underlying dynamics. These flow features have practical relevance with regards to mixing, trapping or transport. Specifically, centers are employed to attract and retain particles [Chong et al., 2013], while saddles (and connecting streamlines) partition the flow, enabling particle separation [Thameem et al., 2017] or targeted mixing in spatially controlled chemistry [Lutz et al., 2006b].

We first observe that the cases of Figure 3.2 (b) and (c), corresponding to $\delta_{AC}\kappa_{max} = 0.19$ and $\delta_{AC}\kappa_{max} = 0.06$, both exhibit four-fold symmetry, in line with the symmetry of the unit cell. At relatively large $\delta_{AC}\kappa_{max} > 0.1$, streaming flows result in single vortices (orange, outlined in bordeaux) with distinct centers, neatly separated by saddles. This topology is an expected, direct generalisation of the single-layer regime for the single cylinder described in Section 3.1. At smaller $\delta_{AC}\kappa_{max}$, additional counter-rotating outer vortices (blue, outlined in bordeaux) appear diagonally, squeezing the original vortices into inner bounded regions adjacent to the cylinders, as shown in Figure 3.2 (c). This is a generalisation of the double-layer regime for the single cylinder. The experiments accurately replicate numerical solutions.

After establishing our approach in the uniform curvature scenario, lattice systems with multiple curvatures are explored. As illustrated over six unit cells in Figure 3.2 (d), a curvature ratio departure from unity ($\kappa_{max}/\kappa_{min} = 2$) breaks four-fold symmetry, leading to a two-fold diagonal symmetry instead. Evidently, reduced symmetry modifies flow topology, permitting the transport of material across two of the four vortices.

Systematic variation of flow conditions ($\delta_{AC}\kappa_{max}$) and curvature ratio ($\kappa_{max}/\kappa_{min} \geq 1$) yield the computationally-determined phase space of Figure 3.3 (a), in which seven distinct flow topologies are identified. Here, we experimentally probe their existence (black dots), spanning curvature ratio by means of our three lattice channels ($\kappa_{max}/\kappa_{min} = 1$, 1.2 and 2).

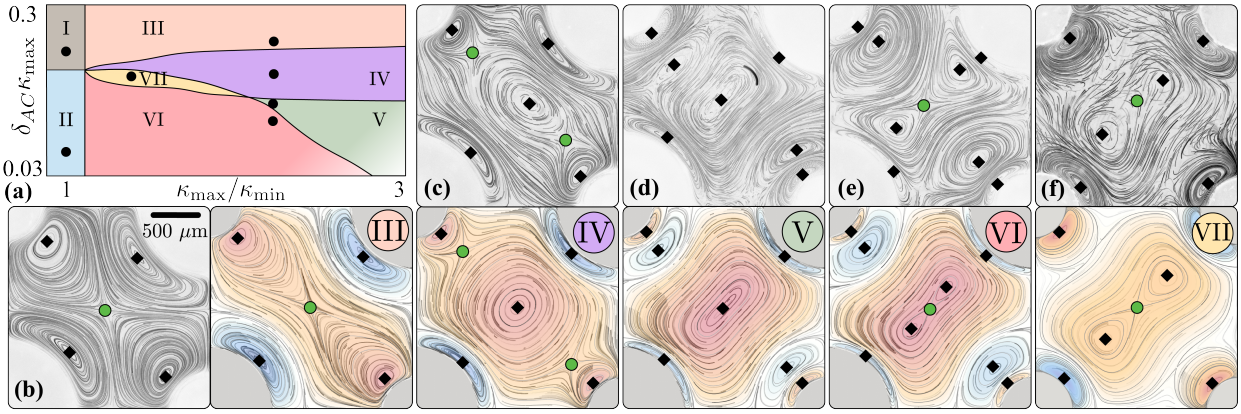

Figure 3.3: Phase space of streaming flow topologies, identified through the lattice system. (a) Phase space as a function of $\delta_{AC}\kappa_{max}$ and $\kappa_{max}/\kappa_{min}$. Black lines indicate transition boundaries between phases, and black dots indicate the specific point in the phase space reported here. Streaming flows are classified into distinct phases depending on their flow topology, characterised by saddles (green circles) and centres (black diamonds). (b) Time-averaged particle pathlines observed in experiments (left) and simulations (right) for phase III. (c - f) Similar pathlines for experiments (top) and simulations (right) for phases IV to VII. Phases in (b,c,d,e) are obtained for $\kappa_{max}/\kappa_{min} = 2$, while (f) employs $\kappa_{max}/\kappa_{min} = 1.2$. Topological markers (saddles and centres) are identified and indicate good agreement between experiments and simulations.

For a given lattice, different flow topologies (phases) can be accessed by modifying δ_{AC}/κ_{max} via the frequency ω, with low frequencies corresponding to large $\delta_{AC}\kappa_{max}$, and vice-versa. The case of $\kappa_{max}/\kappa_{min} = 1$ has already been discussed, and we refer to the topologies of Figure 3.2 (b) and (c) as Phase I and II, respectively. Of the remaining five phases, Phases III-VI are achieved with the lattice of $\kappa_{max}/\kappa_{min} = 2$, while Phase VII is achieved with $\kappa_{max}/\kappa_{min} = 1.2$.

Phase III is observed for $\delta_{AC}/\kappa_{max} > 0.2$. In this phase, the inner vortices of the smaller cylinders interact with each other and form a closed connected bicentric region (marked in orange with two centers and a saddle), as shown in Figure 3.3 (b). This bicentric region then separates the inner vortices (blue) of the larger cylinders.

Phase IV is observed when $0.09 < \delta_{AC}\kappa_{max} < 0.2$. Here, a single central vortex (orange with a center) flanked by two saddles (green) is observed, as shown in Figure 3.3(c). This central vortex then separates the inner vortices (blue) of the larger cylinders.

Phase V is observed when $0.07 < \delta_{AC}\kappa_{max} < 0.09$. In this case, a central vortex (orange with a center) identical to the one in Phase IV is present, as shown in Figure 3.3 (d). Additionally, new outer vortices (blue with centers) appear on either side of the central one, in the vicinity of the smaller cylinders.

Phase VI is seen for $\delta_{AC}\kappa_{max} < 0.07$. In this phase, a bicentric recirculation zone (orange, two centers and a saddle) is observed, as shown in Figure 3.3 (e). Additionally, outer vortices (blue with centers) are seen on either side of this recirculation zone, around the smaller cylinders.

Phase VII is realized for $\delta_{AC}\kappa_{max} \approx 0.11$ and $\kappa_{max}/\kappa_{min} = 1.2$, and shown in Figure 3.3 (f). Once again, a bicentric recirculation zone (orange, two centers and a saddle) is seen, but unlike Phase VI, no outer vortices are present near the smaller cylinders.

These streaming flows are found to well-agree with the numerical predictions. The simulations can now confidently be used to engineer a sequence of varied flow environments, which in turn can be leveraged (particularly for inertial particles, Stokes number > 0.3) for particle manipulation. In purely oscillatory flows, inertial particles are eventually trapped at vortex centers, a fact previously exploited for secure positioning [Lutz et al., 2006a]. In the presence of commonly employed finite transport flows, however, particles' residence time in the device is limited and trapping may or may not occur depending on initial location, and relative strength and topology of the streaming flow. This implies that appropriate streaming patterns, perhaps enabled by our lattice system, may be better suited than others to selectively and effectively remove incoming particles from the mean flow, thus acting as contactless, compact filters, which we present next.

3.2.2 Particle Filtration

To experimentally examine the operation of the lattice system as a filtration device, the previously described $\kappa_{max}/\kappa_{min} = 2$ lattice channel is divided into three major sections of observation, labelled as *IN*, *MID* and *OUT* (Figure 3.4 (a)). The first zone, *IN*, refers to the

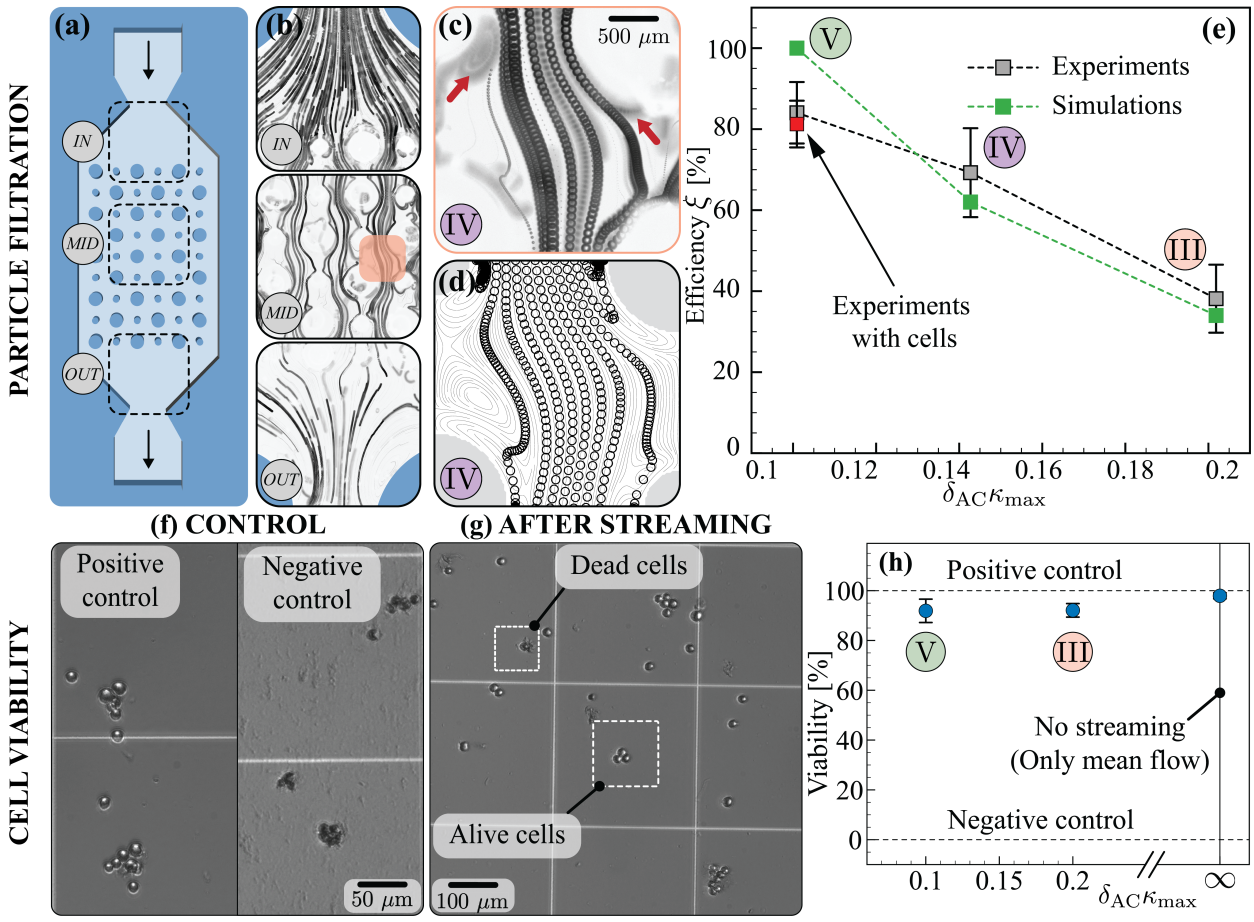

Figure 3.4: Particle filtration with streaming flows in lattice arrays. (a) Illustration of the lattice array used and the locations examined for particle concentration. (b) Particle pathlines observed in experiments within the device, as the particle suspension flows from inlet to outlet. The reduction in pathlines density, from inlet to outlet, indicates particle trapping within the device. Example particle trajectories in (c) experiments and (d) simulations for $\kappa_{max}/\kappa_{min} = 2$, $\delta_{AC}\kappa_{max} = 0.14$ (Phase IV), and $U/U_{\infty} = 360$. Particle trapping locations are indicated by red arrows. (e) Filtration efficiency ξ was measured experimentally (grey squares) and plotted against computational results (green squares) for three different $\delta_{AC}\kappa_{max}$ values, corresponding to lattice Phases III, IV and V. The single red square corresponds to ξ value obtained experimentally for filtration of human cheek cells. The effect of flow topology (lattice phase) manifests as markedly different filtration behaviours. (f, g, h) Cell viability estimation for filtration through lattice arrays. (f) Control: Representative visualization of live and dead C2C12 cells on hemocytometer after Trypan Blue exclusion test [Strober, 2015]. The cells were collected from positive control (PBS) and negative control (Ethanol), without streaming. Cells with a bright center are alive, and dead otherwise. (g) After streaming: Representative visualization of C2C12 cells on hemocytometer used for viability estimation using Trypan Blue exclusion test. Samples were collected from the device's outlet, after 30 mins of operation, across the frequency range 100-400 Hz. (h) Measured viability of C2C12 cells collected from device post operation for Phases III ($\delta_{AC}\kappa_{max} = 0.2$) and V ($\delta_{AC}\kappa_{max} = 0.1$), respectively. Dashed lines represent cell viability for control cases.

inlet of the microchannel, through which a neutrally buoyant suspension of inertial particles (d_p = 65 μm, ρ_p = 1060 kg/m^3) in 22% w/w glycerol/water solution (ν = 1.68 mm^2/s, ρ = 1060 kg/m^3) is injected at a volumetric flow rate of 0.1 ml min^{-1}. These inertial particles are tracked over a period of 50 s, and the input particle flux c_{in} across a fixed cross-section is evaluated (details in figure caption). The second zone, *MID*, refers to the core region of the lattice system where significant trapping occurs. Finally, the third zone, *OUT*, refers to the outlet of the filter, where the output particle flux c_{out} is evaluated. Filtration efficiency is then defined as $\xi = 1 - c_{\text{out}}/c_{\text{in}}$. Without oscillatory flow, virtually all particles pass through the lattice and $\xi \sim 0\%$. When instead the filter is activated by turning the loudspeaker on, complex time-averaged flow topologies emerge from the interplay between transport flow and streaming, leading to particle retention (Figure 3.4 (b)). As seen from Figure 3.4 (c), inertial particles are extracted from the mean flow, and captured within the streaming vortices (red arrows), a mechanism confirmed in simulations (Figure 3.4 (d)).

Filtering efficiency is then characterized via experiments and simulations as function of U/U_∞, which expresses the relative strengths between streaming ($U = s\omega$, oscillation velocity) and transport flow (U_∞, free-stream velocity), and $\delta_{AC}\kappa_{max}$, which determines the streaming flow topology. For a fixed value of $U/U_\infty = 360$, the impact of distinct flow topologies (Phase III, IV and V) is characterized here through the parameter $\delta_{AC}\kappa_{max}$. The obtained filtering efficiencies ξ are plotted in Figure 3.4 (e), where grey squares with error bars represent experimental measurements, and green squares represent computational results (caption for details). As seen, Phase III is the least effective filter ($\xi \sim 40\%$), Phase IV has intermediate filtration efficiency ($\xi \sim 70\%$) and Phase V is the best performing filter, with average values of $\xi = 85\%$ and peaks of $\xi = 92\%$. When compared with simulation results (green squares), we find that the efficiency trends are correctly captured. We note that for Phase V, simulations predict efficiencies close to 100%, while the experimental efficiency saturates, presenting an upper bound at 92%. We attribute this mismatch to two main factors. First, the lattice in the channel is of finite size, unlike periodic simulations.

Streaming patterns at the edges are therefore inevitably distorted, potentially allowing particles to leak through. Second, due to microfabrication constraints the lattice pillars could not be extruded so as to fully span the height of the channel. As a consequence particles are seen floating below the cylinders. While engineering optimisation may further improve performance, our focus here lies in investigating the effect of topologically distinct streaming flows.

The variation in performance with frequency is due to a combination of two effects. First is the flow topology effect, determined by $\delta_{AC}\kappa_{max}$ and leads to the particles experiencing varying flow topologies and flow curvatures. Second is the effect of changing Stokes number: $St = 2d_p^2\omega/9\nu$. This implies a modification of the role of particle inertia, encouraging or discouraging cross-streamline migration, hence trapping. For a particular value of $d_p\kappa_{max}$ the two effects are inseparable and cannot be isolated without introducing additional effects. Therefore we do not attempt to do this for the lattice system. The effect of topology is qualitatively demonstrated in the next section by comparing two geometries that are very but produce considerably different flow topologies: the single cylinder and the bullet.

Post characterization of our device's performance for rigid spherical particles, we demonstrate its suitability for soft biological entities such as cells in PBS buffer medium (($\nu = 0.96$ mm^2/s, $\rho = 1005$ kg/m^3)). First, we perform experiments for Phase V (highest filtering efficiency) with Human Buccal Epithelial cells (HBECs). These cells are chosen as their size (~ 60 μm) is comparable to the previously employed rigid particles. For HBECs we observe $\xi \sim 82\%$, similar to that of polystyrene particles, as seen in Figure 3.4 (e). This illustrates that the filtration is not restricted to hard spherical particles, and demonstrates that comparable performance can be achieved even for soft and plate-like or irregularly shaped bioparticles. Another critical factor, apart from filtration efficiency, is cell viability after filtration. However, HBECs directly extracted from human cheeks (cotton swabs) are already mostly dead [Michalczyk et al., 2004], making any conclusion on viability post filtration meaningless. Hence to show that the cells do not undergo lysis due to flow-induced

shear stresses, we perform experiments using live mouse myoblasts C2C12. We subjected the C2C12 cell suspension to a flow without oscillations (positive control, Figure 3.4 (f), and to the oscillatory flow of Phase III ($\delta_{AC}\kappa_{max} = 0.2$) and V ($\delta_{AC}\kappa_{max} = 0.1$), for 30 minutes with no mean flow. A negative control was created by incubating the cells in Ethanol for 10 minutes, Figure 3.4 (f). It should be noted that 30 minutes correspond to more than ten times the exposure time to shear encountered in regular filtration operations. Trypan Blue (TB) exclusion test [Strober, 2015] performed post device's operation (Figure 3.4 (g)) shows that the cells, even after experiencing streaming flows for significant amounts of time and at high frequencies (up to 400 Hz), remained highly viable ($\gtrsim 90\%$), as seen in Figure 3.4 (h). Additional details are deferred to Section 3.4.

3.3 The Bullet System

The bullet refers to the object formed by the extrusion of a single convex shape created by joining a semi-circle of diameter $2/\kappa_{max}$ to a rounded semi-square of same side-length, as illustrated in Figure 3.5 (a). This particular geometry was computationally designed to generate streaming features conducive to enhanced particle transport [Parthasarathy et al., 2019, Bhosale et al., 2020]. The fabricated bullet for experiments is characterized by a major radius of $1/\kappa_{max} = 0.5$ mm, smoothing radius at the corners of 0.1 mm, and extrusion height of 2.5 mm.

3.3.1 Phase Space

Analogous to the lattice system, as $\delta_{AC}\kappa_{max}$ is decreased, distinct flow topologies emerge. Here they are referred to as Phase **1**, **2** and **3**, and illustrated in Figure 3.5 (a-c). The agreement between computationally designed (top half) and experimentally realised (bottom half) flow fields is apparent.

At higher values of $\delta_{AC}\kappa_{max}$, Phase **1** is observed. In this phase, a single set of vortices

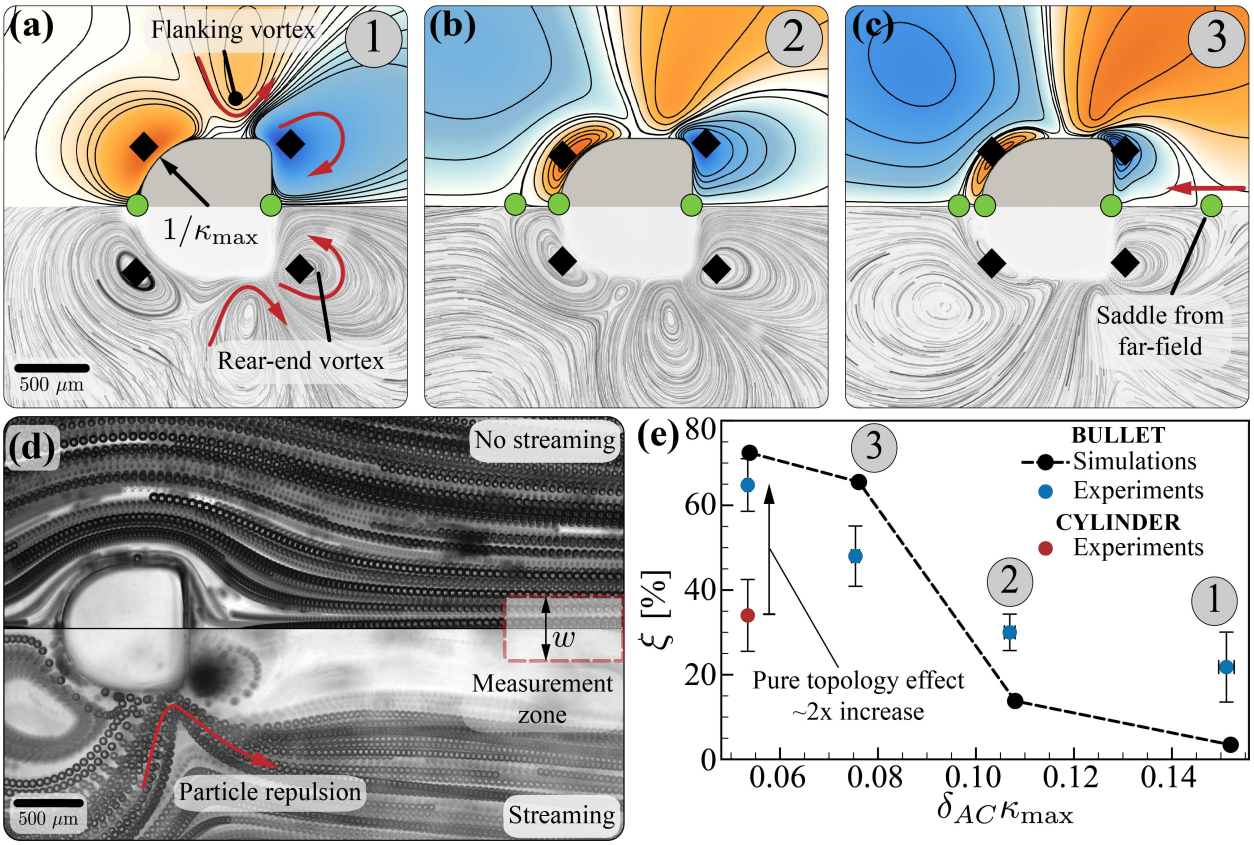

Figure 3.5: Particle separation using the bullet system. (a-c) Comparison of simulated and experimental streaming pathlines around a bullet shaped cylinder, for Phases **1**, **2** and **3**, respectively. (d) Demonstration of inertial separation of particles from the wake region at $\delta_{AC}\kappa_{max} = 0.05$. (e) Efficiency of particle separation ξ, defined as the number of particles that flow in the measurement zone, located in the wake of the bullet, relative to the unperturbed (i.e. no streaming) reference particle content, plotted against $\delta_{AC}\kappa_{max}$ for $U/U_\infty = 100$. Blue data markers represent experimental results, and dashed lines show simulation results for the bullet. the red data marker signifies the performance of a single cylinder for identical circumstances.

(center, black diamonds), which resemble the inner vortices observed for a circular cylinder, are seen on the circular front-end, as shown in Figure 3.5 (a). On the square rear-end, due to the large curvature mismatch at the corners, a set of vortices of large size and flow strength is obtained. In addition to these rear-end vortices, a new set of outer vortices flank the bullet sides. Decreasing $\delta_{AC}\kappa_{max}$ results in Phase **2**. In this phase (Figure 3.5 (b)), the original set of vortices at the circular front-end reconfigures as inner bounded vortices (thickness defined by green saddles), surrounded by outer counter-rotating vortices, similar to the double-layer regime of a circular cylinder. Additionally, a well-defined boundary appears between inner vortices on the circular front-end and flanking vortices. By further decreasing $\delta_{AC}\kappa_{max}$, the system transitions to Phase **3** (Figure 3.5 (c)), where the square-end vortices become bounded by the saddle approaching from the far-field. Consequently, flanking vortices increase in strength and curvature near the rear-end.

3.3.2 Particle Separation

To experimentally demonstrate particle separation, a steady transport flow of 22% w/w glycerol/water solution ($\nu = 1.68$ mm^2/s, $\rho = 1060$ kg/m^3) laden with neutrally buoyant inertial particles ($d_p = 65$ μm, $\rho_p = 1060$ kg/m^3) is generated past the bullet, such that the direction of flow is from the circular-end towards the square-end. Particle separation is then activated by superimposing streaming onto the mean flow. This results in the example flow topology of Figure 3.5 (d). As particles are convected around the bullet, they encounter the flanking vortices, which, as predicted, are observed to deflect particles aside. Any remaining particle that makes it to the square-end of the bullet is then readily trapped by the rear vortices. This creates a wake region mostly free from particles, referred to as the separation zone. The contrast between streaming application and lack thereof is illustrated in Figure 3.5 (d).

Quantification of particle separation is performed similarly to the lattice system, where particles are now tracked in a measurement zone (marked in Figure 3.5 (d)) before and

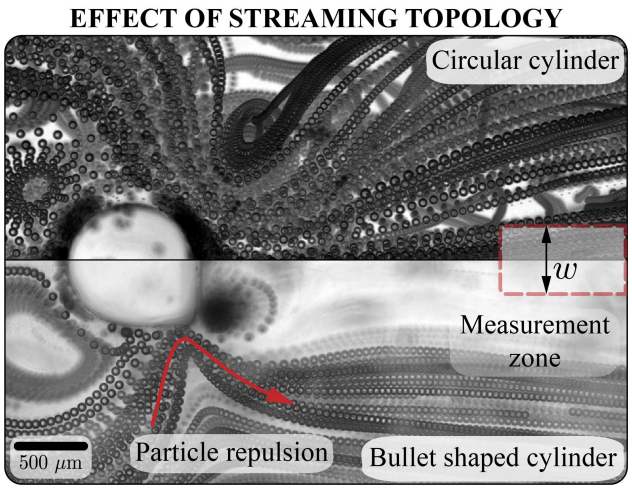

Figure 3.6: Demonstration of particle separation from the downstream region for (top) a circular cylinder and (bottom) a bullet shaped cylinder at $\delta_{AC}\kappa_{max} = 0.05$. We note that because in both cases $d_p = 65$ μm, $\delta_{AC}\kappa_{max} = 0.05$, and $St = 0.37$ is the same as well. The width w of the measurement zone used throughout this demonstration is set to match the characteristic system's length of 500 μm, corresponding to the major radius of the circular/bullet cylinder.

after streaming is applied. Here, separation efficiency $\xi = 1 - c_{out}/c_{in}$ refers to the number of particles that flow in the measurement zone (c_{out}) relative to the unperturbed (i.e. no streaming) reference particle content (c_{in}), and depends once again on U/U_∞ and $\delta_{AC}\kappa_{max}$. For the fixed value $U/U_\infty = 100$, the efficiency ξ is plotted as a function of $\delta_{AC}\kappa_{max}$ in Figure 3.5 (e). As it can be seen, different behaviors emerge across phases, with Phase **3** being evidently superior ($\xi > 70\%$), relative to the modest performance of Phase **1** ($\xi \sim 20\%$). We attribute this difference to the bounded and stronger rear-end vortices of Phase **3**, accompanied by stronger flanking vortices. Finally, we note the qualitative agreement with simulations.

The role of flow topology is clarified by contrasting particle separation of the bullet with those of the single cylinder. As previously described, the cylinder (Figure 3.1) yields distinctly different streaming flow topologies than the bullet geometry (Figure 3.5). The comparison of particle separation is shown in Figure 3.6 for all other parameters kept identical for both experiments. This includes the cylinder radius ($a = 0.5$ mm), the cylinder height

(2.5 mm), the volumetric flow rate (0.2 ml min^{-1}), the ratio of oscillatory to transport flow rates ($U/U_\infty = 160$), and the particle size ($d_p = 65$ μm) and most importantly, the Stokes number ($St = 0.37$). The effect of flow topology is thus apparent from Figure 3.6. The corresponding separation measurements for $\delta_{AC}\kappa_{max} = 0.05$ are $\xi \approx 35\%$ for the cylinder and $\xi \approx 70\%$ for the bullet, both plotted in 3.5 (e). This two-fold increase in separation performance achieved from a minor change to the object geometry, indicates the important role of the flow topology for application.

3.4 Materials and Methods for filtration experiments with biological particles

The experiments described in this section were performed jointly with Gaurav Upadhyay, and the writing of this section is credited to him.

To demonstrate the application of our technique to biological entities such as cells and test the filtration efficiency and their viability post filtration, we have performed experiments using Human Buccal Epithelial Cells (HBECs) and mouse myoblasts (C2C12), respectively.

HBECs suspensions were made by collecting cells from the cheeks of volunteers using sterilized cotton tipped swabs and were diluted in Phosphate Buffer Saline (PBS, Sigma Aldrich). The lattice device was sterilized by autoclaving at 121 °C for 45 minutes.

Although HBECs are helpful to estimate and validate the filtration efficiency of the lattice device for biological entities, we could not perform conclusive viability analysis post filtration experiments. This is due to the fact that the extraction of HBECs has a very low yield ($5 - 10\%$) of viable cells [Michalczyk et al., 2004]. Hence, to perform the cell viability analysis, we used mouse myoblasts, C2C12 cell line.

C2C12 cell line was a generous gift from Prof. Taher Saif, Department of Mechanical Science and Engineering, UIUC. Cells were cultured at 10^6 cells per T-75 flask in the presence of growth media (GM) consisting of Dulbecco's modified Eagle medium (DMEM, Sigma

Aldrich) supplemented with 10% Fetal Bovine Serum, and 1% penicillin–streptomycin. The cells were expanded until they reach $60 - 70\%$ confluency and were then detached from the flask using 0.25% Trypsin-EDTA. Post detachment, the cells were collected, mixed with equal volume of GM, and centrifuged at $150g$. Excess media was aspirated and the cell pellet formed was resuspended in GM at desired concentration and used in experiments.

To estimate the viability of the cells passing through the lattice device, we used the Trypan Blue exclusion test [Strober, 2015]. Trypan blue is a diazo dye that selectively stains cells with damaged or compromised membranes (i.e., dead cells) while leaving viable cells (i.e., live cells) unaffected. Hence, under light microscopy, cells are visually differentiated by whether they appear dark (i.e., dead cells) or bright (i.e., live cells). To test trypan blue for imaging dead cells, we created a negative control of dead cells by mixing the cell suspension with ethanol. Indeed, all the cells were stained when visualized on a hemocytometer, providing us with a standard to differentiate between live and dead cells as shown in Figure 3.4 (f).

Next, the C2C12 cell suspension was introduced into the lattice device and subjected to either (i) a pure steady flow with no oscillatory flow (positive control, Figure 3.4 (f)), or (ii) a pure oscillatory flow with no mean transport flow. For the pure oscillatory flow cases, cells were subjected to 30 minutes of oscillatory flow with frequencies corresponding to either Phase III ($\delta_{AC}\kappa_{max} = 0.2$) or Phase V ($\delta_{AC}\kappa_{max} = 0.1$). After 30 minutes of oscillatory flow, a volume of 1 ml of the cell suspension was collected from the device and then centrifuged at $1000g$. The excess media was aspirated from the vial until only 100 μl of concentrated cell suspension remained. We then mixed 100 μl of 0.4% Trypan Blue (Sigma Aldrich) with the cell suspension and the mixture was incubated at room temperature for 2 minutes. Lastly, 10 μl of this mixture was placed in a hemocytometer and visualized using bright field microscopy at $10\times$ magnification to count the dark (i.e., dead) and bright (i.e., live) cells. The process was repeated four times to measure viability, which for different set of experiments is plotted in Figure 3.4 (h).

Chapter 4

Oscillatory Inertial Focusing

4.1 Review

Inertial focusing has been primarily applied for pre-processing samples in biomedical diagnosis by separating of $5 - 30$ μm particles from suspensions of smaller particles, particularly as it relates to cancer cells, platelets or bacterial cells from blood samples. Other applications include precise sheathless alignment of particles, enrichment of dilute samples and particle exchange across solvents without mixing [Martel and Toner, 2014]. The typical inertial focusing system consists of a suspension of particles that are uniformly dispersed at the inlet, undergoing steady laminar flow through a long straight channel. At the outlet, suspended particles are no longer uniformly dispersed, but rather exit the channel at well-defined equilibrium positions in the flow. The exact focusing position varies considerably with parameters such as the particle Reynolds number ($\mathrm{Re_p}$), particle characteristics (relative size, shape and deformability), channel cross section geometry, and fluid rheology [Stoecklein and Di Carlo, 2019]. For the case of a rigid sphere suspended in an incompressible Newtonian liquid undergoing steady laminar flow, the primary design parameter is the average distance travelled by a particle before it reaches the equilibrium position. The necessary distance to be travelled for succesful focusing is estimated by the relation, $L_f = \pi D_h / \mathrm{Re_p} C_\ell$, where D_h is the hydraulic diameter and C_ℓ is the lift coefficient [Di Carlo, 2009]. For successful focusing to occur, the channel length must satisfy $L > L_f$, which implies long channel lengths ($L > 15$ cm) for small particles in low Re flows ($\mathrm{Re_p} < 0.1$).

In practical applications, channel lengths for steady flow focusing can be reduced by increasing $\mathrm{Re_p}$, which involves an increased flow velocity, larger particles (> 5 μm), or narrow channels. For focusing in unsteady flows, however, channel lengths can be reduced by implementing an oscillatory flow component. The periodic displacement generated by the oscillatory component increases the path length traveled within a finite channel to be effectively infinite. Using this principle, particles as small as 0.5 μm ($\mathrm{Re_p} \approx 0.005$) were recently focused in short channels using large amplitude, low frequency oscillatory flows [Mutlu et al., 2018]. While inertial focusing in unbounded and wall bounded steady flows are conceptually well understood and thoroughly reviewed [Stoecklein and Di Carlo, 2019, Shi and Rzehak, 2020], inertial focusing in oscillatory flows, specifically the effect of unsteady inertial effects on particle migration velocity, are comparatively unknown [Morita et al., 2017].

Early attempts towards the problem of time dependent lift were first made theoretically for a rigid sphere at small $\mathrm{Re_p}$ in an oscillatory simple shear flow [Miyazaki et al., 1995, Asmolov and McLaughlin, 1999]. Parallel numerical studies have addressed time dependent lift on a sphere in steady shear flow at intermediate $\mathrm{Re_p}$ ([Wakaba and Balachandar, 2005] and references within). Most relevant is the work of [Fischer et al., 2002, Fischer et al., 2004] which reports a finite time averaged lift on the sphere even though the driving shear flow is purely oscillatory.

4.2 Problem Formulation

Consider the idealized flow configuration illustrated in Figure 4.1 (a). A neutrally buoyant spherical particle of radius a is suspended in a Newtonian liquid of kinematic viscosity ν as it flows through a 2D channel of width l at a distance d from the wall. The underlying flow in the channel is pulsatile and consists of a weak steady flow component $\bar{\mathbf{u}}'(z')$ with centerline velocity $\bar{u}'$ and a strong oscillatory flow component $\tilde{\mathbf{u}}'(z', t')$ with centerline displacement amplitude s and angular frequency ω. The characteristic flow velocity at the channel scale is

given by $U = s\omega$. The origin of the coordinate system is taken at the center of the particle.

The relevant dimensionless numbers are the relative particle size $\kappa = a/l$, the dimensionless amplitude number $\epsilon = s/l$, and the relative magnitude of the steady flow $\bar{u}'/U$. Of primary interest are the channel Womersley number, $\alpha = l\sqrt{\omega/\nu}$, which is a relative measure of the unsteady inertial force to viscous force, and the particle Reynolds number, $\mathrm{Re_p} = a^2U/l\nu = \kappa^2\alpha^2\epsilon$, which quantifies the ratio of the particle's lateral migration velocity to its disturbance velocity. The Reynolds number ($\mathrm{Re} = Ul/\nu = \alpha^2\epsilon$) quantifies the inertial to viscous forces at the channel scale. It determines focusing position in steady flows, particularly when $\mathrm{Re} > 15$ [Schonberg and Hinch, 1989, Segré and Silberberg, 1961]. Here, the isolated effect of oscillatory flow is studied by maintaining $\mathrm{Re} < 10$ and varying α. As will be demonstrated, both Re and $\mathrm{Re_p}$ are insufficient for describing oscillatory flow focusing. Instead ϵ and α must be considered separately since they result in qualitatively different effects, especially if $\alpha > 5$.

4.3 Asymptotic Analysis

The treatment here is for a small particle ($\mathrm{Re_p} \ll 1$ and $a/l \ll 1$) in a steady 2D channel flow [Schonberg and Hinch, 1989] and is extended to the case of a harmonic purely oscillatory flow. For a particle with a certain translation velocity $\mathbf{U}'_\mathrm{p}$ and angular velocity $\mathbf{\Omega}'_\mathrm{p}$, the governing equations in terms of the position $\mathbf{r}'$, time t', disturbance velocity $\mathbf{u}'$ and disturbance pressure p' are:

$$\nabla' \cdot \mathbf{u}' = 0, \tag{4.1}$$

$$\nu\nabla'^2\mathbf{u}' - \frac{1}{\rho}\nabla' p' = \partial_{t'}\mathbf{u}' + \tilde{\mathbf{u}}' \cdot \nabla'\mathbf{u}' + \mathbf{u}' \cdot \nabla'\tilde{\mathbf{u}}' + \mathbf{u}' \cdot \nabla'\mathbf{u}' + \mathbf{U}'_\mathrm{p} \cdot \nabla'\tilde{\mathbf{u}}'. \tag{4.2}$$

The undisturbed velocity is $\tilde{\mathbf{u}}' = U(\tilde{u}e^{i\omega t'} + \tilde{u}^* e^{-i\omega t'})\mathbf{e_x}$, where $\tilde{u}$ and its complex conjugate $\tilde{u}^*$ are obtained by applying: $z' = \breve{z}' + l/2 - d$ and $\tilde{u}(z') = \tilde{u}^\dagger(\breve{z}') - \tilde{u}^\dagger(-l/2+d)$ to the standard

pulsatile flow profile for walls at $\breve{z}' = \pm l/2$:

$$\tilde{u}^{\dagger} = \frac{\cosh\left(\sqrt{i}\alpha\breve{z}'/l\right) - \cosh\left(\sqrt{i}\alpha/2\right)}{2(1 - \cosh\left(\sqrt{i}\alpha/2\right))}. \tag{4.3}$$

The transformations arise from placing the origin on a particle moving with the flow at a distance d/l from the channel wall, leading to:

$$\tilde{u} = \frac{\sinh\left(\sqrt{i}\alpha z'/2l\right)\sinh\left(\sqrt{i}\alpha(z' + 2d - l)/2l\right)}{1 - \cosh\left(\sqrt{i}\alpha/2\right)}. \tag{4.4}$$

The above equations are subject to a no-slip condition at the particle surface and the channel walls as well as regularity at the far field. That is, $\mathbf{u}' = \mathbf{U}'_{\mathrm{p}} + \mathbf{\Omega}'_{\mathrm{p}} \times \mathbf{r}' - \tilde{\mathbf{u}}'$ on $r' = a$, $\mathbf{u}' = 0$ on $z' = l$ and $z' = l - d$, and finally $\mathbf{u}' \to 0$ as $x' \to \infty$ respectively.

In what follows, the above equations are first solved for the inner problem. That is, for a finite sized particle without regard to the presence of channel walls. Assuming the particle is far smaller than the width of the channel, flow in the particle's vicinity can be treated as a simple shear flow. Afterwards, the corresponding outer problem is solved. This involves treating the far field components of the solution to the inner problem as a singularity that disturbs an otherwise 2D laminar channel flow. As will be shown, solving the outer problem yields the migration velocity of the particle center of mass.

4.3.1 Inner Problem

For the inner problem, the dimensionless position, time and rate of strain are defined $\mathbf{r} = \mathbf{r}'/a$, $t = t'\omega$ and $\gamma = \gamma'(l/U)$, respectively. The corresponding re-scaled pressure and velocities are $p = p'(l/\rho\nu s\omega)$, $\mathbf{u} = \mathbf{u}'(l/Ua)$, $\mathbf{U}_{\mathrm{p}} = \mathbf{U}'_{\mathrm{p}}(l/Ua)$ and $\mathbf{\Omega}_{\mathrm{p}} = \mathbf{\Omega}'_{\mathrm{p}}(l/U)$. The undisturbed velocity is approximated by an oscillatory simple shear flow ($\tilde{\mathbf{u}}_{\mathrm{I}} = \gamma z e^{it}\mathbf{e_x} + \gamma^* z e^{-it}\mathbf{e_x}$), where:

$$\gamma = \frac{\sqrt{i}\alpha}{2}\frac{\sinh\left(\sqrt{i}\alpha(2d - l)/2l\right)}{1 - \cosh\left(\sqrt{i}\alpha/2\right)}. \tag{4.5}$$

The momentum equations become:

$$\nabla^2\mathbf{u} - \nabla p = \mathrm{Re_p}\big(\epsilon^{-1}\,\partial_t\mathbf{u} + \tilde{\mathbf{u}}_\mathrm{I}\cdot\nabla\mathbf{u} + \mathbf{u}\cdot\nabla\tilde{\mathbf{u}}_\mathrm{I} + \mathbf{u}\cdot\nabla\mathbf{u} + \mathbf{U}_\mathrm{p}\cdot\nabla\tilde{\mathbf{u}}_\mathrm{I}\big). \tag{4.6}$$

The boundary conditions for the inner problem are $\mathbf{u} = \mathbf{U}_\mathrm{p} + \mathbf{\Omega}_\mathrm{p}\times\mathbf{r} - \tilde{\mathbf{u}}_\mathrm{I}$ on $r = 1$ and $\mathbf{u}\to 0$ as $r\to\infty$. The unsteady term is significant at leading order only if $\mathrm{Re_p}/\epsilon > 1$. Since this is not the case in experiments, this term is neglected and the equations are identical to those of the inner problem in [Schonberg and Hinch, 1989]. Consequently, the inner problem is quasi-steady and unsteadiness at the channel scale manifests at the particle scale only through the local shear rate. The solution at the far field ($r\to\infty$) is:

$$\mathbf{u} = -\frac{5}{2}(\gamma e^{it} + \gamma^* e^{-it})\frac{\mathbf{r}xz}{r^5} + O(r^{-3}). \tag{4.7}$$

4.3.2 Outer Problem

For the outer problem, the dimensionless time and rate of strain are the same as before, while the position is defined as $\mathbf{R} = \mathbf{r}'/l$. Dimensionalizing equation 4.7 and rescaling the coordinates with l, I find that the asymptotic matching condition for the disturbance velocity implies $\mathbf{u}' \sim \kappa^3 U$ as $R\to 0$. It therefore follows that $\mathbf{U} = \mathbf{u}'/(\kappa^3 U)$, $\tilde{\mathbf{U}} = \tilde{\mathbf{u}}'/U$ and $\mathrm{P} = p'(l/\rho\nu s\omega\kappa^3)$. The re-scaled momentum equation is:

$$\begin{aligned}\nabla^2\mathbf{U} - \nabla\mathrm{P} - \alpha^2\partial_t\mathbf{U} = \mathrm{Re}\big(\tilde{\mathbf{U}}\cdot\nabla\mathbf{U} + \mathbf{U}\cdot\nabla\tilde{\mathbf{U}}\big) \\ + \frac{10\pi}{3}(\gamma e^{it} + \gamma^* e^{-it})(\mathbf{e_x}\partial_Z + \mathbf{e_z}\partial_X)\delta_\mathbf{R},\end{aligned} \tag{4.8}$$

subject to $\mathbf{U} = 0$ at $Z = -d/l$ and $Z = 1 - d/l$ as well as $\mathbf{U}\to 0$ as $X\to\infty$.

The last term on the right hand side of equation 4.8 is the singularity at $R = 0$ due to the particle. The contributions of $\mathbf{u}'\cdot\nabla'\mathbf{u}'$ and $\mathbf{U}'_\mathrm{p}\cdot\nabla'\tilde{\mathbf{u}}'$ are lesser than the remaining terms

by a factor of at least κ^2 and are hence neglected at this order. The equations for a steady flow can be recovered setting $t = 0$ and $\alpha \to 0$ throughout.

In order to proceed, it is necessary to decouple the time dependent forcing in equation 4.8 from the inertial terms for tractability. To do this, a simplifying assumption that $\kappa^2 \ll \mathrm{Re} \ll 1$ is made. Although $\mathrm{Re} \sim 10$ for the experiments herein, the assumption is not thought to affect comparison with experiments. This is suggested by the steady flow case, where results derived assuming $\mathrm{Re} \ll 1$ in [Ho and Leal, 1974] are valid at least till $\mathrm{Re} = 15$. Next, I choose the following ansatz for $\mathbf{U}$ and P:

$$\mathbf{U} = \mathbf{U}_0 e^{it} + \mathbf{U}_0^* e^{-it} + \mathrm{Re}(\mathbf{U}_{1s} + \mathbf{U}_1 e^{i2t} + \mathbf{U}_1^* e^{-i2t}) + \mathrm{Re}^2(\dots),$$

$$\mathrm{P} = \mathrm{P}_0 e^{it} + \mathrm{P}_0^* e^{-it} + \mathrm{Re}(\mathrm{P}_{1s} + \mathrm{P}_1 e^{i2t} + \mathrm{P}_1^* e^{-i2t}) + \mathrm{Re}^2(\dots).$$

With the above, the time dependence of $\mathbf{U}$ and P has been made explicit. That is, all the newly defined $\mathbf{U}_i$ and P_i terms are independent of time. This implies that only $\mathbf{U}_{1s}$ and P_{1s} are relevant to long term particle migration with the rest averaging out to zero over a single oscillation cycle. The ultimate objective is therefore the evaluation of $\mathbf{U}_{1s}(\mathbf{0}) \cdot \mathbf{e_z}$ which directly yields the particle migration velocity in the laboratory frame. The oscillatory nature of forcing however, requires $\mathbf{U}_0$ and P_0 to be evaluated first. Substituting the ansatz in equation 4.8, the $O(1)$ terms give:

$$(\nabla^2 - i\alpha^2)\mathbf{U}_0 - \nabla \mathrm{P}_0 = \frac{10\pi}{3}\gamma(\mathbf{e_x}\partial_Z + \mathbf{e_z}\partial_X)\delta_{\mathbf{R}}, \tag{4.9}$$

$$\nabla^2 \mathrm{P}_0 = -\frac{20\pi}{3}\gamma \partial_X \partial_Z \delta_{\mathbf{R}}. \tag{4.10}$$

The above system of PDEs are converted into a system of ODEs through a Fourier transformation defined as:

$$\widehat{\mathbf{U}}_0(k_1, k_2, Z) = \frac{1}{4\pi^2}\int_{-\infty}^{\infty}\int_{-\infty}^{\infty} \mathbf{U}_0 e^{-i(k_1 X + k_2 Y)} \mathrm{d}X \mathrm{d}Y.$$

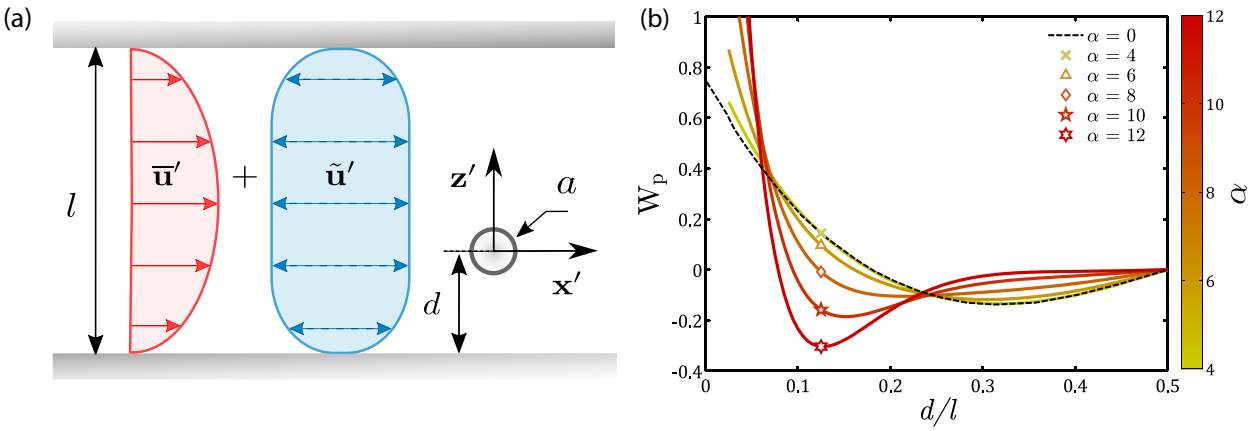

Figure 4.1: (a) Idealized illustration of inertial focusing in planar pulsatile flows between parallel plates. A spherical particle of radius a is suspended in a pulsatile flow, composed of a steady ($\bar{\mathbf{u}}'(z')$) and an oscillatory ($\tilde{\mathbf{u}}'(z', t')$) component. (b) Analytical results, (4.15) and (4.16), of the migration velocity profile along the channel width for different Womersley number pulsatile flows.

To obtain cross stream migration, it is sufficient to consider only the Z component $\mathrm{W}_0 = \mathbf{U_0} \cdot \mathbf{e_z}$. The equations 4.9 and 4.10 in Fourier space are therefore:

$$(\mathrm{d}_Z^2 - k^2 - i\alpha^2)\widehat{\mathrm{W}}_0 - \mathrm{d}_Z\widehat{\mathrm{P}}_0 = 0, \tag{4.11}$$

$$(\mathrm{d}_Z^2 - k^2)\widehat{\mathrm{P}}_0 = 0, \tag{4.12}$$

where $k^2 = k_1^2 + k_2^2$. The boundary conditions are $\widehat{\mathrm{W}}_0 = 0$ and $\mathrm{d}_Z\widehat{\mathrm{W}}_0 = 0$ at $Z = -d/l$ and $Z = 1 - d/l$. The condition at $Z = 0$ is written as:

$$\left(\widehat{\mathrm{P}}_0 \quad \mathrm{d}_Z\widehat{\mathrm{P}}_0 \quad \widehat{\mathrm{W}}_0 \quad \mathrm{d}_Z\widehat{\mathrm{W}}_0 \right)_{0^-}^{0^+} = \frac{5}{6\pi} i k_1 \gamma \left(2 \quad 0 \quad 0 \quad 1 \right).$$

To obtain the equations for $\mathbf{U}_{1s}$, the $O(\mathrm{Re})$ terms obtained by substituting the ansatz in equation 4.8 are gathered and averaged over a single time period. The resulting equation

and its divergence are:

$$\nabla^2 \mathbf{U}_{1s} - \nabla \mathrm{P}_{1s} = \big(\mathrm{W}_0 \partial_Z \tilde{U}^* + \mathrm{W}_0^* \partial_Z \tilde{U}\big)\mathbf{e_x} + \big(\tilde{U}^* \partial_X \mathbf{U}_0 + \tilde{U} \partial_X \mathbf{U}_0^*\big), \tag{4.13}$$

$$\nabla^2 \mathrm{P}_{1s} = -2\big(\partial_X \mathrm{W}_0 \partial_Z \tilde{U}^* + \partial_X \mathrm{W}_0^* \partial_Z \tilde{U}\big). \tag{4.14}$$

The Fourier transform of the above equations give:

$$(\mathrm{d}_Z^2 - k^2)\widehat{\mathrm{W}}_{1s} - \mathrm{d}_Z \widehat{\mathrm{P}}_{1s} = \; ik_1\big(\widehat{\mathrm{W}}_0 \tilde{U}^* - \widehat{\mathrm{W}}_0^* \tilde{U}\big), \tag{4.15}$$

$$(\mathrm{d}_Z^2 - k^2)\widehat{\mathrm{P}}_{1s} = -2ik_1(\widehat{\mathrm{W}}_0 \mathrm{d}_Z \tilde{U}^* - \widehat{\mathrm{W}}_0^* \mathrm{d}_Z \tilde{U}). \tag{4.16}$$

Note that forcing occurs due to $O(1)$ solutions interacting with the undisturbed flow. At this order, the boundary conditions at $Z = -d/l$ and $Z = 1 - d/l$ are $\widehat{\mathrm{W}}_{1s} = 0$ and $\mathrm{d}_Z \widehat{\mathrm{W}}_{1s} = 0$. At $Z = 0$, $\widehat{\mathrm{P}}_{1s}$ and $\widehat{\mathrm{W}}_{1s}$ along with the corresponding first derivatives are continuous.

4.3.3 Migration Velocity Profile

From the exact solutions to 4.11, 4.12,4.15 and 4.16, the lateral migration velocity can be synthesized numerically using:

$$\mathrm{W_p} = \mathrm{W}_{1s}(0) = \int_{-\infty}^{\infty} \int_{-\infty}^{\infty} \widehat{\mathrm{W}}_{1s}(0, k_1, k_2) \mathrm{d}k_2 \mathrm{d}k_1. \tag{4.17}$$

Since $\widehat{\mathrm{W}}_{1s}$ is even in both k_1 and k_2, the integration can be limited to the first quadrant so long as the result is multiplied by a factor of 4. To assist convergence of the integral, the analytical solution for $k \gg 1$ was used:

$$\widehat{\mathrm{W}}_{1s}(0) = \frac{15k_1^2\alpha^2}{64\pi k^5} \Re\left[\frac{i\gamma \cosh(i^{3/2}\alpha(d/l - 1/2))}{\cosh(i^{3/2}\alpha/2) - 1}\right], \tag{4.18}$$

where $\Re$ denotes the real part.

The variation of the particle migration velocity $\mathrm{W_p}$ with d/l for different values of the

Womersley number is shown in Figure 4.1 (b). For small Womersley numbers ($\alpha \leq 5$), the migration velocity profiles are very similar to one another and, more importantly, nearly identical to the migration profile expected for steady flow, within a numerical factor of exactly one-half [Asmolov, 1999]. The factor of one-half arises from the time average of the $\cos^2 t$ term over a single oscillation period. For large Womersley numbers ($\alpha > 5$), the migration velocity increases near the channel walls ($d/l < 0.1$) and becomes negligible in the central region of the channel ($0.2 < d/l < 0.5$). The equilibrium focusing position can be located by determining the null point for each of the migration velocity profiles. The value $\alpha = 5$ is straightforward given that the undisturbed velocity profile (4.3) changes dramatically beyond this threshold. Less so is the null point which moves closer to the wall with increasing α as a result of opposing effects (see Figure 4.3 (a)). Due to increasing α, velocity gradients become larger near the walls and smaller near the centerline (4.3). This implies the wall interaction force becomes relatively stronger but is also confined closer to the wall.

Note that results in Figure 4.1 (b) are not valid for $d/l \to 0$ and breakdown when $d/l \sim \kappa$ as this violates the assumed separation of scales between the outer and inner problems. The oscillatory flow induced inertial lift on a sphere close to a wall has been addressed numerically by [Fischer et al., 2004].

4.4 Experimental Methods

Experiments were performed in a straight channel with a rectangular cross section of high-aspect ratio fabricated from a piece of aluminum sheet metal through wire electrical discharge machining. The total channel length L was 4 cm and the height was 2.5 mm. The channel walls were wet sanded to smoothness resulting in a width l of 300 μm with $< 0.2\%$ deviation from parallel plates along the channel length. The top and bottom walls of the channel were completed by adhering transparent packaging tape to the sheet metal. The tape was

perforated at the channel inlet and outlet and microfluidic tubing was inserted and sealed with epoxy.

A volumetric flow rate of 20 μL/min was used throughout this study unless specified otherwise. For the given channel dimensions, this flow rate corresponded to a maximum flow speed $\bar{u}' = 0.54$ mm/s. The frequencies used here range from $25 \leq f \leq 500$ Hz. The maximum values of the oscillatory velocities ranged from 34 to 89 mm/s and were much larger than the steady flow velocity ($U \gg \bar{u}'$).

Polystyrene particles were density-matched in an aqueous glycerol solution (23% w/w) with density $\rho = 1060$ kg/m^3 and kinematic viscosity $\nu = 1.687$ mm^2/s. Three different suspensions with particle radii $a = 5.4,\ 8.1$, and 10.4 μm were used. Particle suspensions were in the dilute limit with volume fractions ranging from 0.02% up to 0.05%. Particles were imaged at the channel midplane (height) with bright-field microscopy using a 10$\times$ objective lens with a depth of focus of 10 μm. The acquisition frequency of 5 Hz and exposure time of 100 μs was used to monitor the rectified component of particle displacement. The imaging location was at the lengthwise center of the channel, or 2 cm away from the inlet. The residence time of a particle is defined as the shortest time to travel from the inlet to the region of observation and is given by $t_R = L/2\bar{u}' = 37$ s. However, during this time, the maximum total distance travelled by a particle will take into account the oscillatory component, since $U \gg \bar{u}'$, therefore it is estimated that $L_R = 4sft_R$. Therefore, here L_R is referred to as the resident length travelled before observation and ranges from 0.8 to 2.1 m.

4.5 Experimental Results

The dynamics of inertial focusing in planar pulsatile flows is qualitatively demonstrated in the space-time plot, shown in Figure 4.2 (a). Here, suspended particle concentrations at each position along the channel width are represented in grayscale, where light gray corresponds to a low concentration of particles and dark gray corresponds to a high concentration of

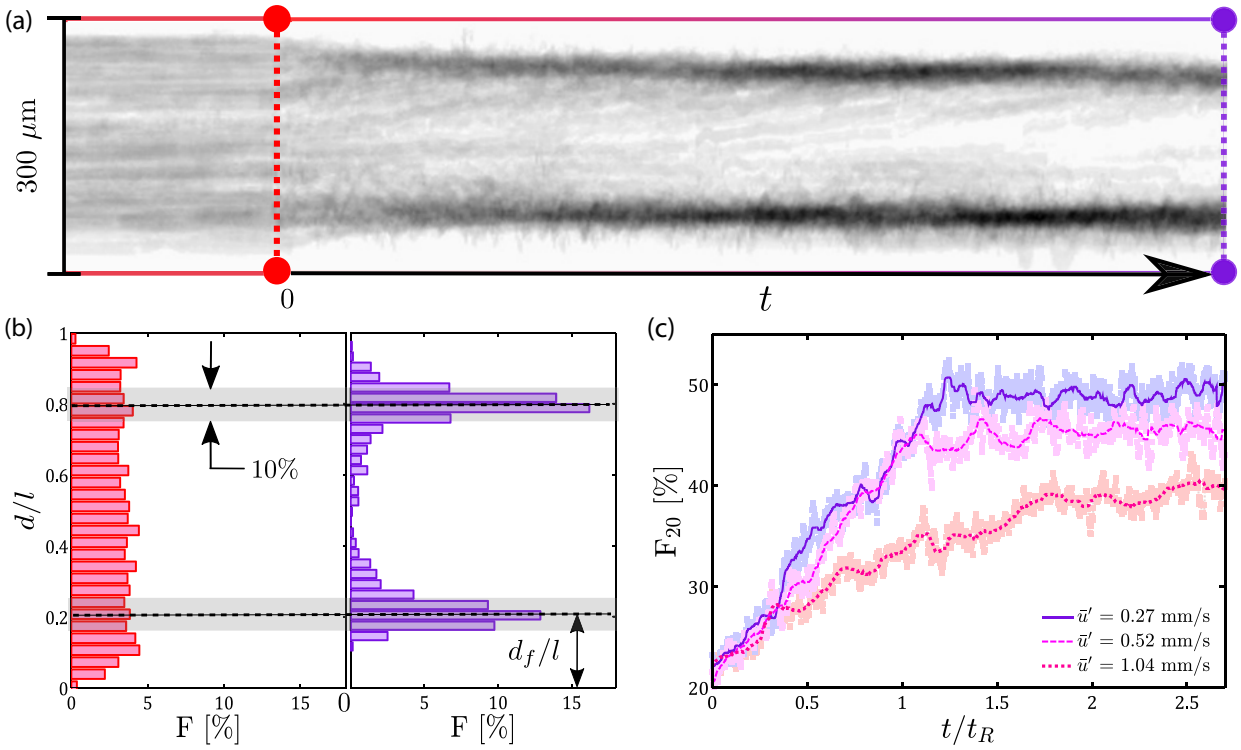

Figure 4.2: (a) Space-time plot of suspended particles migrating to equilibrium positions under pulsatile flow. (b) Histograms of the particle distribution along the channel width for (left) steady flow and (right) pulsatile flow. The focusing efficiency, denoted by F_{20}, quantifies the fraction of particles found within a distance $l/10$ of both focusing positions. (c) Transient focusing efficiency for different steady flow velocities. The efficiency reaches a steady value for all cases after $t/t_R > 1.5$.

particles. Initially, particles are uniformly distributed along the span-wise direction as they are transported by a purely steady unidirectional flow. After the oscillatory component is introduced ($t = 0$), concentration gradients emerge as particles migrate across streamlines and localize into two dark bands.

Histograms of particle positions along the channel width, obtained from digital particle identification and tracking techniques, quantitatively demonstrates the transformation from a uniformly dispersed suspension to a focused suspension, shown in Figure 4.2 (b). The particle number distributions are normalized by the total flux of particles observed. The peaks of the distribution correspond to the localization of particles after migration across streamlines. The peak positions are the measured equilibrium focusing positions, defined

by their distance d_f/l from the channel walls. Since this measurement depends on the local width of the channel, particle tracking was used to extract the steady flow profile that was then fit to a parabolic curve, whose fitting constants determine the precise centerline and local channel width. The focusing efficiency, denoted by F_{20}, quantifies the total fraction of particles located within a distance $l/10$ of both focusing positions and is indicated by the shaded band, shown in Figure 4.2 (b). Therefore, F_{20} ranges from 20%, corresponding to a uniformly dispersed suspension, up to 100%, corresponding to the complete localization of particles at the focusing positions.

When observing a fixed position along the channel length, the steady flow component determines both, the absolute time required for the particle distribution to reach steady state, and the eventual focusing efficiency. For example, the focusing efficiency for $\alpha = 4$, $\kappa = 0.018$, $\mathrm{Re_p} = 0.014$, and the steady flow speeds $\bar{u}'$ of 0.27, 0.52, and 1.04 mm/s initially starts from 20% and increases with time, shown in Figure 4.2 (c). The residence times t_R associated with the steady flow speeds are 74, 37, and 18.5 s, respectively. The rate of increase in the focusing efficiency is initially identical for all steady flow speeds and approaches zero by $t/t_R = 1.5$. As expected, the steady state F_{20} increases with residence time due to the larger focusing length travelled and reaches maximum values of 50%, 45%, and 40%, respectively.

Focusing positions and focusing efficiency are measured only after the particle distributions reach a steady state. Henceforth, the data presented will correspond to a steady state with a steady flow speed of $\bar{u}' = 0.54$ mm/s with a residence time of $t_R = 37$ s. To ensure steady state, measurements are only made after pulsatile flow is applied for 100 s ($t/t_R > 2.5$), after which the particle distribution is measured and synthesized over another 100 s interval.

The data (symbols) for focusing position and focusing efficiency are mean values (multiple experiments and time-averaged during the 100 s interval). The colored regions represents the error, estimated here as one-half of the maximum difference of any measurement from

the mean. For example, the comparison between instantaneous values and mean value are evident in Figure 4.2 (c).

The focusing position d_f/l decreases as the Womersley number increases above $\alpha > 5$, shown in Figure 4.3 (a). For small κ, there is good agreement between experimental measurements ($\kappa < 0.02$) and theory ($\kappa = 0$) as indicated by the dashed line. The theoretical focusing positions are determined by null points in the migration velocity curves, shown in Figure 4.1 (b). For large κ, the deviation of experimental measurements ($\kappa > 0.02$) from theory ($\kappa = 0$) increases with particle size. The corresponding focusing position for a given Womersley number occurs farther away from the channel wall, while preserving the qualitative theoretical ($\kappa = 0$) trend. That is, the focusing positions continue to approach the channel wall for Womersley numbers above $\alpha > 5$. While the focusing position can be described quite accurately with advanced computational methods for an individual particle, the evaluation of focusing efficiency requires a comprehensive statistical analysis of particle positions for many particles across all initial conditions. This is made possible only with an experimental approach.

The focusing efficiency was measured for different particle sizes and Womersley numbers, shown in Figure 4.3 (b). Here, the focusing length of $L_R = 2.1$ m was maintained across frequencies by independently adjusting the amplitude and frequency such that the product of the oscillatory velocity magnitude (U) is equal to a constant. For small Womersley numbers ($\alpha < 5$), the focusing efficiency ranges from 50% to 90% for the particle Reynolds numbers of 0.01 and 0.07, respectively. The high extent of focusing efficiency, $F_{20} > 80\%$ for $Re_p = 0.071$, illustrates the efficiency of oscillatory flows for inertial focusing. For large Womersley numbers ($\alpha > 5$), the focusing efficiency decreases monotonically and approaches 20%, or that of a uniformly dispersed suspension, for the smallest particle size.

The focusing efficiency was also measured for different oscillatory amplitudes and Womersley numbers, shown in Figure 4.3 (c). Here, the relative particle size of $\kappa = 0.035$ was maintained a constant throughout. Once again, for small Womersley numbers ($\alpha < 5$), the

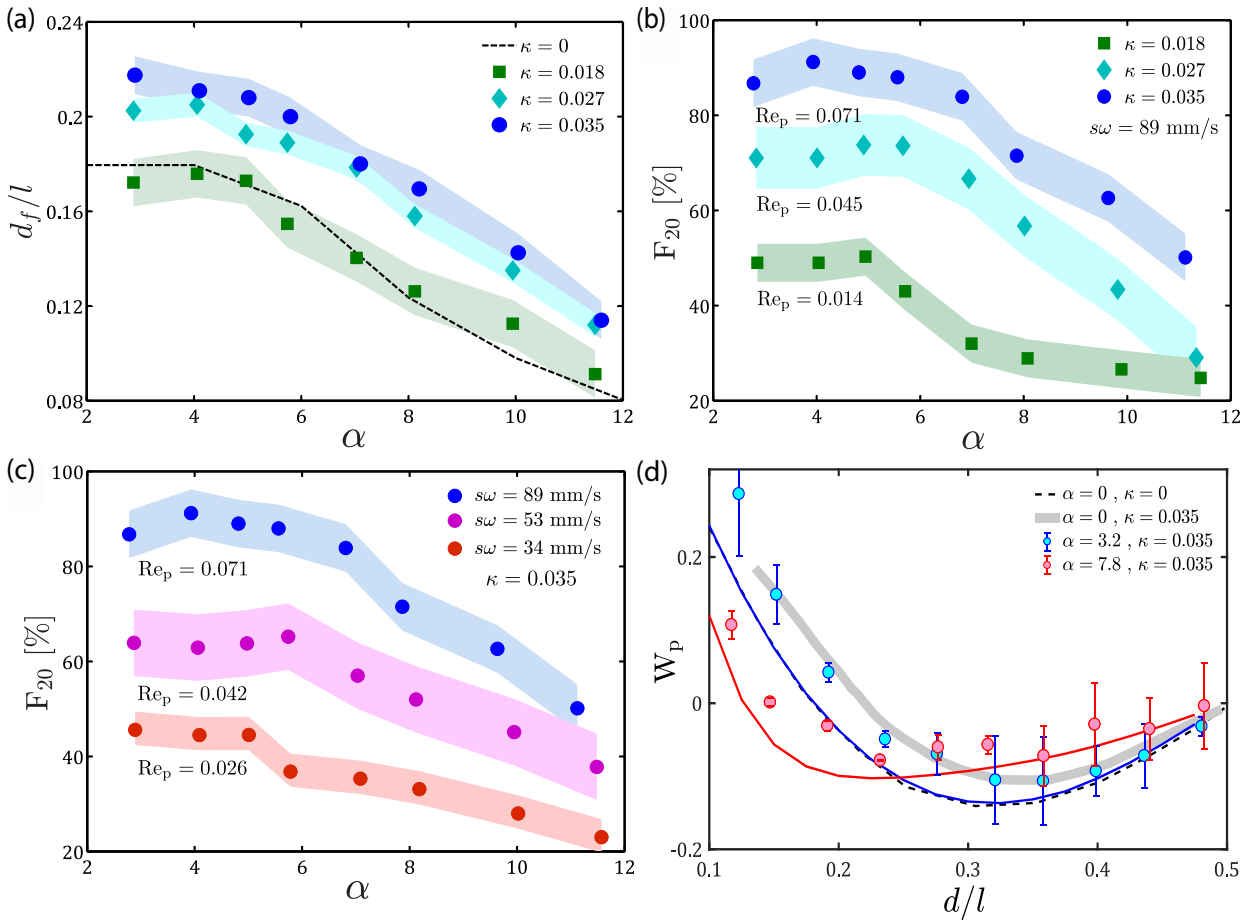

Figure 4.3: (a) The focusing position for different relative particle sizes as a function of Womersley number. The experimental measurements (symbols) are similar to the analytical predictions (dashed) obtained from Figure 4.1 (b). The discrepancy is due to finite particle size ($\kappa > 0.02$). (b) The focusing efficiency for suspensions of different relative particle sizes as a function of Womersley number. The oscillatory velocity amplitude (U) is maintained constant across throughout. (c) The focusing efficiency for a suspension of a fixed particle size as a function of the Womersley number for varying oscillatory velocity amplitude. The oscillatory velocity amplitude is kept constant for a single curve but varied across curves. (d) The migration velocity profile for a low (blue) and high (red) Womersley number. The experimental measurements (symbols) are compared to corresponding theoretical results for point particles in a oscillatory flow (red/blue solid, (4.15) and (4.16)), as well as, to point (black dashed) and finite-size (gray stripe, [Asmolov et al., 2018]) particles in a steady flow.

focusing efficiency has a similar range of 45% to 90% for the oscillatory velocities of 34 mm/s and 89 mm/s, respectively. For large Womersley numbers ($\alpha > 5$), the focusing efficiency decreases monotonically and approaches 20% for the lowest oscillatory amplitude. From both cases, for a fixed Womersley number, a larger $s\omega$ or κ value determined a higher extent in the F_{20} value, in agreement with inertial focusing in steady flows.

A distinct advantage of studying inertial focusing in oscillatory flows compared to focusing in steady flows is that the migration of individual particles across a large resident path length can be clearly observed and tracked. Therefore, it is possible to accurately, measure the average migration velocity profile across the channel width; something that is not easily achieved in steady flows due to practical constraints of resolving single particles over a large field of view. The guiding principle is, once again, the decoupling of travelled distance from displacement [Vishwanathan and Juarez, 2020]. The averaged migration velocity at each spanwise position for a low frequency ($\alpha = 3.2$) and high frequency ($\alpha = 7.8$) pulsatile flow and relative particle size of $\kappa = 0.035$ is shown in Figure 4.3 (d).

The migration velocity was measured by tracking the position of many individual particles ($N \approx 100 - 1000$ per experiment) during the transient regime, i.e., $t/t_R < 1$ in Figure 4.2 (c).

Experimental measurements (symbols) compare well with analytical results for point particles (solid, (4.15) and (4.16)) in an oscillatory flow. Here, symbols represent average values and error bars represent one standard deviation from the mean. A precise match with half the magnitude of numerical results for finite-sized particles (gray stripe, $\kappa = 0.035$, [Asmolov et al., 2018]) in a steady flow is observed for the low frequency case.

See comment about the numerical factor of one-half in section §3.3.

4.6 Discussion

The Womersley number is an important parameter for pulsatile flows [Dincau et al., 2019]. It defines the ratio of the channel width to the Stokes boundary layer thickness and determines the velocity profile for unsteady laminar flows. While inertial focusing in pulsatile flows provides an opportunity for reduced channel lengths and pressure drops in biomedical applications, it first requires understanding the direct link between transient inertial forces and particle migration velocity profiles in unsteady laminar flows.

In general, the focusing efficiency is independent of α for small Womersley numbers ($\alpha < 5$), shown in Figure 4.3 (b) and 4.3 (c). The constant focusing efficiency for these cases is due to the migration velocity profiles, which are also independent for $0 < \alpha < 5$, shown in Figure 4.1 (b). However, for large Womersley numbers ($\alpha > 5$), the focusing efficiency decreased monotonically with increasing α, shown in Figure 4.3 (b) and 4.3 (c). The decrease in the focusing efficiency for these cases is due to the migration velocity profiles, which become increasingly weak at the center of the channel for $\alpha > 5$, shown in Figure 4.1 (b).

For focusing in steady laminar flows, the particle Reynolds number determines the magnitude of the particle migration velocity, that is, a larger $\mathrm{Re_p}$ corresponds to increased focusing efficiency. In contrast, $\mathrm{Re_p} = \kappa^2\alpha^2\epsilon$ does not always directly correlate with improved focusing efficiency in unsteady oscillatory flows. In fact, above a critical Womersley number ($\alpha > 5$), the focusing efficiency decreases with increasing $\mathrm{Re_p}$ if only α is increased. Therefore, for the purposes of inertial particle focusing, it is best to maintain $\alpha < 5$. For $\alpha > 5$, although the focusing efficiency decreases, the migration velocity profile suggests that particles migrate away from the channel wall with speeds that increase directly with Womersley number. This effect could be leveraged in efforts to mitigate the fouling of surfaces without affecting the bulk concentration profile.

Chapter 5

Synchronous Oscillatory Electro-Inertial Focusing

5.1 Problem Formulation

Consider the idealized configuration illustrated in Figure 5.1 (a). A rigid, neutrally buoyant, insulating, negatively charged spherical particle of radius a and zeta potential ζ_p is suspended in a Newtonian liquid of kinematic viscosity ν, ionic conductivity σ, permittivity ε as it flows through a 2D insulating channel with width l and zeta potential ζ_w. The underlying flow in the channel consists of a steady flow component $\bar{\mathbf{u}}'(z)$, a pressure driven oscillatory flow component $\tilde{\mathbf{u}}'(z,t')$ and an electro-osmotic oscillatory flow component $\tilde{\mathbf{u}}'_E(z,t')$ that is caused by a uniform oscillating electric field $\tilde{\mathbf{E}}'(t)$. The oscillatory flows and field have the same frequency f and angular frequency $\omega = 2\pi f$. The respective centerline amplitudes are $\bar{u}$, U, $s_E\omega$ and angular frequency ω. The amplitude of the electric field is E. The phase difference between the electro-osmotic velocity and the oscillatory flow is given by ϕ.

5.2 Experimental Methods and Parameters

5.2.1 Microchannel

The experimental setup is shown in Figure 5.2. The flow manifold is a straight rectangular microchannel made of PDMS (10:1, resin:crosslinker), demolded from 3D printed mold (SLA, Form3) that was treated with silicone mold release. Four holes are made with a biopsy punch (1mm), two at each end of the channel. The channel is then bonded to a glass slide

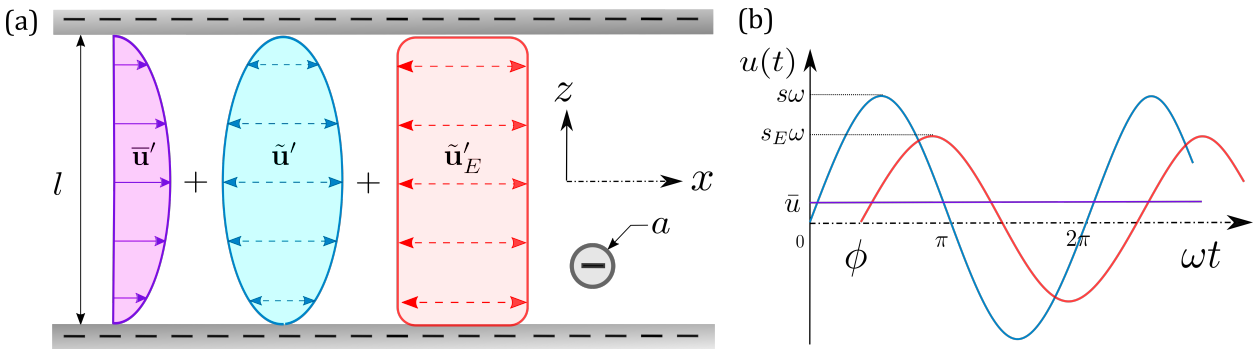

Figure 5.1: (a) Idealized illustration of synchronous oscillatory electro-inertial focusing (SOEIF) of an insulating, negatively charged, neutrally buoyant spherical particle in an insulating, negatively charged 2D channel. (b) Illustration of the centerline velocities versus time for each flow component.

after 1 minute of oxygen plasma treatment. After bonding, a few drops of uncured PDMS are poured along the edges of the PDMS-glass interface and subsequently cured for better bonding and sealing. Two multi-stranded copper wires with stainless steel pins are used for the electrodes. Polyethylene tubing is inserted at the inlet and outlet, followed by the pins to create the electrodes. The tubing and electrode interfaces are sealed with epoxy (Loctite 5 min).

5.2.2 Solution

The laboratory temperature is maintained at 20°C. The solution used is 22% glycerol in water with 0.1 mM NaCl which corresponds to a kinematic viscosity $\nu = 1.68$ mm^2/s, density $\rho = 1060$ kg/m^3 [Glycerine Producers' Association, 1963], conductivity $\sigma = 0.12$ mS/cm [Liao et al., 2017], permittivity $\varepsilon = 6.55 \times 10^{-10}$ F/m [Behrends et al., 2006] and effective ionic diffusion coefficient $D = 1.15 \times 10^{-9}$ at 50 Hz. Polystyrene tracer particles (Spherotech) with radii $a = 0.5, 1.7, 2.6$ μm (diameters of $1, 3.4, 5.2$ μm) are mixed in volume fractions of $\psi = 2, 6, 20 \times 10^{-5}$ respectively. The corresponding Debye length, is $\lambda_D = \sqrt{\frac{\varepsilon k_B T}{2z^2 e^2 C_0}} \approxeq 16.8$ nm.

5.2.3 Activation

To produce the flow, a speaker based oscillatory source capable of producing $s \geq 100$ μm and $U \leq 8$ cm/s across the frequency range $25 \leq f \leq 800$ Hz in the PDMS microchannels and detailed in [Vishwanathan and Juarez, 2020] is used along with a syringe pump operated at $10 - 20$ μL/min, that produces a steady flow of centerline speed $\bar{u} = 1 - 2$ mm/s. A high voltage amplifier (TREK 677) with a gain of 1000$\times$ is used to generate an oscillatory electric field. The high voltage line is supplied from the amplifier to two alligator clips that then grip the copper strands of either electrode. The sinusoidal input voltages ($V(t)$ with $0 - 5$ Vpp) to both the speaker and amplifier are supplied by a function generator (RIGOL DG812) with a controlled phase difference Φ. The oscillatory electro-osmotic flow emerges as a combined result of the oscillatory electric field, the fixed charges at the channel walls and the ions in the working liquid with $s_E \leq 20\mu$m at 50 Hz.

The majority of experiments are performed at $f = 50$ Hz, $a = 0.5$ μm, and a field amplitude $E = 50$ kV/m corresponding to 2000 Vpp applied with a gap of 2 cm.

5.2.4 Optics

The dynamics of the particles under the influence of the combined electric field and pressure driven flow are visualized with brightfield imaging using an inverted microscope (Nikon Eclipse Ti2). For measuring particle focusing, a 4$\times$ lens is used to image particles near the channel outlet. For measuring migration velocity, a 10$\times$ magnification is used to image particles near the channel inlet. All data is obtained at the channel midplane.

5.2.5 Hydrodynamics

For the parameter ranges used here, velocity magnitudes are such that: $\bar{u}, s_E\omega \ll U$ implying that purely hydrodynamic effects are largely determined by the pressure driven oscillatory flow. The length dimensions are likewise related by $a \ll l \ll h \ll L$. This implies that flow

inside the channel is fully developed and the flow is quasi 2D at the midplane, where data is obtained.

The channel Reynolds number is given by $\mathrm{Re} = Ul/\nu \leq 10$ for all experiments considered here implying that the flow profile is unaltered by inertial effects. The Womersley number $\alpha = l\sqrt{\omega/\nu}$, governs transient hydrodynamic effects at the channel scale, and therefore determines $\tilde{\mathbf{u}}'(z,t)$ and $\tilde{\mathbf{u}}'_E(z,t)$. For a frequency of $f = 50$ Hz, $\alpha = 4.1$ which corresponds to a quasi-steady flow profile [O'Brien, 1975]. Taken together, the ranges of Re and α imply that for $-l/2 + O(\lambda_D) < z < l/2 - O(\lambda_D)$, the pressure driven flow is given by:

$$\tilde{\mathbf{u}}'(z,t) \approxeq U(1 - (2z/l)^2)\sin(\omega t), \tag{5.1}$$

and the electro-osmotic flow is given by :

$$\tilde{\mathbf{u}}'_E(z,t) \approxeq s_E\omega \sin(\omega t + \phi). \tag{5.2}$$

The Stokes number $St = 2a^2\omega/9\nu$ governs transient hydrodynamic effects at the scale of the particle. For these experimental parameters $St \leq 3 \times 10^{-4} \ll 1$ implying irrelevance [Michaelides, 1997]. Similarly the particle Reynolds number, which governs inertial effects at the particle scale takes values in the range $10^{-4} - 10^{-3}$. For this range, forces responsible for inertial migration are weaker than Brownian motion [Mutlu et al., 2018].

5.2.6 Electrokinetics

The principal electrokinetic effects relevant to these experiments are electro-osmotic flow at the channel scale and electrophoresis at the particle scale. The amplitude of the electro-osmotic flow in terms of electric field is $\varepsilon\zeta_w E/\mu$. Likewise the electrophoretic slip velocity amplitude at the surface of the particle is $\varepsilon\zeta_p E/\mu$. Here ζ_w and ζ_p are the zeta potentials of the wall and the particle, respectively.

During the low frequency ($\alpha < 5$) experiments performed herein, it is not possible to separate the effects of electrophoresis and electro-osmosis because the electro-osmotic flow can only be visualized using tracer particles. For this reason, for each experiment the amplitude of the combined measurement is reported as:

$$s_E\omega = \varepsilon(\zeta_p + \zeta_w)E/\mu \tag{5.3}$$

However, at high frequency ($\alpha \gg 5$) the electro-osmotic flow component is suppressed near the channel center. This principle was used to measure the particle zeta potentials in a manner similar to that described in [Amer Cid et al., 2021]. For this, the oscillatory motion of particles near the channel center for an electric field amplitude of $E = 125$ kV/m, and frequency of 800 Hz ($\alpha = 16.5$) was tracked using a global-shutter high speed camera working at 16000 fps. For particle radii $a = 0.5,\ 1.7,\ 2.6$ μm, the particle zeta potentials obtained were $\zeta_p = -22 \pm 2, -39 \pm 8, -53 \pm 5$ mV, respectively.

The electro-osmotic flow velocity amplitude can therefore be obtained by subtracting the electrophoretic part. The ratio of the electric potential energy to the thermal potential energy ranges $0.8 \leq e\zeta_p/k_BT \leq 2.0$. For this range, the nonlinear electrokinetic effects are weak [Hossan et al., 2018]. The ratio of viscous to electrokinetic stresses is estimated by $Q = sa/s_El < 0.2$ for the experimental parameter range accessed here.

The colloidal timescales of significance are Maxwell-Wagner scale given by $\tau_{MW} = \varepsilon/\sigma \approxeq$ 65 ns and the volume diffusion/concentration polarization timescale $\tau_{VD} = a^2/2D \approxeq 0.2$ ms [Shilov et al., 2000]. Both these timescales are significantly smaller than the oscillatory time period of 20 ms at 50 Hz, implying quasi-steady electrokinetic behavior at the particle scale.

5.2.7 Phase difference: Φ vs ϕ

It is worth highlighting the difference between Φ and ϕ. The phase difference set by the function generator between the voltage applied to activate the electric field and the voltage

applied to the speaker is Φ and can be experimentally controlled. The actual phase difference between electro-osmotic oscillatory flow and the pressure driven oscillatory flows is ϕ and it cannot be controlled experimentally. All subsequent results are reported in terms of Φ only, the relationship between Φ and ϕ is elaborated below.

The principal relation between ϕ and Φ is $\phi = \Phi + \phi_s + \phi_{sE}$, where ϕ_s is a phase shift associated with the startup of the pressure driven flow and ϕ_{sE} the phase shift associated with the startup of the electro-osmotic flow.

The electric field, is exactly synchronized with the applied voltage and there is no measurable phase lag for the frequencies considered here, that is $\phi_{sE} \approx 0$. The high voltage output of the amplifier was verified to be synchronized with the voltage output of the function generator correct to 1 microsecond. Further, since the channel materials: PDMS, glass and polyethylene are completely insulating, their conductance and inductance are negligible. The capacitive and resistive impedances of the fluid in the channel can be estimated by $X_c = L/\varepsilon lh\omega = 2 \times 10^{11}\ \Omega$ and $R = L/\sigma lh = 4.4 \times 10^6\ \Omega$ indicating that load is almost entirely resistive. This implies that the current and electric field inside the channel are exactly synchronized with the voltage. It follows that the electro-osmotic flow velocity and the electrophoretic particle migration is anti-synchronized owing to the negative charges of the channel wall and particle.

Likewise, the input voltage to the speaker is measured to be synchronized with the output of the function generator. The relatively large wavelengths of the frequencies used here ($\lambda = c/f = 30$ m) imply that the phase shift effects within the fluid and other mechanical components such as the tubes, and adapter are also negligible. Nevertheless, the effects of ϕ_s are not necessarily negligible. This is because, all uncertainty about the relationship between Φ and ϕ arises during the startup of the speaker. The phase characteristics of the speaker cone excursion as a function of input voltage are not known and this evaluation is quite involved and therefore not performed here. To minimize the uncertainty associated with the speaker startup, the speaker activation protocol is standardized. Before each dataset the

speaker voltage is set to 0 and the cone is allowed to reach the equilibrium or null position. Then the desired speaker voltage is set in the function generator and the speaker is activated from rest, after which it is kept undisturbed. Only the field voltage is changed to measure the effects of phase. Furthermore, for each experiment the phases difference are uniformly sampled to minimize any uncertainity associated with a finite ϕ_s.

5.3 Results

The concept of SOEIF is demonstrated in Figure 5.3 for $a = 0.5$ μm particles transported by a steady flow with $\bar{u} = 2$ mm/s from left to right. The experimental conditions for each image are listed in the caption. These images are obtained from raw images by subtracting the median background, and subsequently projecting 200 of the resulting frames (corresponding to 4 seconds) onto a single image. The bright dots correspond to tracer particles and the bright bands to regions of high particle density.

The distribution of particles across the channel cross section is homogeneous when an oscillatory pressure driven flow is applied without an oscillatory electric field as shown in Figure 5.3 (a), or when an oscillatory electric field is applied without an oscillatory as seen from Figure 5.3 (b). A similar homogenous distribution is obtained when the flow and field frequencies are not synchronized as seen from Figure 5.3 (c) and (d). When the flow and field are synchronized however, depending on the phase difference, the particles are highly localized into focusing regions. For $\Phi = 0°$, a single focusing band at the centerline of the channel is observed as displayed in 5.3 (e). Conversely for $\Phi = 180°$, there are two focusing positions that are symmetric about the centerline as seen from Figure 5.3 (f).

As described in Chapter 4, histograms of particle density versus span-wise channel positions are shown beside the corresponding minimum projection image in Figure 5.3. There is a single sharp peak at the center of Figure 5.3 (e) corresponding to particle focusing at the center. The percentage of total particles in the red shaded region, that is, within $\pm l/10$

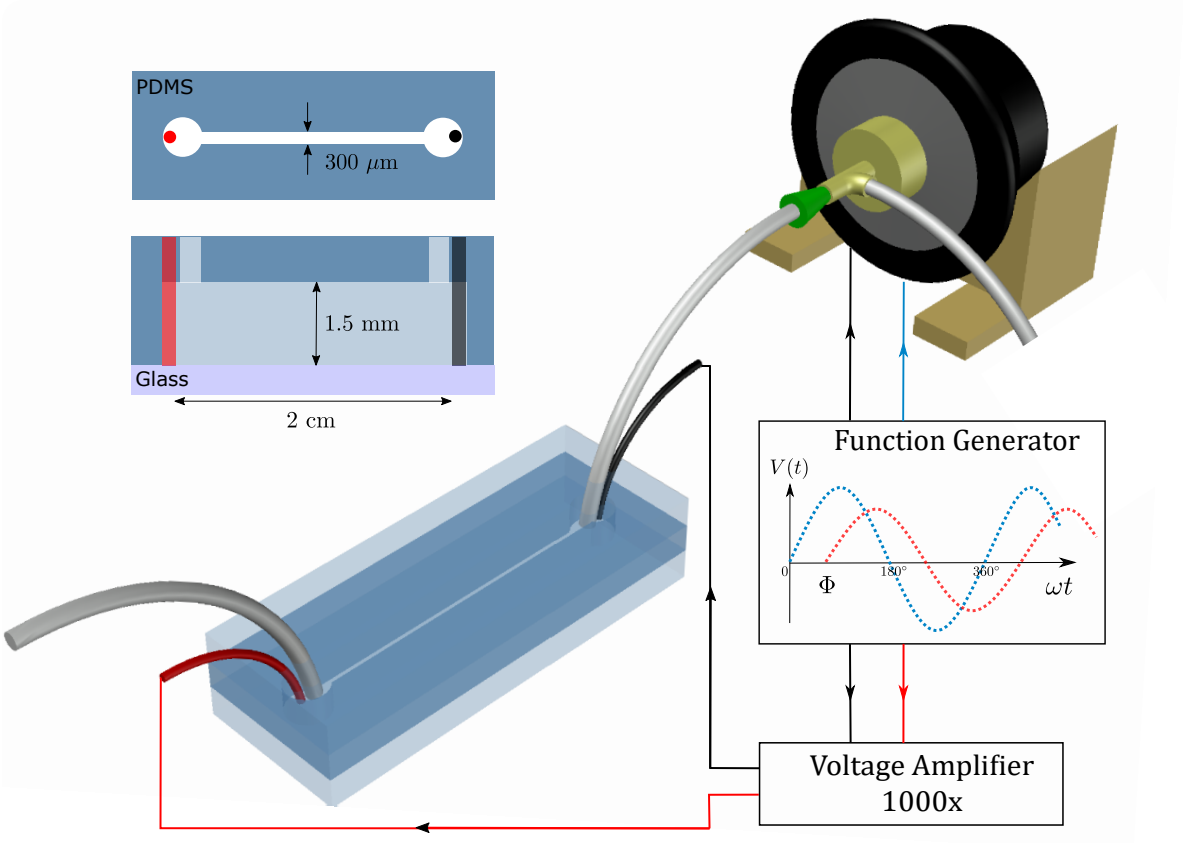

Figure 5.2: Experimental setup and microchannel. The PDMS microchannel (top left) has length $L = 2$ cm, height $h = 1.5$ mm and width $l = 300$ μm. A polyethylene tube and a stainless steel electrode is inserted at both the inlet and outlet. The outlet tube is interfaced to a speaker via an adapter elbow (yellow) affixed to the speaker cone. A pipette tip (green) is used as a wedge seal. The electrode terminals are connected to a high voltage adapter with a 1000× gain. The amplifier and the speaker are activated by a function generator that produces synchronized sinusoidal voltages with a controlled phase difference Φ.

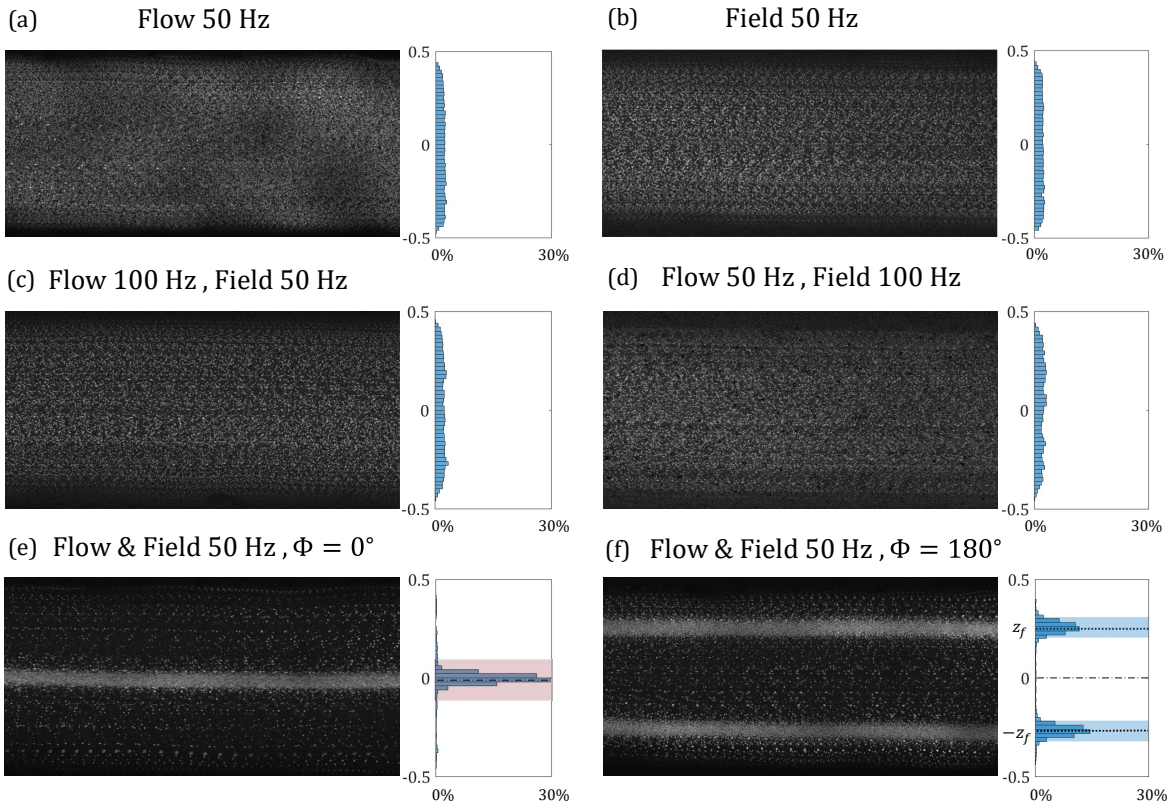

Figure 5.3: Images of particle minimum projections (background subtracted for contrast) near the channel outlet for $a = 0.5$ μm, $\bar{u} = 2$ mm/s, $L_R = 2$ cm for different frequency and phase conditions. (a) Oscillatory flow ON at 50 Hz, electric field OFF: $U = 73 \pm 5$ mm/s, $E = 0$ kV/m, $s_E\omega = 0$ mm/s. (b) Oscillatory flow OFF, electric field ON at 50 Hz: $U = 0$ mm/s, $E = 50$ kV/m, $s_E\omega = 1.1 \pm 0.2$ mm/s. (c) Oscillatory flow ON at frequency 100 Hz, electric field ON at frequency 50 Hz: $U = 77 \pm 8$ mm/s, $E = 50$ kV/m, $s_E\omega = 1.1 \pm 0.2$ mm/s. (d) Oscillatory flow ON at frequency 50 Hz, electric field ON at frequency 100 Hz: $U = 73 \pm 5$ mm/s, $E = 50$ kV/m, $s_E\omega = 0.9 \pm 0.2$ mm/s. (e) Oscillatory flow ON at frequency 50 Hz, electric field ON at frequency 50 Hz: $U = 73 \pm 5$ mm/s, $E = 50$ kV/m, $s_E\omega = 1.1 \pm 0.2$ mm/s with $\Phi = 0°$. (f) Oscillatory flow ON at frequency 50 Hz, electric field ON at frequency 50 Hz: $U = 73 \pm 5$ mm/s, $E = 50$ kV/m, $s_E\omega = 1.1 \pm 0.2$ mm/s with $\Phi = 180°$.

of the center is referred to as $F_{20\%}$ and quantifies the focusing efficiency. Likewise, there are two peaks in the histogram shown in Figure 5.3 that are symmetric about the center. The focusing position z_f is defined by the distance of either peak position from the channel center. For two focusing positions symmetric about the center, the focusing efficiency, F_{20}, quantifies the total fraction of particles located within $\pm l/20$ of either peak. Since this measurement is sensitive to the position of the centerline and the width of the channel, particle tracking was used to extract the steady flow profile and then fit to a parabolic curve. The fitting constants determined the precise centerline and local channel width.

5.3.1 Focusing position and efficiency

The evolution of particle pathlines with phase is shown in Figure 5.4 (a). At $\Phi = 0°$ the particles focus into a single band at the center of the channel. The single band focusing persists as Φ is increased from $\Phi = 0°$ through $\Phi = 40°$ with the same approximate band thickness. For $\Phi = 60° - 80°$, the apparent thickness of the focusing band increases. This is because of the incipient formation of two focusing bands, reflected by the particle density histogram having two closely spaced peaks that are not fully distinct and have overlapping regions. For $\Phi = 100°$ through $\Phi = 240°$ there are two distinct, well separated focusing bands, with no observable focusing at the channel center. At $\Phi = 260°$, there is a resurgence of an observable but diffuse focusing band at the center, which coexists with the two focusing positions close to the channel walls. As Φ increases further to $\Phi = 300°$, the focusing band at the center becomes narrower and more well defined, while the focusing band near the walls becomes less defined in comparison. Beyond $\Phi = 320°$, the focusing bands near the walls become unresolvable while the focusing band at the center continues to become narrower and more distinct, returning to the case of $\Phi = 0°$.

The evolution of focusing position (z_f) is plotted against phase in Figure 5.4 (b). The data markers are color coded according to whether there is stable focusing at the center (red, filled) or not (red, open), whether the focusing positions overlap with the center (purple), or

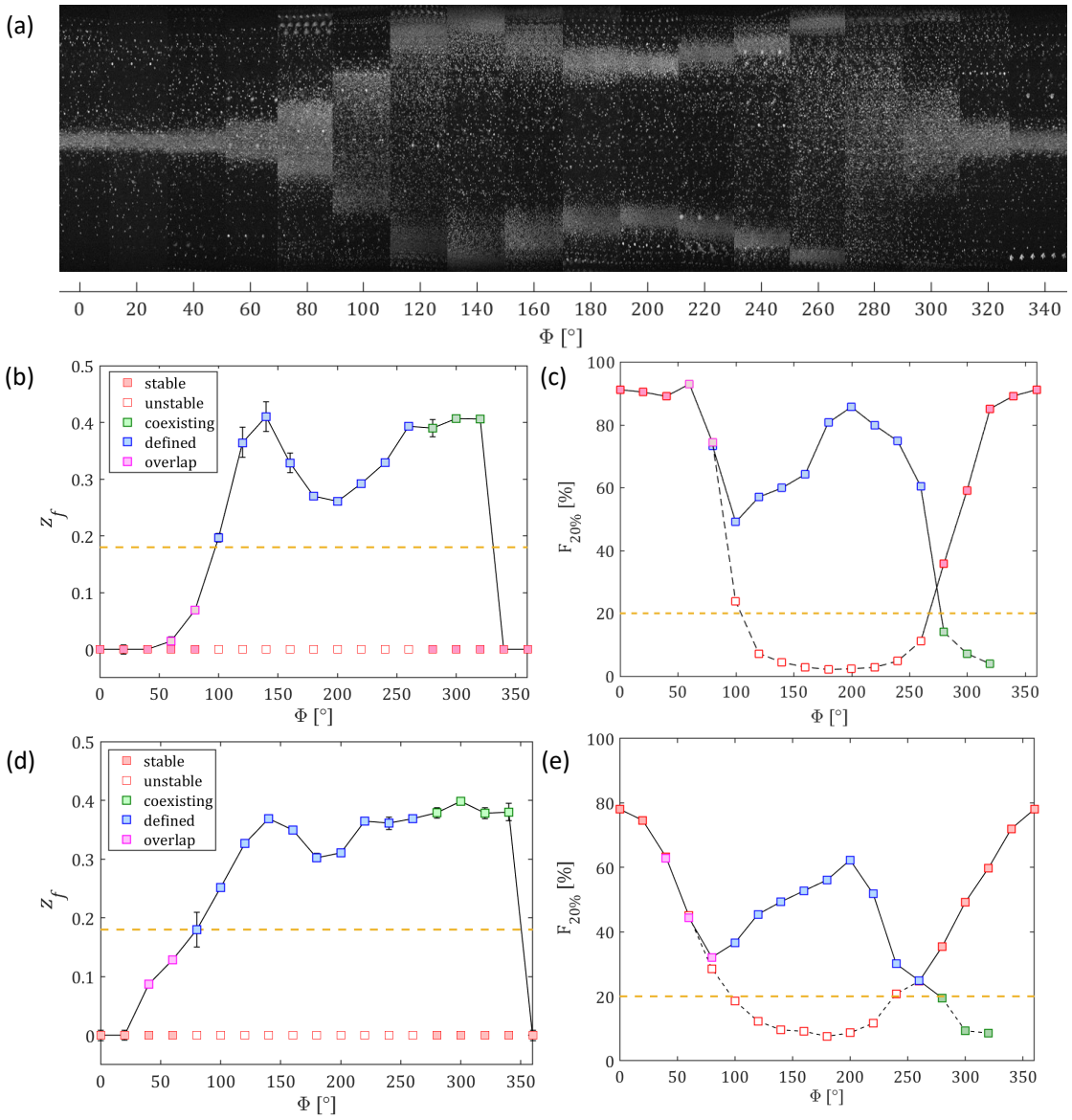

Figure 5.4: (a) Channel focusing bands as a function of Φ for $E = 50$ kV/m. (b) Focusing position as a function of Φ for the case shown in (a). The yellow dashed reference line shows focusing position for purely inertial focusing. (c) Focusing efficiency quantified by $F_{20\%}$ as a function of Φ for case shown in (a). The $F_{20\%}$ refers to the percentage of total particles within $\pm\, l/10$ of the focusing position. The yellow dashed reference line shows the efficiency for a homogeneous particle distribution. (d) Focusing position and (e) Focusing efficiency as a function of Φ for $E = 25$ kV/m. Different regimes encountered: stable focusing band at the center (red), eccentric focusing band with center overlap (magenta), defined eccentric focusing bands (blue), focusing band that coexists with stable focusing at center (green). Parameters: $a = 0.5$ μm, $\bar{u} = 2$ mm/s, $f = 50$ Hz, $l = 300$ μm, $s = 234$ μm, $s_E = 3$ μm at $E = 50$ kV/m, $L_R = 2$ cm.

distinct (blue), or coexist (green) with the center. Here $z_f = 0$ corresponds to the channel center, and $z_f = 0.5$ corresponds to the channel wall.

Initially, $0 \leq \Phi \leq 40°$ implies $z_f \approx 0$ meaning stable focusing only at the center (red, filled). For $60° \leq \Phi \leq 80°$, $z_f \leq 0.1$ for which the focusing bands overlap (purple) and are therefore not well defined. For $100° \leq \Phi \leq 260°$ the focusing position is well defined (blue) and first increases up to $z_f = 0.4$ at $\Phi = 140°$, and then subsequently decreases to $z_f \approx 0.3$ at $\Phi = 200°$, increasing once again to $z_f \approx 0.4$ at $\Phi = 260°$. The eccentric focusing position does not change much from $z_f \approx 0.4$ for $280° \leq \Phi \leq 320°$ but becomes less distinct, coexisting (green) with an increasingly well defined stable focusing position at the channel center. The center focusing band completely disappears for $340° \leq \Phi \leq 360°$ and the system reverts to stable focusing at the center.

The analogous $F_{20\%}$ measurements are also plotted against phase in Figure 5.4 (c). The yellow dashed line corresponds to $F_{20\%} = 20\%$, which represents the case of homogeneous particle distribution that is observed when only a flow, only a field or an asynchronized flow and field are used. For $0° \leq \Phi \leq 40°$, 90% of the particles are focused solely at the channel center. At $60° \leq \Phi \leq 80°$, both the focusing bands around the center and the two incipient focusing positions overlap. As a result, the focusing efficiency at the center, and around the histogram peaks are quite similar, and the data markers nearly overlap. For $100° \leq \Phi \leq 240°$, the focusing efficiency within the two distinct focused bands increases from 50% at $\Phi = 100°$ to a maxima of 85% at $\Phi = 200°$ and proceeds to decrease to 70% at $\Phi = 240°$. For this range, the center is no longer a discernible focusing position. Nevertheless, the focusing efficiency at the center is still shown and takes values less than 20% implying a deficiency or absence of particles. For $260° \leq \Phi \leq 360°$, the center becomes the principal focusing position once again, and the efficiency of the center improves from 35% up to 90%, as expected. Meanwhile, the focusing efficiency of the near wall focusing position drops rapidly from 60% at $\Phi = 260°$ to $\approx 0\%$ at $\Phi = 320°$.

Figure 5.4 (d) an (e) show the corresponding focusing position and focusing efficiency for

an electric field of lower oscillatory amplitude. The evolution of both the focusing position and the focusing efficiency with Φ is qualitatively similar to those seen in Figure 5.4 (b) and (c). Starting with stable focusing at the center ($z_f \approx 0$) for $\Phi = 0°, 20°$, the focusing position moves towards $z_f \approx 0.37$ at $\Phi = 140°$ comparatively steadily about which it fluctuates until $\Phi = 240°$. Interestingly, the decrease from $\Phi = 140°$ to $\Phi = 200°$ is much less pronounced in this case. As expected for an electro-inertial phenomenon, a weaker field amplitude results in less focusing efficiency in both the center focusing band and eccentric focusing bands, all other parameters are kept constant. The center band focusing efficiency is maximum at $\Phi = 0°$ and takes a value of $F_{20\%} \approx 80\%$, while the maximum eccentric band focusing is $F_{20\%} \approx 60\%$ at $\Phi = 20°$.

5.3.2 Particle migration velocity

The particle migration velocity, in contrast to the focusing efficiency, is a more direct measurement of the underlying focusing process and does not depend on the residence length. It provides an opportunity to isolate and characterize the mechanism of particle migration. Furthermore, measurement of the particle migration velocity benefits greatly from oscillatory flows due to the much longer ($> 100\times$) path distances that can be observed without loss in measurement resolution. To obtain the migration velocity measurements, particles are tracked 1 mm away from the inlet of the channel. This yields a spatially homogeneous sampling of particles and minimizes difficulties in tracking that can arise due to dense particle localization.

Figure 5.5 (a) shows a scatter plot of particle migration velocity measurements for the parameters described in the caption. Each data point (pink) corresponds to the migratory displacement of a particle at the end of one oscillatory period (1 frame at 50 fps for 50 Hz).

The migration velocity measurements in a sampling window (see Section 5.5) of streamwise length 1100 μm, spanwise length 18 μm and centered about $z/l = 0.25$ are plotted as a histogram in Figure 5.5 (b). The migration velocities follow a unimodal distribution with a

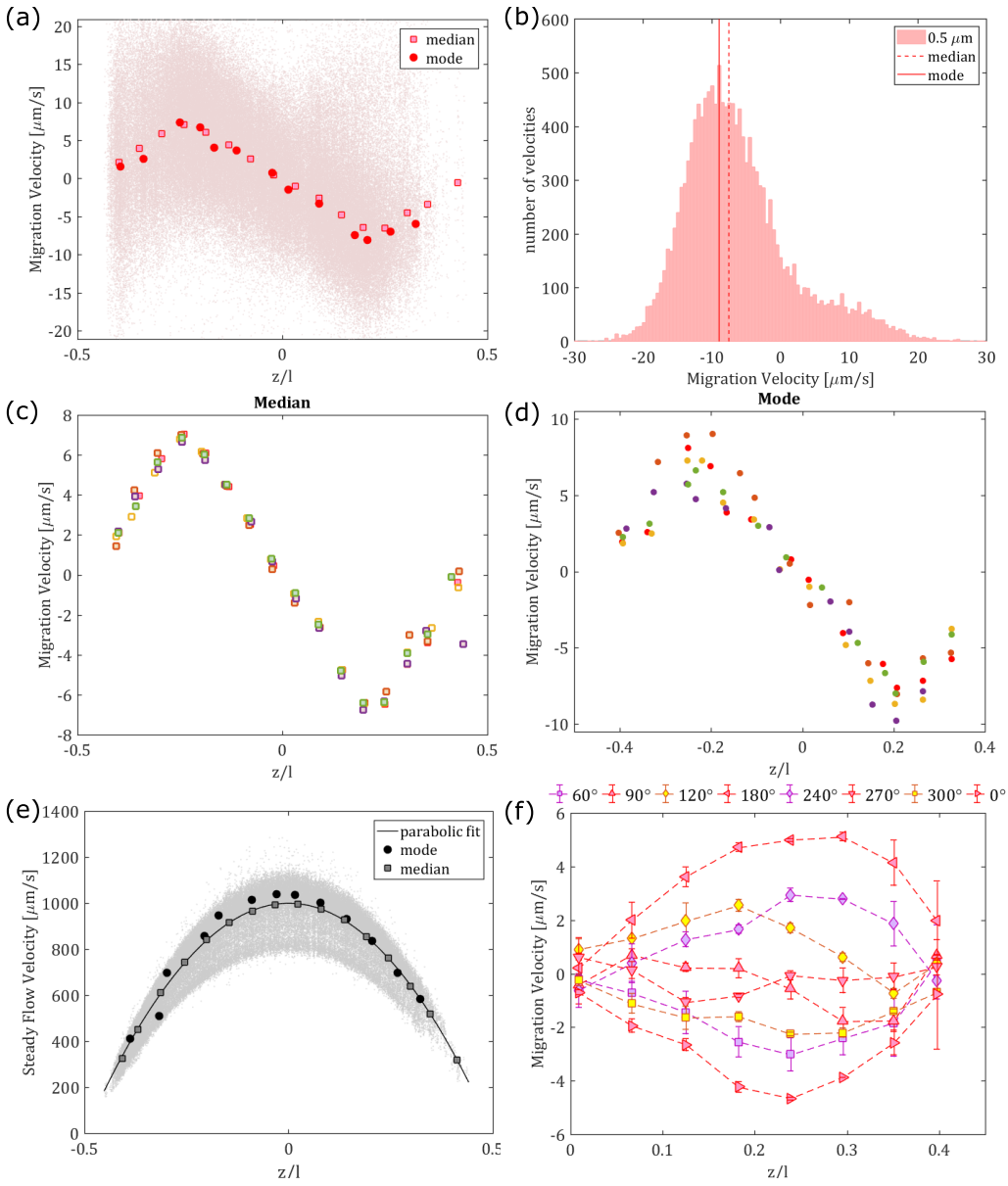

Figure 5.5: (a) Scatter plot of migration velocity at different span-wise positions. Median and modal filtered migration velocities. Reliable data range is from $-0.4 \leq z/l \leq 0.4$ (b) Histogram of migration velocities for particles in the spanwise position range $-0.28 \leq z/l \leq -0.22$. Median and modal migration velocities plotted in (a) are identified on the distribution. (c) Median and (d) and modal filtered migration velocity profiles, respectively, at $\Phi = 0°$ for multiple realizations ($N = 5$) under identical conditions illustrates higher repeatability of median filtering. (e) Scatter plot of raw steady transport velocity. Median and mode filtered transport velocity profile compared against a parabolic fit to the raw data. Parameters (a) - (e): $a = 0.5$ μm, $\bar{u} = 1.0$ mm/s, $f = 50$ Hz, $E = 50$ kV/m, $l = 300$ μm, $s = 60.5$ μm, $s_E = 3.5$ μm, $\Phi = 0°$. (f) Comparison of median filtered migration velocity profiles for different values of Φ. The errorbars are obtained by taking the deviation between two separate realizations. Parameters (f): $a = 0.5$ μm, $\bar{u} = 1.0$ mm/s, $f = 50$ Hz, $E = 50$ kV/m, $l = 300$ μm, $s = 32$ μm, $s_E = 7.1$ μm.

distinct peak. The median (dashed) and mode (dash-dot) of the distribution are marked on the histogram with the median velocity having a $\approx 10\%$ lesser magnitude than the modal velocity.

The median and mode of the measured velocities for each segment (width $l/16$) of the channel width are plotted against the corresponding position to obtain the effective migration velocity profile in Figure 5.5 (a). For $|z/l| > 0.4$, the effective velocities are not reliable due to a lack of sufficient particle density near the walls. As observed, there is a considerable spread in the data points around the median/modal values and the origin of this relatively large scatter of tracked migration velocities is investigated in Section 5.5. Similar spread in the velocity measurements is also seen in experiments shown in [Rossi et al., 2022].

Figure 5.5 (c) and 5.5 (d) show the median migration velocity measurements for multiple realizations ($N = 5$) of the same experiment. Each realization is marked with a different color. Evidently, the median migration velocity yields much more repeatable results and is therefore adopted hereafter. It is worth emphasizing that these migration velocities are a few microns per second, 100 times less than the transport velocity, and 1000 times less than the pressure driven velocity. Such measurements of this migration velocity are made possible only by using oscillatory flows, which can greatly extend the observational range without compromising the measurement resolution.

Figure 5.5 (e) shows the corresponding measurement of the transport velocity. A parabola is fit to the raw data and the precise channel center position and widths are extracted from it. Here too, it can be seen that the median velocity coincides with the fit, and thus, performs better than the corresponding modal velocity.

Figure 5.5 (f) shows the median migration velocities at different values of the phase difference Φ, ranging from $\Phi = 0^\circ$ to $\Phi = 360^\circ$. The errorbars are quantified by taking the deviation between migration velocity profiles obtained for two different realizations of the same experiment. As expected from observations in Figure 5.5 (a), the errorbars grow considerably large as z/l approaches 0.4.

For $\Phi = 0°$ the migration is completely towards the center at all positions indicated by its negative value for the entire measurable range. For $\Phi = 180°$ the migration is completely towards the stable position between $z/l = 0.35 - 0.4$. For $\Phi = 90°$ the migration is considerably weaker but towards a stable focusing position between $z/l = 0.2 - 0.25$ in agreement with Figure 5.4 (b). Likewise, $\Phi = 270°$ gives a migration velocity profile that indicates two focus positions: $z/l = 0$ and $z/l = 0.35 - 0.4$, also in agreement with Figure 5.4 (b). Overall, the migration velocity appears to follow an approximately $\cos\Phi$ dependence.

Next, the effect of electric field and oscillatory flow amplitude on the scaling of migration velocity are evaluated for $a = 0.5$ μm particles. In Figure 5.6 (a), the peak migration velocity is plotted against a varying electric field amplitude with the oscillatory flow amplitude and other experimental parameters kept constant. The peak value is taken to be the mean of three largest migration speeds (the local maxima and one point on either side) for $z/l < 0$ and $z/l > 0$. The errorbar corresponds to the difference between the peak values for $z/l > 0$ and $z/l < 0$. The maximum migration velocity scales linearly with electric field amplitude. Similarly, in Figure 5.6 (b), the peak migration velocity is plotted against the corresponding amplitude of the oscillatory flow with the electric field amplitude and other experimental parameters kept constant. The peak migration velocity also scales linearly with oscillatory flow amplitude.

Finally, particle migration velocity measurements for particles with radii $a = 1.7$ and 2.6 μm are presented. To control for measurement errors of oscillatory flow amplitude and electro-osmotic flow amplitude, these experiments were performed simultaneously with the previously shown measurements for $a = 0.5$ μm particles. That is, a solution with volume fraction 0.001% of 0.5 μm particles, 0.003% of 1.7 μm particles, and 0.01% of 2.6 μm particles was prepared and used. The corresponding migration velocities for $\Phi = 0°$ and $\Phi = 180°$ are shown in Figure 5.6 (c) for all three particle sizes. The plot data suggests that particle migration velocity is larger for smaller particles and decreases with particle size provided all other factors are kept identical. The migration velocities for other phases (not shown) also

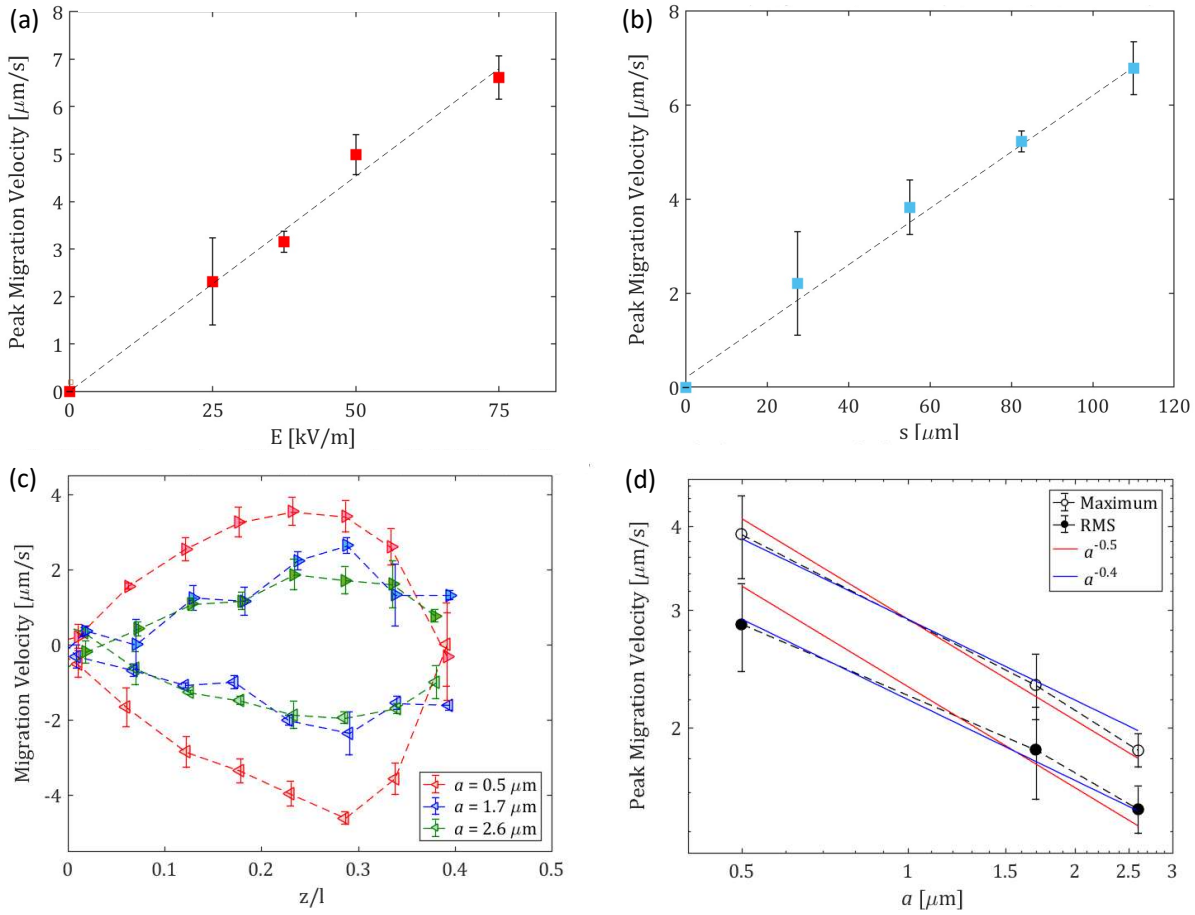

Figure 5.6: (a) Peak migration velocity scaling with electric field for $a = 0.5$ μm and $s = 60.5$ μm. At $E = 50$ kV/m, $s_E = 3.5$ μm. (b) Peak migration velocity scaling with oscillatory amplitude for $a = 0.5$ μm, $E = 50$ kV/m, $s_E = 3.4$ μm. (c) Migration velocity profiles of particles with $a = 0.5,\ 1.7,\ 2.6$ μm obtained simultaneously. Results for $\Phi = 0°$ and $\Phi = 180°$, $E = 50$ kV/m, $s = 32$ μm, $s_E = 7.1$ μm. (d) Peak migration velocity versus radius in log-log scale. Obtained either from averaging the peak velocity of phases $\Phi = 0°, 180°$, or by taking the rms average of all phases (sampled every 30°). Results for $E = 50$ kV/m, $s = 32$ μm, $s_E = 7.1$ μm. Red and blue dashed lines are power law curves $a^{-0.5}$ and $a^{-0.4}$, respectively. Other parameters: $\bar{u} = 1$ mm/s, $f = 50$ Hz, $l = 300$ μm.

corroborates this result.

As described previously, the peak migration speed, obtained by averaging the three largest migration speeds was obtained for the three different radii $a = 0.5, 1.7, 2.6$ μm ($\zeta_p = -22, -39, -53$ mV) and averaged for both $\Phi = 0°$ and $\Phi = 180°$ to obtain the maximum migration velocity. The errorbar is their corresponding difference. The maximum migration velocity is plotted in Figure 5.6 (d) against the particle radius in a log-log plot. To account for the variation with Φ and the startup uncertainty ϕ_s, the Root-Mean-Squared (RMS) peak velocity for a uniform sampling of Φ in steps of 30° was obtained, and is also plotted against particle radius in the same plot. The scaling exponent for the maximum and the phase-RMS migration velocities appear to follow a particle radius scaling of $\approx a^{-\xi}$ where $\xi = 0.4 - 0.5$ in this range of particle radii.

5.4 Discussion

Combining the above results, the following scaling law for the primary mechanism of particle migration is inferred in the channel bulk, that is for $l/2 - |z| \gg a$ is inferred:

$$W_m \sim EU \cos(\Phi + \phi_s) a^{-\xi}.$$

Based on the experimental evidence, the scaling of W_m with U and E are confirmed. The scaling with $\cos\Phi$ also emerges naturally from having $W_m \propto UE$. There is nevertheless, some indication of a sub-dominant secondary mechanism that causes the evolution of z_f and $F_{20\%}$ with Φ shown in Figure 5.4 to be asymmetric about $\Phi = 180°$. This fact reflected in the particle migration profiles for $\Phi = 90°$ and $\Phi = 270°$ shown in Figure 5.4 (f), which are weak but not uniformly zero.

The scaling of W_m with a is not conclusive, however it suggests that W_m decreases with particle radius a. If the effect of varying particle zeta potential is neglected, one

obtains $W_m \propto a^{-\xi}$ with $\xi \approx -0.5$. If the particle zeta potential is considered, one obtains $W_m \propto (\zeta_p/a)^{-\xi}$ with $\xi \approx 1$. Both possibilities contradict our expectation that the migration velocity is proportional to a^2 as suggested by recent theories [Khair and Kabarowski, 2020, Choudhary et al., 2019]. Further experiments with controlled zeta potentials and particle radii will need to be performed to identify the mechanism more precisely. In the subsequent paragraphs, these findings are compared to the experiments of other groups that use steady flows and DC electric fields and the comparison is summarized in Table 5.1. The implications of our results for theories are also discussed.

Particle migration in a combined electric field and pressure driven flow were first reported in [Kim and Yoo, 2009]. Polystyrene particles of diameter 5 μm and electrophoretic mobility -0.025 mm^2/V $\cdot$ s, were suspended in a neutrally buoyant glycerol-water solution. A steady flow with centerline velocity 1.77 mm/s and an electric field of 12.8 kV/m aligned parallel to flow were used to focus particles at the center of a Tygon tube of diameter 85 μm. It was found that focusing saturated at 90% at the center after a transient period of 45 seconds, when a position 5 cm from the inlet was observed. This indicates a migration velocity of $42/45 \approx 1$ μm/s. In a subsequent work [Kim and Yoo, 2015] performed an experiment under nearly identical conditions in a square PDMS channel of dimensions 82×90 μm and length 4.5 cm, the transient period once again found to be around 45 seconds and corresponding to a migration velocity of $44/45 \approx 1$ μm/s.

An independent body of work [Cevheri and Yoda, 2014c] examined the distribution of polystyrene colloidal particles with radius 245 nm near the bottom (glass) surface of a 350×30 μm microchannel using evanescent wave particle tracking. When subject to a combination of pressure driven flow (wall shear rates 1600 s^{-1}) and an anti-parallel electric field (-9.5 kV/m) [Cevheri and Yoda, 2014b], the particles move towards the bottom and eventually self assemble into periodically spaced stripes of high particle densities that are oriented along the direction of flow. When the field (-0.95 kV/m) is parallel to the flow (shear rates 1600 s^{-1}) [Cevheri and Yoda, 2014a], particles near the bottom surface experience a

lift force that is significantly larger (20 fN), and qualitatively different than the lift forces caused only by flow, and only by field. That is, the combined lift is much greater than the sum of parts, indicating a nonlinear interaction between the effects of flow and field. The measured force has a linear scaling with the field, as opposed to the quadratic scaling found without a driven flow. The lift force also scales sub-linearly with strain rate, with a power law exponent of $0.4 - 0.5$, in contrast with the linear scaling with strain measured in the absence of an electric field. Although illuminating, these near-wall lift measurements are not directly comparable to the migration velocity measurement presented in Figures 5.5 and 5.6 since the former measurements are only valid within 500 nm of the walls while latter measurements are not reliable within 30 μm of either wall.

Subsequent works [Yee and Yoda, 2018, Yee and Yoda, 2021] report the time taken for the particles to accumulate at the bottom surface before the onset of banding, under similar experimental conditions as those described above. The accumulation time T_0, is a measure of the average migration velocity in the bulk of the channel and can therefore be directly compared with the results presented here. The migration velocity can be estimated to be $W_m \approx 34/T_0$ μm/s, correct to an order unity prefactor. Based on the experiments shown in [Yee and Yoda, 2018], the migration velocity scales as: $W_m \propto T_0^{-1} \propto \dot{\gamma}E$, in agreement with our results. Furthermore W_m is shown to increase with particle volume fraction but decreases with increasing particle radius (zeta potential kept fixed). The latter counter-intuitive decrease with particle size is also in agreement with our experiments. Likewise, the migration velocity for particle radius 355 nm, a field of -3.1 kV/m, and strain rate 1070 s^{-1} is measured to be $W_m \approx 2$ μm/s, concordant with results in Figure 5.5 for $E = 50$ kV/m and $u/l = 33.5$ s^{-1} even though the channel is ten times larger in width.

The linear scaling of the electro-inertial lift force with electric field and strain rate is also reported by [Lochab and Prakash, 2021] for particle radius 240 nm. For the center focusing case (flow and field aligned), the migration velocity is estimated by dividing the channel width by the time taken for the 3D particle distributions obtained via confocal microscopy

to stabilize. For a field of +10 kV/m and a shear rate 540 s^{-1}, the particle experiences a force of 30 fN, which corresponds to a migration velocity of 4.5 μm/s, in agreement with data presented here. The extent of particle focusing, and by extension the migration velocity, is found to decrease strongly with viscosity, which is evidenced by the fact that it goes from well focused to completely unfocused when the viscosity is increased by a factor of 2. Interestingly, for 5 μm particles in viscoelastic polymeric solutions (1000 ppm Poly-Ethylene-Oxide), experiments [Li and Xuan, 2018] revealed that the direction of migration was exactly reversed. That is, when the flow and field are parallel, particle migrated towards the walls and when the field and flow were anti-parallel, particles migrated towards the center.

The most promising theory to explain these observations was derived independently by [Choudhary et al., 2019] and [Khair and Kabarowski, 2020]. For a pure shear flow of a Newtonian liquid with shear rate u/l, the migration velocity is given by:

$$W_m = -\frac{0.29\varepsilon\zeta_p a^2 EU}{\mu^2 l}.$$

In this case, the lift on the particle arises from a nonlinear interaction between the electrophoretic disturbance velocity created by a charged particle in an electric field, with the undisturbed pressure driven flow. This theory captures many features of the measured electro-inertial migration such as the linear proportionality of both field and amplitude (or equivalently shear rate) and the inverse dependence on viscosity and predicts the direction of migration correctly. For relatively large particles $a > 5$ μm, this theory predicts migration velocities comparable in magnitude to experiments. For colloidal particles, for instance $a = 500$ nm, the migration velocities are ~ 10 nm/s, a hundred times smaller than the experimentally measured migration velocities of ~ 1 μm/s. Furthermore, this theory predicts a strong increase in migration velocity with particle radius, while experiments shown here and elsewhere [Yee and Yoda, 2018] suggest a negative scaling with particle radius.

The mechanism responsible for this weak negative scaling with particle remains elusive,

but it seems plausible that this is caused by a finite value of λ_D. This is suggested by another theory [Khair and Balu, 2019] which predicts a Magnus-like lift arising from a shear induced asymmetry in the ionic cloud surrounding the particle. The theory predicts a migration velocity:

$$W_m = -\mathcal{L}(a/\lambda_D)\frac{\varepsilon^2\zeta_p^3 a^2 EU}{12\pi D^2\mu^2 l} \approx -\frac{\varepsilon^2\zeta_p^3\lambda_D^5 EU}{12\pi D^2\mu^2 l a^3},$$

where the function $\mathcal{L}(a/\lambda_D) \propto (a/\lambda_D)^{-5}$ when $a \gg \lambda_D$ indicating the possibility of an apparent negative scaling with radius. Unfortunately, this theory also predicts migration velocities much lower than those obtained experimentally

Finally, there is also the possibility of long-range interactions and collective dynamics of particles. This is suggested by [Yee and Yoda, 2018] which reports that the accumulation time decreases as the volume fraction increases from 0.17% to 0.33%, all other parameters kept constant. In the accumulation time measurements, particles get highly localized near the bottom plane and subsequently self organize into bands. Inter-particle interactions are thus inevitable, confounding the relationship between the bulk migration velocity and the accumulation time. In this work however, the effects of particle interactions are significantly reduced by using a volume fractions less than 0.001% and measuring migration velocities near the inlet, where particle localization and consequent interactions are minimal. Nevertheless, comparable magnitudes of migration velocity are obtained and therefore collective dynamics and long-range interactions are unlikely.

Combining the above observations and insights, I hypothesize the following form for the migration velocity:

$$W_m = \mathcal{K}(a/\lambda_D)\frac{\rho U l_s^2}{l\mu}\frac{\zeta_p E\varepsilon}{\mu}\cos\phi,$$

where l_s is a length scale which arises from electrokinetics and depends only on material properties of the particle and fluid.

Future experiments will explore the role of frequency on the particle migration. Two important non dimensional groups can be independently examined with the current apparatus

Manuscript	a [μm]	U/l [s^{-1}]	E [KV/m]	U_m [μm/s]	lU_m/EU [μm^2/V]	Comments [μm]
Kim & Yoo (2009)	2.5	20.0	12.9	1.89	7.3	Tube 85 μm
Kim & Yoo (2015)	2.5	18.6	13.0	1.91	7.9	82×90 μm
Cevheri & Yoda (2014)	0.245	400	0.5	2.6	13	Near wall migration
Li & Xuan (2018)	5	55	30	6.9	4.18	50×100 μm
Yee & Yoda (2018)	0.25	440	1	1.76	4.0	34.6×340 μm
Lochab & Prakash (2021)	0.25	1000	2	2.5	1.25	34.6×340 μm
This work	0.5	36	50	4.5	5.0*	300×1500 μm

Table 5.1: Comparison of experimental parameters across studies. *− Multiplied by a factor of two to account for oscillatory flow.

in the $25 - 800$ Hz frequency range: the Womersley number $\alpha = l/\sqrt{\nu/\omega}$, which simultaneously determines the pressure driven and electro-osmotic flow profiles; and the dimensionless concentration polarization time, also known as volume diffusion time : $\vartheta = \omega a^2/2D$. The effect of α, can be surveyed by increasing the frequency from 50 Hz ($\alpha = 4$) to 800 Hz ($\alpha = 16$). The effect of ϑ, can be isolated by decreasing the channel width to 75 μm and increasing the frequency so that $\alpha \leq 5$ even at the highest frequencies, and performing experiments at frequencies ranging from $25 - 800$ Hz with particles of radius 1.7 μm.

5.5 Supplementary: Velocity Scattering

The mechanism of the noisy spread of measured migration (pink) and transport (black) velocities seen in Figure 5.5 (a) and (e) respectively is discussed in this section. For any narrow segment of the span-wise position, the migration velocities obey a unimodal distribution with a distinct peak as demonstrated in Figure 5.5 (b). Since the mean is known to not be a good measure of central tendency for noisy distributions, the median and mode were used to obtain the effective migration velocity profile. Upon comparison, the median was found to be have better repeatability across different identical trials and was adopted thereafter, yielding results in good agreement with previous literature for steady flow electro-inertial focusing (see Table 5.1).

In this section, the origin of the spread is investigated. The Brownian contribution to the velocity spread can be estimated using the well known linear relationship between the root-mean-squared displacement of the particle's center of mass (z_p) and the time elapsed (Δt):

$$\langle (z_p(\Delta t) - z_p(0))^2 \rangle = 2D_p \Delta t \implies U_B = \frac{\sqrt{\langle (z_p(\Delta_p t) - z_p(0))^2 \rangle}}{\Delta t} = \sqrt{\frac{2D_p}{\Delta t}},$$

where U_B is the characteristic Brownian scattering velocity, $D_p = \frac{k_B T}{6\pi\mu a}$ is the diffusion coefficient of the particle center of mass, and the angular brackets denote ensemble average. For $\Delta t = 20$ ms (50 fps imaging), $a = 0.5$ μm implies $U_B \approx 5$ μm/s and $a = 1.7$ μm implies $U_B = 2.9$ μm/s. While U_B is comparable to the measured velocity scattering, it is not large enough to be considered the sole cause.

To assess the effects of oscillatory electric field and oscillatory flow on the measured spread of tracked velocities, the distribution of both the migration and transport velocities are analyzed inside a sampling window of size $\Delta x \times \Delta y$ and centered about $z/l = -0.25$ and illustrated in Figure 5.7. By default, $\Delta x = 1100$ μm and $\Delta y = 18$ μm is chosen so that a well populated distribution of velocities with a distinct non-zero median can be analyzed without too much loss in position resolution. The position $z/l = -0.25$ is chosen because the migration speed is approximately maximum. To conveniently compare the distributions across different cases, we obtain the envelope of the histogram such as the one shown in Figure 5.5 (b) with the maxima normalized to unity. This is referred to as the normalized distribution curve and is shown for both the migration and transport velocities in Figure 5.7 (b) and (c) respectively.

The distributions of $a = 0.5$ μm particles in an oscillatory flow ($s = 91$ μm), with ($E = 50$ kV/m, red) and without ($E = 0$ kV/m, black) an oscillatory electric field are contrasted for multiple ($N = 3$) realizations in Figure 5.7 (b) and (c). The distribution curves for particles with $a = 1.7$ μm (blue) measured concurrently with the $a = 0.5$ μm

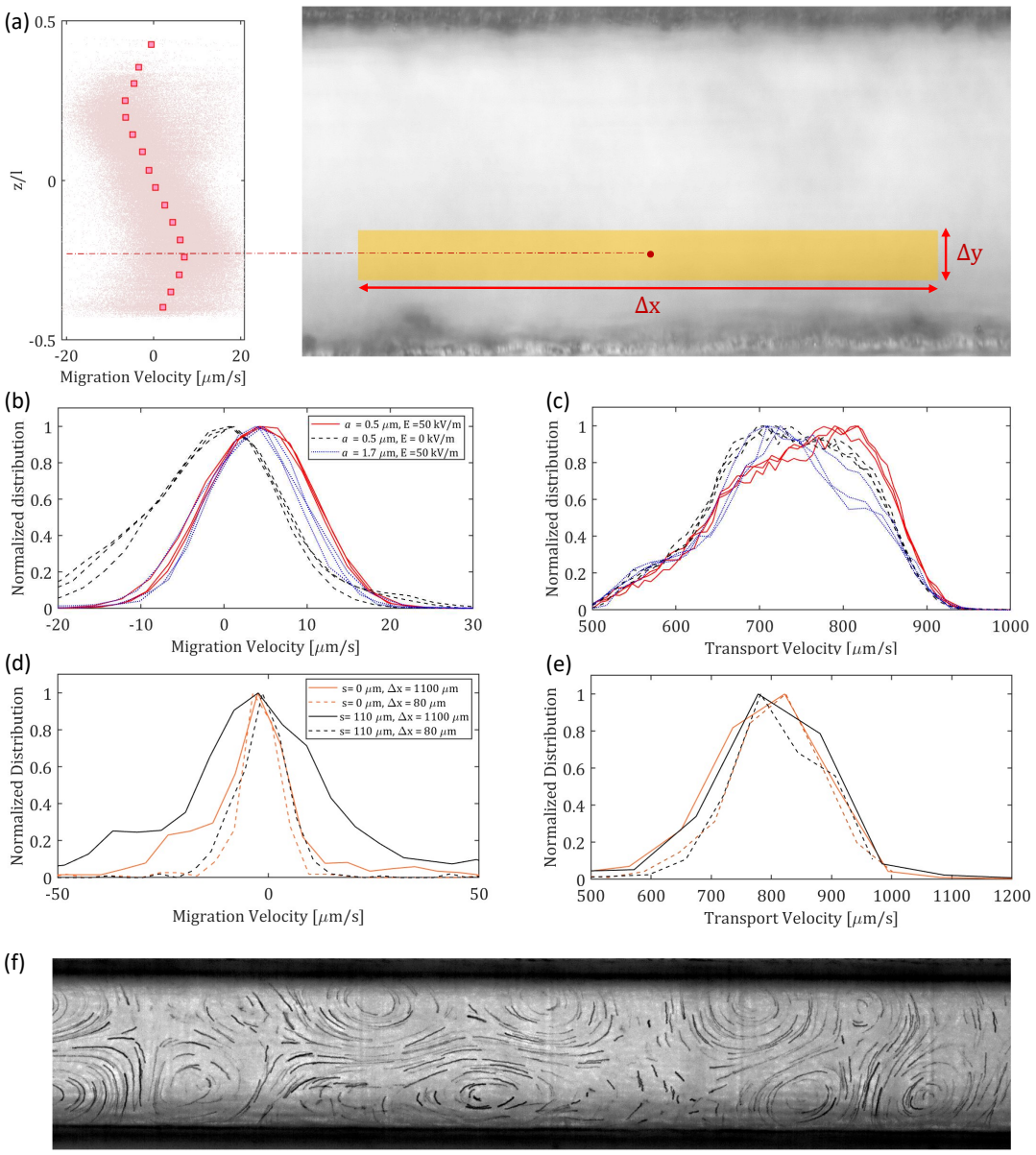

Figure 5.7: (a) Illustrates sampling window of size $\Delta x \times \Delta y$ centered about $z/l = -0.25$. By default $\Delta x = 1100$ μm and $\Delta y = 18$ μm. (b) and (c) Normalized distribution curves of migration and transport velocities, respectively. Compares the distributions of $a = 0.5$ μm particles in an oscillatory flow ($s = 91$ μm), with ($E = 50$ kV/m, red) and without ($E = 0$ kV/m, black) an electric field, along with $a = 1.7$ μm (blue) for the same conditions. Variation across multiple ($N = 3$) realizations is also displayed. (d) and (e) Compares migration and transport velocity distributions for $a = 0.5$ μm particles without an electric field ($E = 0$ kV/m), for cases with ($s = 110$ μm, black) and without ($s = 0$ μm, orange) an oscillatory flow. Also shows the comparison between the distribution obtained for a sampling window with a large ($\Delta x = 1100$ μm, continuous) and small ($\Delta x = 80$ μm, dashed). (f) Illustrates wall roughness generated streaming vortices in absence of a steady transport flow and producing scattering in migration velocity measurements.

(red) case for $E = 50$ kV/m are also plotted. Comparing multiple trials for a given case (color), it is seen that the distributions have relatively small error ($< 5\%$) and are robust characteristics for investigating the scatter. In order to compare the extent of scatter between two distributions, we define the peak width given by the full width of the distribution peak at half its maximum value (FWHM) as our metric.

For the migration velocity distributions in Figure 5.7 (b), the cases of $a = 0.5$ μm with and without an electric field have approximately equal peak widths and differ only by the position of the maxima. This implies that the peak width, and therefore the spread of velocities are largely unaffected by the presence or absence of an electric field. Additionally, for $a = 1.7$ μm, the peak width is measurably narrower than for $a = 0.5$ μm, plausibly due to the reduced contribution of Brownian motion for larger particles as discussed previously.

For the transport velocity, the scatter is significant but relatively much smaller compared to the median transport velocity. There is a measurable distortion of transport velocity distribution depending on the case, however the peak width is approximately the same in all cases.

Figure 5.7 (d) and (e) show the migration and transport velocity distributions respectively, for $a = 0.5$ μm particles in the absence of any electric field ($E = 0$ kV/m). Instead, these plots show the distributions for the case with ($s = 110$ μm, black) and without ($s = 0$ μm, orange) an oscillatory flow. A comparison for those cases at two different sampling lengths ($\Delta x = 80$ μm and $\Delta x = 1100$ μm) is also displayed. For $\Delta x = 1100$ μm, it is seen that the peak width for the case with an oscillatory flow (black, continuous) is approximately twice of that for the case without (orange, continuous). However, when $\Delta x = 80$ μm, the difference between the peak widths for the cases with (black, dashed) and without (orange, dashed) oscillatory flow are negligible. Interestingly, for the transport velocity, all four cases have virtually identical distributions with the peak width for the $\Delta x = 80$ μm cases, being only 10% less than the $\Delta x = 1100$ μm case.

Given the observations of Figure 5.7 (b) - (e), the spread of measured migration velocity

is best explained by a combination of particle scattering due to Brownian motion and channel streaming vortices. These channel streaming vortices are currently not well understood, and arise even in relatively straight channels, possibly due to the roughness of wall surfaces and the finite channel height or 3D nature of the channel manifold. These streaming vortices were measured to have maximum velocities in the $\mathcal{O}(10\ \mu\text{m/s})$ range for oscillatory amplitudes of $s = 10 - 100\ \mu\text{m}$ and channel width of 300 μm and are typically suppressed by a steady transport flow, but can be visualized in the absence of it as shown in Figure 5.7 (f). In the absence of a weak transport flow, these vortices tend to randomize particle positions and homogenize particle distributions that have been focused into bands. However, because these are streaming vortices and therefore obey mass conservation, over long distances, the randomizing or homogenizing effects of these vortices average out to zero. For this reason, when a steady transport flow is used, the effect of streaming on effective particle migration becomes negligible, therefore allowing particles to be focused into bands without being randomized. Instead, these vortices result in an increase in the scatter of the measured migration velocity, especially when long sampling windows are used. When short sampling windows are used the scattering is less, but the effective migration velocity is inaccurate due to the effect of the streaming vortices not averaging out to zero.

Chapter 6

Summary and Applications

6.1 Summary

In Chapter 2, an experimental technique to generate oscillatory flows was demonstrated. This method involved the direct interfacing of microfluidic tubing with a speaker diaphragm, which allowed independent control of oscillation frequency and amplitude. Frequencies ranging from $25 \leq f \leq 800$ Hz ($157 \leq \omega \leq 5026$ rad/s) and amplitudes ranging from $10 \leq s \leq 600$ µm ($U \leq 10$ cm/s) were realized for a 110 μm $\times$ 110 μm $\times$ 6 cm PDMS microchannel. Displacement amplitudes as large as 100 μm, and velocity amplitudes as large as 4 cm/s could be generated over the entire range frequencies. For sinusoidal signals, Fourier analysis yields low harmonic distortion (THD$<$ 10%) except for the highest frequencies at the highest volumes ($>$ 4.5 V input). The apparatus, imaging and particle tracking was validated across the frequency range through comparison of experiments with established theories for oscillatory flow near a flat surface and flow inside a square channel.

In Chapter 3, the steady streaming flow field was first characterized for a single cylinder, using its topological features across different dimensionless frequencies ($\delta_{AC}/a \equiv \alpha^{-1} = \sqrt{\nu/\omega}/a$) and cylinder aspect ratios (h/a). For shorter cylinders ($h/a = 0.7 - 2$), saddle points were not observed at all. Measurements of the eddy center distance (L_e/a) grew approximately linearly with α^{-1} in agreement with established theory, but only at high frequencies. For cylinders with $h/a = 3.75$, measurements of both the normalized eddy center distance (δ_{DC}/a), and the normalized saddle point distance (δ_{DC}/a) agreed well with both theoretical and DNS simulation results, growing approximately linearly for the entire

frequency frequency range. For a checkerboard lattice of high aspect ratio cylinders, five new flow topologies were obtained, each with a different number of vortex centers depending on both the curvature ratios of the two cylinders $\kappa_{max}/\kappa_{min}$ and $\delta_{AC}\kappa_{max}$. The number of vortices were found to increase with increasing frequency, and a corresponding number of saddle points also emerged to coincide conserve the topological charge of the flow. These topological features were found to match well with those obtained from simulations. The lattice system was demonstrated to filter inertial particles ($St > 0.1$). Filtration efficiencies $> 70\%$ were obtained when $\delta_{AC}\kappa_{max} < 0.14$ or equivalently when $\alpha > 7$ for the smaller radius. Likewise, the streaming flow topology for a bullet geometry was also in complete agreement with simulations. The unique streaming flow topologies around the bullet were used for continuous flow separation of inertial particles, with separation efficiencies $> 70\%$ obtained when $\delta_{AC}\kappa_{max} < 0.14$ or equivalently when $\alpha > 7$. The filtration efficiency for comparably sized human cheek cells was found to be only slightly lower. This implies that comparable filtration efficiency can be obtained even when soft and non spherical particles are used rather than rigid spherical particles.

In Chapter 4, inertial focusing was demonstrated in an oscillatory flow through a quasi-2D microchannel. The focusing efficiency measured at the outlet of the channel was found to reach steady state after a time equivalent to the residence time ($t_R = L/\bar{u}$) of particles inside the channel. The focusing efficiency was primarily determined by the particle Reynolds number $Re_p = Ua^2/l\nu$, and $> 90\%$ focusing was obtained even when $Re_p < 0.1$ for a straight channel of only 4 cm length. For low frequencies i.e $\alpha < 5$, the focusing position and the focusing efficiency were found to be constant and unchanged from those expected for a steady flow. For $\alpha > 5$, the focusing position was found to be move closer to the channel wall while the focusing efficiency was found to decrease. The dependence of the focusing position on α was in quantitative concordance with the predictions of asymptotic theory for the limit of infinitesimal ($a/l \ll 1$) particles. Precise measurements of the particle migration velocity were performed for low and high frequencies and were found to display good agreement with

the derived asymptotic theories, thereby validating the scaling law for the migration velocity as: $W_m \sim U(a/l)^3$.

In Chapter 5, SOEIF was demonstrated using an oscillatory flow and a synchronous oscillatory electric field inside a quasi-2D PDMS microchannel. Successful focusing of particles with radii almost 3 orders of magnitude smaller than the channel width ($a/l = 0.0016$) was performed, with $Re_p \ll 0.001$. By changing the phase difference between the electric field and flow (Φ), the focusing position of negatively charge polystyrene particles could be tuned between the center of the channel ($\Phi = 0$), to very near the walls ($\Phi = 180$). The migration velocity was found to scale linearly with the oscillatory amplitude ($W_m \propto s \propto U$), linearly with electro-osmotic flow amplitude ($W_m \propto s_E \propto E$) and with the cosine of the phase $W_m \propto \cos\Phi$. The phase averaged migration velocity was found to increase with decreasing particle radius for identical conditions, scaling weakly with particle radius. For the experimental range considered $W_m \propto a^{-\xi}$ where $\xi = 0.4 - 0.5$.

A succinct overview of the advances to micro-particle manipulation achieved through the work presented in this thesis is shown in Figure 6.1 in terms of the confinement ratio a/l. Compared to elementary filtration where the particle size is comparable to the width of the flow manifold, the techniques presented in Chapter 3 to Chapter 5 have progressively enabled the manipulation of particles that are $2-3$ orders of magnitude smaller by leveraging oscillatory flows.

6.2 Assessment and Applications

In this section I assess the applications of microfluidics and propose ways in which my unique contributions, and more generally oscillatory and nonlinear microfluidics can be effectively applied. To do this I categorize microfluidic applications into two broad categories: decentralized and centralized microfluidics, and make recommendations specific to each category.

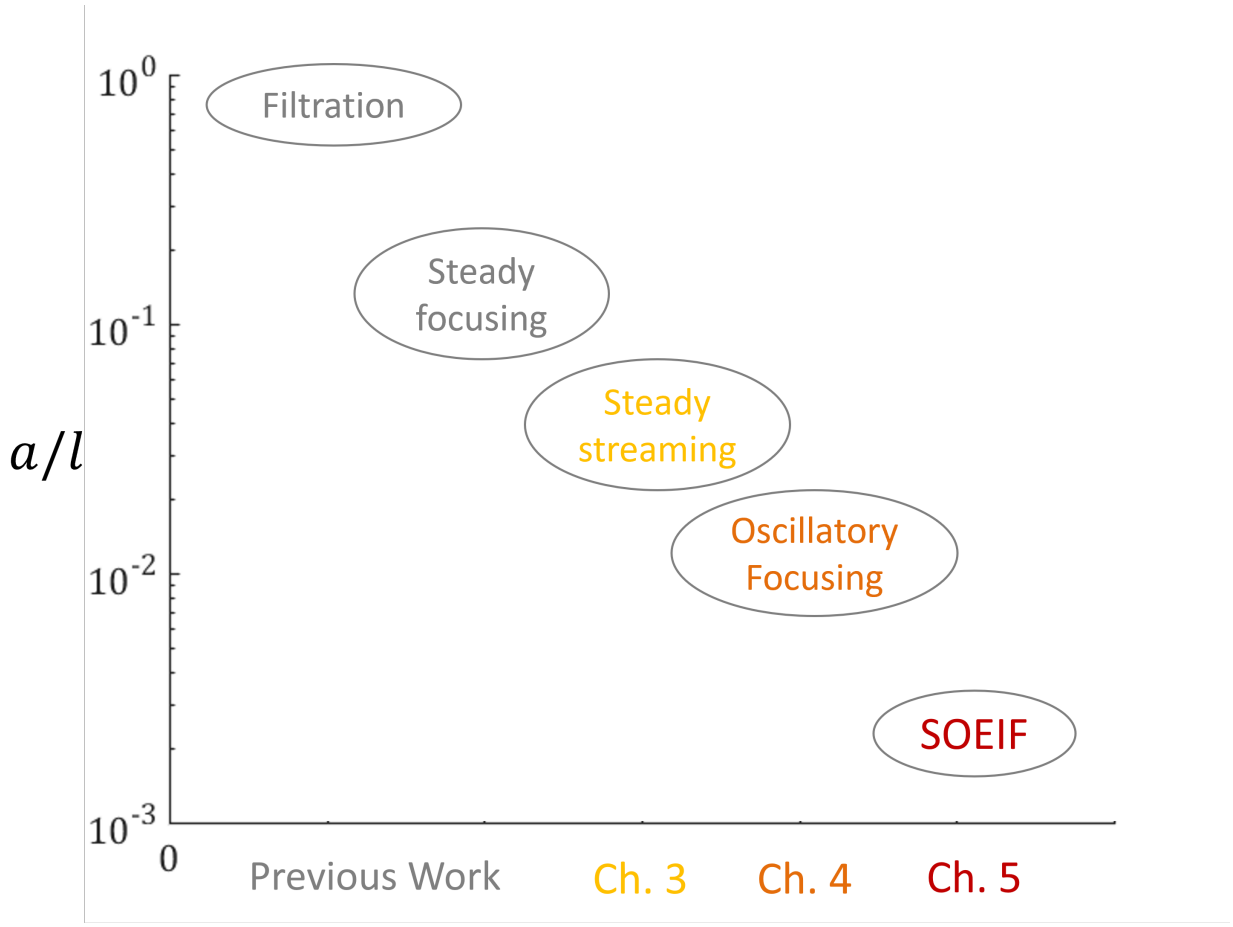

Figure 6.1: Summary of progress made in this thesis in terms of a/l. The techniques Compared to filtration, a 3 order of magnitude decrease in the blockage ratio has been demonstrated.

6.2.1 Decentralized Microfluidics

By decentralized microfluidics, I refer to the class of microfluidic applications that include point of care diagnostic devices [Yang et al., 2022], wearable microfluidics [Padash et al., 2020], chemical sensors for hazardous compounds [Plamen et al., 2005] and microfluidics for structural, process and environmental prognostics [Kung et al., 2019, Yew et al., 2019]. These devices are invariably for the purposes of chemical or biological analysis and are typically single functional, highly target specific, cheap, sturdy, and ideally require minimal expertise and peripheral equipment to use. Established traditions of decentralized microfluidics include paper microfluidics (μPADs) and centrifugal microfluidics (Lab on Disk) [Miyazaki et al., 2020]. For these applications, cheap and rapid fabrication methods such as soft lithography, injection molding, additive manufacturing (Fused deposition molding (FD), Sterelithography (SLA) and PolyJet(PJ)), wax paper printing and xurography are typically used. In the coming years, additive manufacturing are posed to be the dominant method of decentralized microfluidic devices with paper microfluidics in second place [Bhattacharjee et al., 2016, Nishat et al., 2021].

In this category of applications, the most preferred means of driving fluid is using gravitational head, capillary action or manual force since these are methods that do not require any electricity. However, if some systematic control and programability is required due to the complexity of the operation, speaker based oscillatory actuation is a viable method for pumping fluid [Jain and Lutz, 2017], controlling valves [Bachman et al., 2019], mixing and particle separation especially when compliant/soft features can be incorporated into the device, since basic phones (phones without internet), radios and earphones/speakers are available even in considerably under-resourced regions. For contrast, Lab on Disk devices require a disk player that is steadily declining in availability and either a low skilled operator or an internet connection to function.

While Electro-osmotic pumping for low conductivity samples or magnetohydrodynamic

pumping for high conductivity samples can also be used, these risk damaging the sample and in the case of electro-osmotic pumping require voltages larger than 5V. In this case, SOEIF becomes a technique that can be applied to minimize the exposure to strong electric fields and Maxwell stresses typically experienced with techniques such as dielectrophoretic particle manipulation. Furthermore, SOEIF can be highly effective in manipulating particles three orders of magnitude smaller than the width of the channel as demonstrated in Chapter 5 allowing for microparticle manipulation without the need for microchannels.

6.2.2 Centralized Microfluidics

By centralized microfluidics, I refer to sophisticated bespoke microfluidic systems that employ numerous sensors and actuators that operate in concert, typically used in biotech industries or research institutes. Such microfluidic platforms are constructed by combining modules that perform specific operations including but not limited to: droplet production and encapsulation, droplet fusion and fission, particle manipulation, mixing, exposure to light, acoustic/electric impedance measurement, sorting, heating/cooling, prolonged incubation and observation. These microfluidic devices are often integrated with computers or microcontrollers for real time image and signal analysis, control and optimization. They include optical components for analyzing florescent markers and even X-ray, neutron or light scattering setups. The applications of such devices range broadly from polyfunctional analysis, chemical/material synthesis or synthetic biology. Polyfunctional analysis applications such as omics (genomics, proteomics, cellomics, transcriptomics), characterizing chemical and biological reaction kinetics, cell/organoid/immuno-assays for developing therapies, for example DropSeq. By material synthesis applications I refer to microfluidic devices to produce complex multi-level emulsions (eg: O/W/O/W), lipid and polymeric nanoparticles, self assembled nano-structures and tunable inks for 3D bio-printing. Synthetic biology applications lie between generalized analytical and synthetic applications of microfluidics. These typically involve identifying and isolating optimal enzymes and proteins for catalysis, cell

lines, or directed evolution of microbes for large scale synthesis, for example Berkeley Lights.

Applications which require prolonged windows of exposure to certain conditions (light, flow, thermal or chemical gradients) or prolonged observation/incubation are ideal opportunities for a direct application of oscillatory flows in centralized microfluidics. In such cases, oscillatory flows can be used to minimize footprint and the pressure drop of the circuit albeit at the cost of additional complexity. Examples of this principle being used are [Jo et al., 2009, Alizadehgiashi et al., 2009, Abolhasani and Jensen, 2016]. Other important opportunities include mimicking physiological environments, and preventing or minimizing clogging and or fouling of the channel walls [Dincau et al., 2019].

Despite the variety of applications that fall under the umbrella of centralized microfluidics, the common thread that runs through all is the ever increasing demand for higher throughput, especially for synthesis and synthetic biology applications. Furthermore, it is often not possible to increase the throughput by simple parallelization, such as when expensive optical equipment is required for operation. A generalized nonlinear microfluidics based approach can be transformative for increasing the throughput of these systems. This is because, in most techniques for particle and droplet manipulation, efficiency is adversarial with the speed of the transport flow. That is, the separation field, often applied orthogonal to the direction of flow, is overpowered by the transport flow at high flow rates, resulting in poor performance. Although the orthogonal forces can be made proportionally stronger in theory, this poses an increased risk of damaging delicate bio-particles. In stark contrast, nonlinear microfluidic techniques improve with throughput. This could either be purely due to inertia, as seen from inertial focusing, or possibly due to cross-coupled interactions between hydrodynamic and other field effects as demonstrated in SOEIF. It is therefore beneficial to better explore and characterize how nonlinear hydrodynamic effects interact with these various other fields and expand this repertoire of possibilities. Further research into the applications of nonlinear microfluidics for operations other than mixing and particle manipulation, such as droplet formation, fusion and fission is especially wanting.

Although there is great potential in nonlinear microfluidics for scaling up microfluidic throughput, testing and prototyping such systems presents a formidable challenge. This is because, hydrodynamic nonlinear effects are often subdominant at the low speeds typically encountered in prototype microfluidic applications, and can be overlooked if not actively being investigated. Using increased speeds causes the window for observing and quantifying these flow-accelerated effects to shrink rapidly despite the phenomenon becoming more effective. Furthermore, identifying the particular nonlinear terms and mechanisms responsible for any given effect is not a straightforward process for steady flows. A problem made more difficult when interactions between hydrodynamics and other fields is being examined, since multiple nonlinear effects of different characteristic timescales often occur together. For instance, consider that it took over 10 years with several competing analytical theories to correctly identify the hydrodynamic effect responsible for the Segre-Silberberg effect [Segré and Silberberg, 1961, Ho and Leal, 1974].

It is precisely to address the above challenge of uncovering nonlinear mechanisms, that I expect oscillatory flows to be most useful in the coming years. This is for two reasons: the first is that oscillations, particularly in the $10-1000$ Hz frequency range enable exposure to high velocities without the associated displacement, allowing the long distance consequences of the phenomenon in question to be observed and accurately characterized. A property harnessed to measure the migration velocities in Chapter 4 and Chapter 5. These measurements, when performed in high aspect ratio channels can be used for direct comparison with theory and simulations, further accelerating the process of design and implementation. The second is that selective combinations of nonlinear terms can be isolated by choosing the oscillatory frequencies appropriately. For instance, to isolate the term $\sim U^2E$, one could use, a frequency of 100 Hz for the electric field and 50 Hz for the oscillatory flow. This concept has been demonstrated through SOEIF in Chapter 5. A related advantage is that the timescale relevant to the process can be systematically isolated and probed via frequency. Such clear characterization, will enable better design of high throughput steady flow systems. For ex-

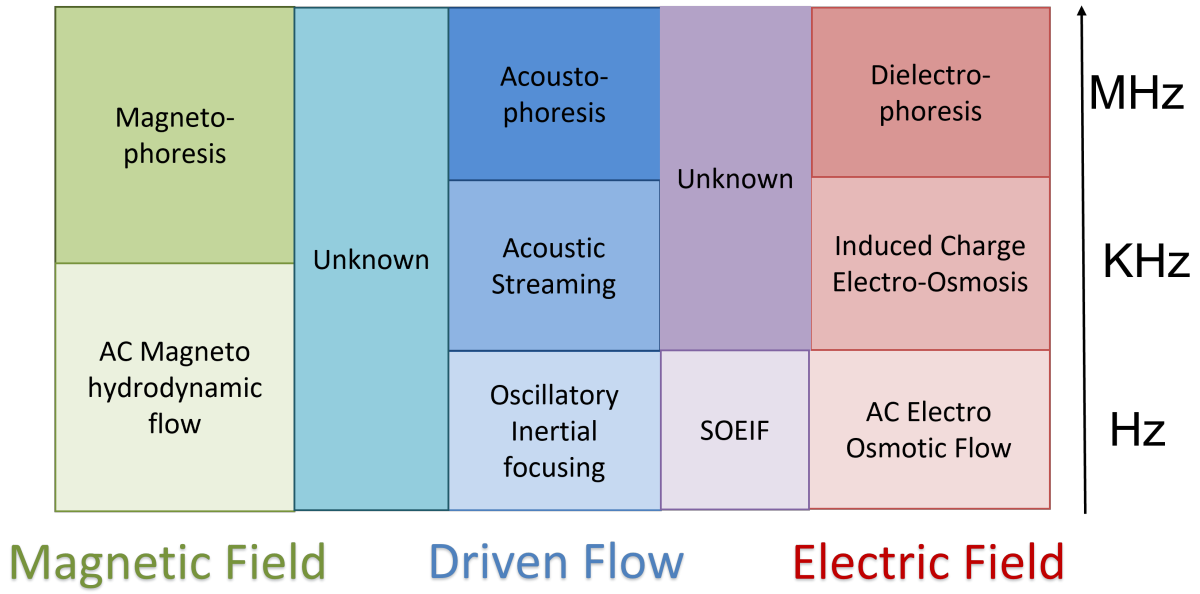

Figure 6.2: Illustration of future avenues for exploring nonlinear oscillatory microfluidics. SOEIF arises from nonlinear interaction between oscillatory flow and field at low frequencies (Hz). Similar nonlinear interactions between Induced Charge electro-osmosis and steady streaming (KHz), acoustophoresis and dielectrophoresis (MHz), and those between AC magnetohydrodynamic and oscillatory flow (Hz to MHz) remain completely unexplored.

ample, if it is known that the U^2E coupling is most effective at a frequency of 10 KHz, one can design a flow manifold through which liquid flows at 10 cm/s with periodic features placed at every 10 μm to selectively activate and amplify the U^2E nonlinear-effect.

6.2.3 Future work

Guided by the above principles, the avenues of future exploration are summarized in the graphic shown in Figure 6.2. The immediate next step to the research presented above is to examine the non-linear cross coupling between steady streaming and induced charge electro-osmosis (ICEO). ICEO refers to the quadrupolar rectified flows that emerge around an electrically conducting obstacle when it is placed in a uniform AC electric field while being surrounded by a quiescent fluid. Steady streaming and ICEO are highly analogous flow phenomenon in both form and origin, both of which are observed in the $100 - 10000$

Hz. Such an experiment can be performed without much change to the experimental setup used for SOEIF / streaming and would only entail replacing the PDMS single cylinder with a metallic cylinder and applying a synchronized electric field and flow. The stable vortex cores in this case, could serve as a nucleation point for assembly of polystyrene particles into compact shapes of controlled sizes. Similar explorations of the interaction between nonlinear electrokinetic and acoustic phenomena such as dielectrophoresis and acoustophoresis can be performed at higher frequencies although this will require a completely different experimental setup. I hope experimentalists applying acoustophoresis will attempt this problem.

Another analogous unchartered avenue of study is the dynamics of particles in a combined magnetohydrodynamic (MHD) and pressure driven flow. MHD refers to flows driven by the interaction of a fluid with a magnetic field, usually oriented normal to the direction of flow [Al-Habahbeh et al., 2016, Lemoff and Lee, 2000]. Often this is accomplished by using a highly conductive sample (high ionic strength) and applying a current through it via electrodes that are oriented perpendicular to both the magnetic field and the channel stream. MHD has been proven to be highly energy efficient method for pumping conductive liquids without any moving parts. Likewise, magnetic manipulation of magnetic particles in a non-magnetic solution and non-magnetic particles in a magnetic solution are well established commercially used methods [Pamme, 2006].

Nevertheless, the combined non-linear effect of a driven flow and a magnetic flow on a suspension of particles in a fluid, both of which are non-magnetic has not been studied. This is an opportunity to overcome many of the limitations of SOEIF. Chief among these is that SOEIF and other electrophoretic techniques can only operate with very low conductivity samples due to the large fields used to avoid resistive heating and damage to the equipment. Another concern is the cost and size of the amplifiers / voltage sources required for producing large fields, therefore hampering scale-up and mass production of devices. Unlike electric fields however, magnetic fields and electric current are much easier and cheaper to apply at scale. I think this is a particularly worthwhile direction of inquiry because of its potential

as a high throughput, clog-free and scalable method for microplastic removal from water.

References

[Abolhasani and Jensen, 2016] Abolhasani, M. and Jensen, K. F. (2016). Oscillatory multiphase flow strategy for chemistry and biology. *Lab on a Chip*, 16:2775–2784.

[Al-Habahbeh et al., 2016] Al-Habahbeh, O., Al-Saqqa, M., Safi, M., and Abo Khater, T. (2016). Review of magnetohydrodynamic pump applications. *Alexandria Engineering Journal*, 55(2):1347–1358.

[Alizadehgiashi et al., 2009] Alizadehgiashi, M., Khabibullin, A., Li, Y., Prince, E., Abolhasani, M., and Kumacheva, E. (2009). Shear-induced alignment of anisotropic nanoparticles in a single-droplet oscillatory microfluidic platform. *Lab on a Chip*, 9:2738–2741.

[Amer Cid et al., 2021] Amer Cid, I., Ussembayev, Y. Y., Neyts, K., and Strubbe, F. (2021). Measurement of the amplitude and phase of the electrophoretic and electroosmotic mobility based on fast single-particle tracking. *ELECTROPHORESIS*, 42(16):1623–1635.

[Amit et al., 2016] Amit, R., Abadi, A., and Kosa, G. (2016). Characterization of steady streaming for a particle manipulation system. *Biomedical Microdevices*, 18:39.

[Asmolov, 1999] Asmolov, E. S. (1999). The inertial lift on a spherical particle in a plane poiseuille flow at large channel reynolds number. *Journal of Fluid Mechanics*, 381:63–87.

[Asmolov et al., 2018] Asmolov, E. S., Dubov, A. L., Nizkaya, T. V., Harting, J., and Vinogradova, O. I. (2018). Inertial focusing of finite-size particles in microchannels. *Journal of Fluid Mechanics*, 840:613–630.

[Asmolov and McLaughlin, 1999] Asmolov, E. S. and McLaughlin, J. B. (1999). The inertial lift on an oscillating sphere in a linear shear flow. *International Journal of Multiphase Flow*, 25(4):739 – 751.

[Bachman et al., 2019] Bachman, H., Fu, H., hsun Huang, P., Tian, Z., Embry-Seckler, J., Rufo, J., Xie, Z., Hartman, J. H., Zhao, S., Yang, S., Meyer, J. N., and Huang, T. J. (2019). Open source acoustofluidics. *Lab on a Chip*, 19:2404–2414.

[Basilio et al., 2019] Basilio, P. A., Torres Rojas, A. M., Corvera Poiré, E., and Olguín, L. F. (2019). Stream of droplets as an actuator for oscillatory flows in microfluidics. *Microfluidics and Nanofluidics*, 23(5):64.

[Behrends et al., 2006] Behrends, R., Fuchs, K., Kaatze, U., Hayashi, Y., and Feldman, Y. (2006). Dielectric properties of glycerol/water mixtures at temperatures between 10 and 50 °c. *Journal of Chemical Physics*, 124(14). Cited By :69.

[Bhattacharjee et al., 2016] Bhattacharjee, N., Urrios, A., Kang, S., and Folch, A. (2016). The upcoming 3d-printing revolution in microfluidics. *Lab Chip*, 16:1720–1742.

[Bhosale et al., 2020] Bhosale, Y., Parthasarathy, T., and Gazzola, M. (2020). Shape curvature effects in viscous streaming. *Journal of Fluid Mechanics*, 898.

[Cevheri and Yoda, 2014a] Cevheri, N. and Yoda, M. (2014a). Electrokinetically driven reversible banding of colloidal particles near the wall. *Lab Chip*, 14:1391–1394.

[Cevheri and Yoda, 2014b] Cevheri, N. and Yoda, M. (2014b). Lift forces on colloidal particles in combined electroosmotic and poiseuille flow. *Langmuir*, 30(46):13771–13780. PMID: 25343853.

[Cevheri and Yoda, 2014c] Cevheri, N. and Yoda, M. (2014c). Using Shear and Direct Current Electric Fields to Manipulate and Self-Assemble Dielectric Particles on Microchannel Walls. *Journal of Nanotechnology in Engineering and Medicine*, 5(3). 031009.

[Chong et al., 2013] Chong, K., Kelly, S. D., Smith, S., and Eldredge, J. (2013). Inertial particle trapping in viscous streaming. *Physics of Fluids*, 25:033602.

[Choudhary et al., 2019] Choudhary, A., Renganathan, T., and Pushpavanam, S. (2019). Inertial migration of an electrophoretic rigid sphere in a two-dimensional poiseuille flow. *Journal of Fluid Mechanics*, 874:856–890.

[Di Carlo, 2009] Di Carlo, D. (2009). Inertial microfluidics. *Lab on a Chip*, 9:3038–3046.

[Di Carlo et al., 2007] Di Carlo, D., Irimia, D., Tompkins, R. G., and Toner, M. (2007). Continuous inertial focusing, ordering, and separation of particles in microchannels. *Proceedings of the National Academy of Sciences*, 104:18892–18897.

[Dincau et al., 2019] Dincau, B., Dressaire, E., and Sauret, A. (2019). Pulsatile flow in microfluidic systems. *Small*, page 1904032.

[Fischer et al., 2002] Fischer, P. F., Leaf, G. K., and Restrepo, J. M. (2002). Forces on particles in oscillatory boundary layers. *Journal of Fluid Mechanics*, 468:327–347.

[Fischer et al., 2004] Fischer, P. F., Leaf, G. K., and Restrepo, J. M. (2004). Influence of Wall Proximity on the Lift and Drag of a Particle in an Oscillatory Flow. *Journal of Fluids Engineering*, 127(3):583–594.

[Friend and Yeo, 2011] Friend, J. and Yeo, L. Y. (2011). Microscale acoustofluidics: Microfluidics driven via acoustics and ultrasonics. *Reviews of Modern Physics*, 83:647–704.

[Glycerine Producers' Association, 1963] Glycerine Producers' Association (1963). *Physical properties of glycerine and its solutions*. Glycerine Producers' Association, New York.

[Groisman et al., 2003] Groisman, A., Enzelberger, M., and Quake, S. R. (2003). Microfluidic memory and control devices. *Science*, 300(5621):955–958.

[Ho and Leal, 1974] Ho, B. P. and Leal, L. G. (1974). Inertial migration of rigid spheres in two-dimensional unidirectional flows. *Journal of Fluid Mechanics*, 65(2):365–400.

[Holtsmark et al., 1954] Holtsmark, J., Johnsen, I., Sikkeland, T., and Skavlem, S. (1954). Boundary layer flow near a cylindrical obstacle in an oscillating, incompressible fluid. *The Journal of the Acoustical Society of America*, 26:26.

[Hossan et al., 2018] Hossan, M. R., Dutta, D., Islam, N., and Dutta, P. (2018). Review: Electric field driven pumping in microfluidic device. *ELECTROPHORESIS*, 39(5-6):702–731.

[Jain and Lutz, 2017] Jain, R. and Lutz, B. (2017). Frequency tuning allows flow direction control in microfluidic networks with passive features. *Lab Chip*, 17:1552–1558.

[Jo et al., 2009] Jo, K., Chen, Y.-L., de Pablo, J. J., and Schwartz, D. C. (2009). Elongation and migration of single dna molecules in microchannels using oscillatory shear flows. *Lab on a Chip*, 9:2348–2355.

[Khair and Balu, 2019] Khair, A. S. and Balu, B. (2019). The lift force on a charged sphere that translates and rotates in an electrolyte. *ELECTROPHORESIS*, 40(18-19):2407–2414.

[Khair and Kabarowski, 2020] Khair, A. S. and Kabarowski, J. K. (2020). Migration of an electrophoretic particle in a weakly inertial or viscoelastic shear flow. *Phys. Rev. Fluids*, 5:033702.

[Kim et al., 2013] Kim, S. J., Yokokawa, R., and Takayama, S. (2013). Microfluidic oscillators with widely tunable periods. *Lab on a Chip*, 13:1644–1648.

[Kim and Yoo, 2009] Kim, Y. W. and Yoo, J. Y. (2009). Axisymmetric flow focusing of particles in a single microchannel. *Lab Chip*, 9:1043–1045.

[Kim and Yoo, 2015] Kim, Y. W. and Yoo, J. Y. (2015). Bidirectional inward migration of particles lagging behind a poiseuille flow in a rectangular microchannel for 3d particle focusing. *Journal of Micromechanics and Microengineering*, 25(2):027002.

[Kung et al., 2019] Kung, C.-T., Hou, C.-Y., Wang, Y.-N., and Fu, L.-M. (2019). Microfluidic paper-based analytical devices for environmental analysis of soil, air, ecology and river water. *Sensors and Actuators B: Chemical*, 301:126855.

[Landau and Lifshits, 1959] Landau, L. D. and Lifshits, E. M. (1959). *Fluid Mechanics, Translated by J.B. Sykes and W.H. Reid.*, volume 6 of *Course of theoretical physics*. Pergamon Press: London.

[Lemoff and Lee, 2000] Lemoff, A. V. and Lee, A. P. (2000). An ac magnetohydrodynamic micropump. *Sensors and Actuators B: Chemical*, 63(3):178–185.

[Leslie et al., 2009] Leslie, D. C., Easley, C. J., Seker, E., Karlinsey, J. M., Utz, M., Begley, M. R., and Landers, J. P. (2009). Frequency-specific flow control in microfluidic circuits with passive elastomeric features. *Nature Physics*, 5:231–235.

[Li and Xuan, 2018] Li, D. and Xuan, X. (2018). Electrophoretic slip-tuned particle migration in microchannel viscoelastic fluid flows. *Phys. Rev. Fluids*, 3:074202.

[Liao et al., 2017] Liao, B., Wei, L., Chen, Z., and Guo, X. (2017). Na2s-influenced electrochemical migration of tin in a thin electrolyte layer containing chloride ions. *RSC Adv.*, 7:15060–15070.

[Lieu et al., 2012] Lieu, V. H., House, T. A., and Schwartz, D. T. (2012). Hydrodynamic tweezers: Impact of design geometry on flow and microparticle trapping. *Analytical Chemistry*, 84.

[Lochab and Prakash, 2021] Lochab, V. and Prakash, S. (2021). Combined electrokinetic and shear flows control colloidal particle distribution across microchannel cross-sections. *Soft Matter*, 17:611–620.

[Lutz et al., 2006a] Lutz, B. R., Chen, J., and D. T. Schwartz, D. (2006a). Hydrodynamic tweezers: 1. noncontact trapping of single cells using steady streaming microeddies. *Analytical Chemistry*, 78:5429–5435.

[Lutz et al., 2006b] Lutz, B. R., Chen, J., and Schwartz, D. T. (2006b). Characterizing homogeneous chemistry using well-mixed microeddies. *Analytical Chemistry*, 78:1606–1612.

[Martel and Toner, 2014] Martel, J. M. and Toner, M. (2014). Inertial focusing in microfluidics. *Annual Review of Biomedical Engineering*, 16:371–396.

[Michaelides, 1997] Michaelides, E. E. (1997). Review—The Transient Equation of Motion for Particles, Bubbles, and Droplets. *Journal of Fluids Engineering*, 119(2):233–247.

[Michalczyk et al., 2004] Michalczyk, A., Varigos, G., Smith, L., and Ackland, M. L. (2004). Fresh and cultured buccal cells as a source of mrna and protein for molecular analysis. *Biotechniques*, 37(2):262–269.

[Miyazaki et al., 2020] Miyazaki, C. M., Carthy, E., and Kinahan, D. J. (2020). Biosensing on the centrifugal microfluidic lab-on-a-disc platform. *Processes*, 8(11).

[Miyazaki et al., 1995] Miyazaki, K., Bedeaux, D., and Avalos, J. B. (1995). Drag on a sphere in slow shear flow. *Journal of Fluid Mechanics*, 296:373–390.

[Morita et al., 2017] Morita, Y., Itano, T., and Sugihara-Seki, M. (2017). Equilibrium radial positions of neutrally buoyant spherical particles over the circular cross-section in poiseuille flow. *Journal of Fluid Mechanics*, 813:750–767.

[Morris and Forster, 2000] Morris, C. J. and Forster, F. K. (2000). The correct treatment of harmonic pressure-flow behavior in microchannels. *Micro-Electro-Mechanical Systems*, pages 473–479.

[Mosadegh et al., 2010] Mosadegh, B., Kuo, C. H., Tung, Y. C., Torisawa, Y. S., Bersano-Begey, T., Tavana, H., and Takayama, S. (2010). Integrated elastomeric components for autonomous regulation of sequential and oscillatory flow switching in microfluidic devices. *Nature Physics*, 6:433–437.

[Mutlu et al., 2018] Mutlu, B. R., Edd, J. F., and Toner, M. (2018). Oscillatory inertial focusing in infinite microchannels. *Proceedings of the National Academy of Sciences*, 115:7682–7687.

[Nishat et al., 2021] Nishat, S., Jafry, A. T., Martinez, A. W., and Awan, F. R. (2021). Paper-based microfluidics: Simplified fabrication and assay methods. *Sensors and Actuators B: Chemical*, 336:129681.

[O'Brien, 1975] O'Brien, V. (1975). Pulsatile fully developed flow in rectangular channels. *Journal of the Franklin Institute*, 300:225 – 230.

[Ouellette et al., 2006] Ouellette, N. T., Xu, H., and Bodenschatz, E. (2006). A quantitative study of three-dimensional Lagrangian particle tracking algorithms. *Experiments in Fluids*, 40:301–313.

[Padash et al., 2020] Padash, M., Enz, C., and Carrara, S. (2020). Microfluidics by additive manufacturing for wearable biosensors: A review. *Sensors*, 20(15).

[Pamme, 2006] Pamme, N. (2006). Magnetism and microfluidics. *Lab Chip*, 6:24–38.

[Parthasarathy et al., 2019] Parthasarathy, T., Chan, F. K., and Gazzola, M. (2019). Streaming-enhanced flow-mediated transport. *Journal of Fluid Mechanics*, 878:647–662.

[Phillips et al., 2016] Phillips, R. H., Jain, R., Browning, Y., Shah, R., Kauffman, P., Dinh, D., and Lutz, B. R. (2016). Flow control using audio tones in resonant microfluidic networks: towards cell-phone controlled lab-on-a-chip devices. *Lab on a Chip*, 16:3260–3267.

[Plamen et al., 2005] Plamen, D., Andrew, F., and Jeffery, L. (2005). Chemical and biological weapons: Current concepts for future defenses. *Johns Hopkins APL Technical Digest*, 26(4):321–333.

[Rallabandi et al., 2017] Rallabandi, B., Wang, C., and Hilgenfeldt, S. (2017). Analysis of optimal mixing in open-flow mixers with time-modulated vortex arrays. *Physical Review Fluids*, 2:064501.

[Riley, 2001] Riley, N. (2001). Steady streaming. *Annual Review of Fluid Mechanics*, 33:43–65.

[Rossi et al., 2022] Rossi, M., Marin, A., Cevheri, N., Kahler, C. J., and Yoda, M. (2022). Particle distribution and velocity in electrokinetically induced banding. *Microfluidics and Nanofluidics*, 23.

[Schonberg and Hinch, 1989] Schonberg, J. A. and Hinch, E. J. (1989). Inertial migration of a sphere in poiseuille flow. *Journal of Fluid Mechanics*, 203:517–524.

[Segré and Silberberg, 1961] Segré, G. and Silberberg, A. (1961). Radial particle displacements in poiseuille flow of suspensions. *Nature*, 189:1476–4687.

[Shi and Rzehak, 2020] Shi, P. and Rzehak, R. (2020). Lift forces on solid spherical particles in wall-bounded flows. *Chemical Engineering Science*, 211:115264.

[Shilov et al., 2000] Shilov, V., Delgado, A., González-Caballero, F., Horno, J., López-García, J., and Grosse, C. (2000). Polarization of the electrical double layer. time evolution after application of an electric field. *Journal of Colloid and Interface Science*, 232(1):141–148.

[Shmilovitz, 2005] Shmilovitz, D. (2005). On the definition of total harmonic distortion and its effect on measurement interpretation. *IEEE Transactions on Power Delivery*, 20(1):526–528.

[Stoecklein and Di Carlo, 2019] Stoecklein, D. and Di Carlo, D. (2019). Nonlinear microfluidics. *Analytical Chemistry*, 91:296–314.

[Strober, 2015] Strober, W. (2015). Trypan blue exclusion test of cell viability. *Current protocols in immunology*, 111(1):A3–B.

[Thameem et al., 2017] Thameem, R., Rallabandi, B., and Hilgenfeldt, S. (2017). Fast inertial particle manipulation in oscillating flows. *Physical Review Fluids*, 2:052001.

[Vázquez-Vergara et al., 2017] Vázquez-Vergara, P., Rojas, A. M. T., Guevara-Pantoja, P. E., Poiré, E. C., and Caballero-Robledo, G. A. (2017). Microfluidic flow spectrometer. *Journal of Micromechanics and Microengineering*, 27(7):077001.

[Vishwanathan and Juarez, 2020] Vishwanathan, G. and Juarez, G. (2020). Generation and application of sub-kilohertz oscillatory flows in microchannels. *Microfluidics Nanofluidics*, 24:1–10.

[Wakaba and Balachandar, 2005] Wakaba, L. and Balachandar, S. (2005). History force on a sphere in a weak linear shear flow. *International Journal of Multiphase Flow*, 31(9):996 – 1014.

[Wang et al., 2011] Wang, C., Jalikop, S. V., and Hilgenfeldt, S. (2011). Size-sensitive sorting of microparticles through control of flow geometry. *Applied Physics Letters*, 99:034101.

[Wiklund et al., 2012] Wiklund, M., Green, R., and Ohlin, M. (2012). Acoustofluidics 14: Applications of acoustic streaming in microfluidic devices. *Lab on a Chip*, 12:2438–2451.

[Xia et al., 2012] Xia, H. M., Wang, Z. P., Fan, W., Wijaya, A., Wang, W., and Wang, Z. F. (2012). Converting steady laminar flow to oscillatory flow through a hydroelasticity approach at microscales. *Lab on a Chip*, 12:60–64.

[Xie et al., 2015] Xie, Y., Chindam, C., Nama, N., Yang, S., Lu, M., Zhao, Y., Mai, J. D., Costanzo, F., and Huang, T. J. (2015). Exploring bubble oscillation and mass transfer enhancement in acoustic-assisted liquid-liquid extraction with a microfluidic device. *Scientific Reports*, 5.

[Yang et al., 2007] Yang, J., Chen, C., Hu, I. ., and Lyu, P. (2007). Design of a self-flapping microfluidic oscillator and diagnosis with fluorescence methods. *Journal of Microelectromechanical Systems*, 16(4):826–835.

[Yang et al., 2022] Yang, S.-M., Lv, S., Zhang, W., and Cui, Y. (2022). Microfluidic point-of-care (poc) devices in early diagnosis: A review of opportunities and challenges. *Sensors*, 22(4).

[Yee and Yoda, 2018] Yee, A. and Yoda, M. (2018). Experimental observations of bands of suspended colloidal particles subject to shear flow and steady electric field. *Microfluidics and Nanofluidics*, 22:1613–4990.

[Yee and Yoda, 2021] Yee, A. J. and Yoda, M. (2021). Observations of the near-wall accumulation of suspended particles due to shear and electroosmotic flow in opposite directions. *ELECTROPHORESIS*, 42(21-22):2215–2222.

[Yew et al., 2019] Yew, M., Ren, Y., Koh, K. S., Sun, C., and Snape, C. (2019). A review of state-of-the-art microfluidic technologies for environmental applications: Detection and remediation. *Global Challenges*, 3(1):1800060.

[Zhou and Schroeder, 2016] Zhou, Y. and Schroeder, C. M. (2016). Single polymer dynamics under large amplitude oscillatory extension. *Physical Review Fluids*, 1:053301.